Examining Hydrogeological Processes in Freezing Soils using Remote Geophysical and Numerical Techniques

by

Brittney Glass

A thesis

presented to the University of Waterloo

in fulfillment of the

thesis requirement for the degree of

Master of Sciences

in

Earth Sciences (Water)

Waterloo, Ontario, Canada, 2019

Author's Declaration

I hereby claim that I am the sole author of this thesis. This is a true copy of the thesis, including any required final revisions, as accepted by my examiners.

I understand that my thesis may be made electronically available to the public.

Acknowledgements

As I reflect on the journey that has been the completion of this thesis, there are many people I would like to acknowledge and thank for their guidance and support. Firstly, I thank my supervisor, Dr. David Rudolph, for providing the inspiration which started this project, and for his dedication to my role in it. Dave's passion and continued interest in this work gave me the motivation I needed to persist through the challenges and hurdles that go along with a thesis, and for this, I am very grateful to him.

Secondly, I would like to thank my committee members, Dr. Andre Unger and Dr. Claude Duguay, for their feedback and assistance throughout this process. I feel very fortunate to have had committee members who are so knowledgeable and insightful in this particular area of study. I am also indebted to Dr. Brewster Conant Jr., whose dedication to the field campaign allowed me to verify many of the hypotheses and predications I made surrounding the occurrence of icings.

Thirdly, I would like to acknowledge my family and friends for their support and encouragement throughout this time. To Iwona and Sarah, I thank both of you for always being available for hugs and for coffee chats. When I began this venture, I did not expect to find friends who are as dear to me as you both are now. To Andrew, I thank you for your input and assistance working through many of the questions that arose in this work. You too have been a great friend and support to me, and I look forward to continuing to work with you on this project. To Mike, thank you for always supporting my dreams; thank you also for bringing me lots of Bubble Teas during the nights I spent writing.

Finally, I gratefully acknowledge the University of Waterloo, the Royal Bank of Canada Water Scholarship program, Global Water Futures, NSERC, and the Farvolden Groundwater Research Scholarship fund for the financial support they have provided for this work.

Abstract

The work presented in this thesis aimed to demonstrate the use of remote geophysical methods and numerical modelling to address questions related to hydrogeological processes in freezing soils. Two different study areas and research questions were investigated: In chapter 1, Landsat 4-5 TM and RapidEye-3 datasets were used to identify groundwater discharge zones in the Central Mackenzie Valley of the Northwest Territories. Given that this area is undergoing active shale oil exploration, identification of groundwater discharge zones is of great importance. Discharge zones represent groundwater-surface water interaction points that are potential pathways for contaminants associated with hydraulic fracturing to move. Following the works of Morse and Wolfe (2015), a series of image algorithms were applied to imagery for the entire Central Mackenzie Valley, and for the Bogg Creek Watershed (a sub watershed of the CMV) for selected years between 2004 and 2017. The algorithm series extracted 'icings' from the images. Icings (also called aufeis) are surface ice lenses where groundwater discharges in the winter months, then freezes. Icings were statistically examined for all of the selected years to determine whether a significant difference in their occurrence and size existed. It was concluded that there was a significant difference in the spatial distribution of icings from year to year, but that there were several places where icings were recurring. During a field visit in August of 2018, high resolution thermal imagery was captured for several of these locations and it was found that groundwater was also discharging in the summer. This provides strong evidence to suggest that the recurring icings represent springs from which groundwater discharges year-round. These springs represent ideal locations to monitor the quality of discharging groundwater following the establishment of fracking operations. Furthermore, identifying these monitoring points remotely is expected to have drastically reduced the field efforts that would have been required to find them in situ. This thesis demonstrates the value of remote geophysical methods for hydrogeological applications, particularly in areas that have limited accessibility.

The second component of this thesis establishes a conceptual model that describes the processes which influence winter subsurface pipe and water main breakage in Southern Ontario. Recent winters in this region have seen a dramatic increase in the number of pipe/main breaks that occur above the regional water table, but below the freezing front. Though subsurface pipe breakage is well-understood in saturated conditions or in the case when it is encompassed within

the freezing zone, it is not well understood in the conditions of unsaturated soil which is not frozen, but contains a frozen zone above it. It is hypothesized that differential stress may be exerted on a pipe as soils of different frost heaving potential freeze and expand above the pipe. Once a certain overburden pressure is exceeded and upward frost heaving is no longer possible, it is expected that subsequent freezing will exert force onto the soil skeleton (and therefore pipe) below it. Two specific conceptual problems are developed in this work, and the processes which affect the distribution of stress in each case are described in detail. Then, a plan for the numerical implementation of each problem using the finite element model ABAQUS is given. Though the numerical models are not shown in this work, the conceptual models provide the framework which is necessary to implement a successful numerical model. The problem of pipe breakage in the unsaturated zone is complex and requires the coupling of equations which describe groundwater flow, stress-strain in a porous medium, and heat transport. Therefore, it was vital for an in-depth conceptual understanding of the problem to be established before introducing the numerical application.

Table of Contents

List of Tables

List of Figures

Chapter 1 - Introduction: Examining hydrogeological processes in freezing soils using remote geophysical and numerical techniques

Freezing soil and permafrost processes can significantly influence the nature of the hydrogeological regime. Understanding the role that these processes play has become increasingly important in light of both climatic changes and anthropogenic development. Two specific research questions, for different study regions, were investigated in this work. The first of these research questions is conducted for a region of active shale oil exploration in the Northwest Territories – The Central Mackenzie Valley (CMV). The goal of the work in this region was to use remote geophysical imagery to pinpoint promising field monitoring locations which a) represent active groundwater-surface water (GW-SW) interaction points, and/or b) have seen continually degrading vegetation in recent years. The significance of these criteria is important with respect to both global climate change, and to the development of shale oil operations.

Currently, the CMV's hydrogeological regime is poorly understood; this is largely due to its remoteness, lack of access, and small population. In anticipation of shale oil operations, it is crucial to locate regions where groundwater interacts with surface water as these places are most vulnerable to surface contamination in the event of a spill or leak related directly to oil fracking, or to leaching of fracking fluids and wastewater (Loh, et al. 2015). In addition, information about GW-SW interaction points form the beginning of baseline environmental monitoring in the CMV that is of immediate interest to both the Government of the Northwest Territories (GNWT) and the local inhabitants of the CMV region. The current research program was developed in response to water security challenges in the Northwest Territories resultant from climatic changes and industrial expansion. Water security issues in this region of Canada are manifested as both quality and quantity concerns. For this work specifically, criterion (a) listed above contributes to the monitoring of water quality as it migrates through the subsurface to eventually reach surface water bodies. Not only does this work benefit the larger goal of environmental monitoring and predictive modelling, but it also benefits the communities of the Sahtu Settlement Region who directly access both surface and groundwater in the CMV. In advance of shale oil operations, many of these communities expressed concerns regarding groundwater contamination, volume of water use by fracking operations, and disruption of animal migratory

paths that are relied upon for hunting. An overall objective of the research work is to quantify and ultimately minimize the impact that industrial growth will have on these remote and self-sustaining communities.

Criterion (b), to locate regions of continuing vegetation degradation, relates more specifically to climate change than to industrial development. It has been observed in previous works that vegetation in Northern Canada has an extremely variable response to climate change. Some regions have seen increased greening as a result of warmer atmospheric temperatures and longer growing seasons (Girardin et al. 2016), while others have seen vegetation degrading as a result of permafrost thaw that leads to constant subsurface saturation and surface flooding (Quinton et al. 2011, Narita et al. 2015). Regions slightly south of the CMV, such as the highly studied Scotty Creek Watershed within the Laird Basin, have experienced the latter of these. It was therefore hypothesized that the CMV may be beginning to experience the same effects. Vegetation patterns have innumerable implications for overall ecosystem health and function. Areas that experience continual vegetation degradation should therefore be prioritized as field monitoring locations as they present an opportunity to quantify the effects of climate change and serve as baseline monitoring sites. Additionally, they provide important information about the region's hydrogeological processes: they indicate areas where permafrost is likely thawing, and where the position of the water table is changing.

One of the major challenges in establishing environmental monitoring in the CMV is the remoteness of the region. Field campaigns, though of course necessary, are logistically challenging and very costly to initiate. Remotely sensed imagery provides an effective and relatively inexpensive method of both monitoring the environment and establishing priority in situ monitoring locations. Much effort, time, and financial resources can be saved by pre-determining field locations prior to beginning field campaigns. With specific attention given to hydrogeological analyses, this research notes a large gap in the use of remote geophysical methods for assessment of subsurface parameters related to hydrogeological processes. This may be due to the already well-researched and effective in situ methods used in hydrogeological studies. The current research aims to demonstrate the effectiveness of completely remote methods that use surface features as proxies for subsurface processes. In situ hydrogeological

evaluations are precise in their assessments of subsurface processes, but they are not generally feasible on large scales, or in remote regions. Use of high resolution (< 5m pixel size) rather than medium or coarse resolution imagery can greatly increase the accuracy of remote environmental analysis such that it will be more comparable to in situ analysis. Approaches to combine terrestrial-based data with the remote sensing information is critical for upscaling local data and ground-truthing of the satellite-based data. For both criterion in this work, high resolution RapidEye-3 and Planet Scope imagery are utilized and compared to medium resolution Landsat imagery. The work presented here provides a methodology that will be easily adapted for other regions and that can be accomplished with very little cost on large scales.

The second research question investigated in this work is given in Appendix A. This component of the thesis aimed to conceptualize a numerical model used for the predication of subsurface stress and strain resultant from freezing and thawing of frost susceptible soils. Specifically, the conceptual model developed here examines the effect of seasonal freezing and thawing on underground pipes and mains by locating points of maximum stress within the subsurface. The methodology used to address this research question may also be adapted for use in other regions (such as the Central Mackenzie Valley) which experience seasonal freezing and thawing of the ground and where subsurface infrastructure such as petroleum pipelines are located. It has been well documented that shallow pipes and mains can be damaged when a downward propagating frost front encompasses and freezes them (Fu et al. 2014, Zhu et al. 2013). However, recent observations in Southern Ontario have documented damage to pipes and mains (during winter) that lie well below the maximum depth of the freezing front. This observation led to the hypothesis that the alteration of material properties during freezing exerts a differential stress on pipes and manes below the freezing front, even when they do not freeze. The conceptual model developed to describe this problem will later be applied to numerical scenarios that will pinpoint the material properties and conditions which are most conducive to subsurface stress, and by extension, mane and pipe damage. This information will be valuable to engineers and city planners as they design and construct new developments; the results of this work will indicate which conditions are most likely to be problematic when implementing new pipes and manes, which regions may currently be at risk, and which conditions are more likely to be favorable.

In addition to providing a conceptualized model for the specific problem described above, this work gives a comprehensive review of currently existing numerical models which are capable of simulating heat transport processes in porous media; the benefits of these models are described in detail, and recommendations are given for solving different types of freeze-thaw problems numerically. This section details three main types of numerical models which are capable of simulating heat transport: Groundwater-heat transport (GW-HT) models, Mechanical deformation-heat transport (MD-HT) models, and Groundwater-Mechanical Deformation-Heat Transport (GW-MD-HT) models. As evidenced by their names, these models simulate heat transport in addition to either mechanical deformation or groundwater flow, or both. Depending on the application, one type of these three model categories may be more appropriate than another. For the conceptualized pipe freeze-thaw model described above, it is assumed that the numerical model will be of a GW-MD-HT type, coupling all three systems of equations.

The thesis to follow is organized as such: Chapter two will address the first research goal, 'Locating priority groundwater monitoring locations and regions of degrading permafrost in the Central Mackenzie Valley'. This chapter includes sections detailing the study area, relevant background information, specific research objectives, methodology, analysis, results, and conclusions. Appendix A will address the second research goal, 'Conceptualization of a model for frost heave induced pipeline damage'. This appendix includes relevant background information pertaining to the current state of frost heave and freezing soil modelling, specific research objectives, methods for conceptualizing two specific cases, and hypotheses pertaining to those cases. These two thesis components are broadly related, but are distinct sections so that they may be rapidly translated to journal articles.

2.0 Locating priority groundwater monitoring locations and regions of degrading permafrost in the Central Mackenzie Valley

2.1 Study Area

The methodology tested here, which aims to detect groundwater surface water interactions through the use of remote geophysical data, is focused on a 6300 sq. km section of the lower Central Mackenzie Valley (CMV) of the Northwest Territories shown in Figure 1. The region represents an expansive and diverse ecosystem which remains largely undeveloped. Recent oil and gas exploration has necessitated the establishment of baseline studies which will monitor both ecosystem health and groundwater/surface water quantity and quality. Given here is an overview of the current knowledge of the CMV, summarized from technical reports of oil/gas lease companies, the Government of the Northwest Territories, and select research papers.

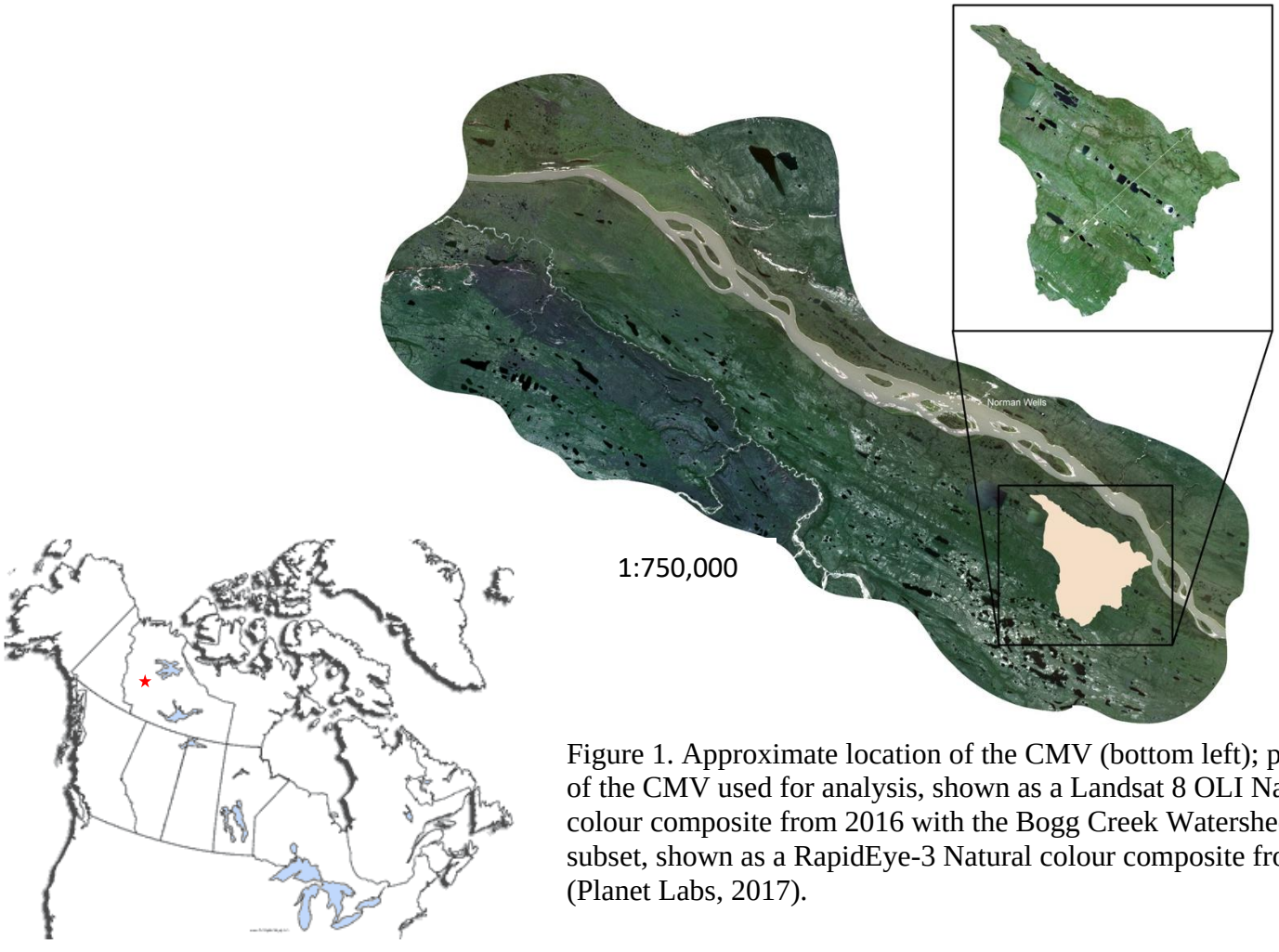

Figure 1. Approximate location of the CMV (bottom left); portion of the CMV used for analysis, shown as a Landsat 8 OLI Natural colour composite from 2016 with the Bogg Creek Watershed as a subset, shown as a RapidEye-3 Natural colour composite from 2017 (Planet Labs, 2017).

This particular section of the Central Mackenzie Valley is chosen as it encompasses all of the leases currently owned by Husky Energy Ltd (Surface Water Quality Assessment, Husky Energy, 2016). Within the CMV, the Bogg Creek Watershed is of particular interest as it contains an access road which will increase the feasibility of future field work in this remote area.

2.1.1 Geographic Situation

The CMV is bound by the Mackenzie River in the east and the Mackenzie Mts. in the western portion of the study area. The valley itself is characterized by undulating topography which slopes gently upwards from the base of the Mackenzie River to the Mackenzie Mts. The elevation change from Norman Wells, NWT to the base of the mountains is approximately 300m in the Euclidean direction. The valley is interspersed by an extensive rectangular/trellis drainage system (described in more detail below) and water bodies which tend to follow a linear pattern from North to South. This part of the CMV is largely uninhabited save for the towns of Norman Wells, located at 65.3° N, 126.8° W at 73 m of elevation, and Tulita, located at 64.9° N, 125.6° W at 101 m of elevation. These towns comprise the Sahtu Settlement Region, populated primarily by First Nations communities. The CMV is comprised of three distinct ecosystems which, although similar overall, do possess some unique topographic characteristics. These regions are the North Mackenzie Plains, Carcajou Plains, and Mackenzie Foothills regions (Ecosystem Classification Group, 2007, 2010; AMEC, 2014). The North Mackenzie Plains comprise the majority of the study area, which is the undulating valley parallel to the Mackenzie River. The Carcajou Plains represent a transition zone between the flat wetland dominated plains in the east and the higher elevated regions in the west (Amec, 2014). Finally, the Mackenzie Foothills represent the region parallel to the Mackenzie Mts. which has the greatest variability in elevation throughout the entire study area, spanning from 200m a.s.l. at the eastern (closer to river) side, to 900m a.s.l at the western (foot of the mountain) side (Amec, 2014). The National Ecological Framework of Canada characterizes the Mackenzie valley as two ecozones: The Taiga Plains (valley region) and the Taiga Cordillera (mountainous region) (CanSIS, 2017). These ecozones are broader than the ecosystem classifications described above.

2.1.2 Climate

The works of Rouse et al. (1997) characterize the CMV as a subarctic climate, owing to its below freezing mean annual air temperatures. Average annual mean air temperature, rainfall and snowfall are given by Environment Canada from 1943-2012 at climate stations in Norman Wells and Tulita: For Norman Wells and Tulita respectively, the average air temperature is -5.7°C and -5.3°C, the average rainfall is 181.0 and 183.5 mm, and the average snowfall is 151.8 and 114.9 mm. For the Mackenzie Valley, the 2005 Arctic Climate Impact Assessment (ACIA) reports annual average temperature increases between 2-3°C in the past 50 years, and up to 4°C during the winter for a period from 1958-2012 (Climate Change in the NWT, 2012). The same study reports increase in precipitation from 1958-2012 in the fall and winter and decrease in precipitation during the spring and summer. These trends are slight in all seasons but summer, where the decrease in average annual precipitation is significant (~25 mm over the course of the 50 year measured period). For Norman Wells specifically, overall mean annual temperature increases from 1943-2011 and is given by Environment Canada and compiled in Figure 2 below.

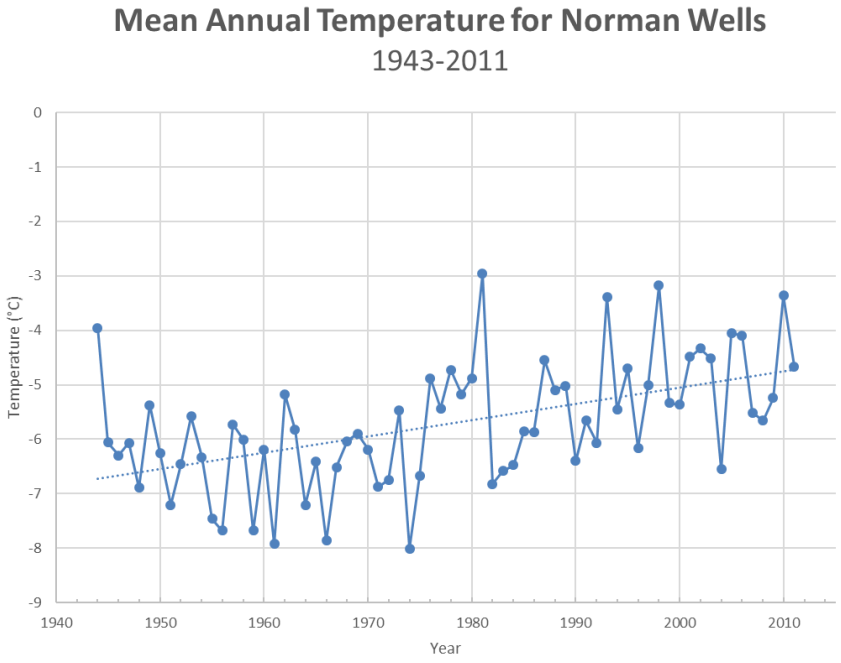

Figure 2. Mean annual temperature trend for Norman Wells, NWT, from 1943-2011 (Environment Canada, 2018).

2.1.3 Vegetation

The account of vegetation given here is summarized from the works of Hugh M. Raup (1995) unless otherwise indicated. Vegetation patterns within the Mackenzie Valley are highly influenced by the frequent occurrence of forest fires. Such fires have become more common in recent years due to lack of summer precipitation and increased dryness. The dominant tree species in this ecosystem is the white spruce (*Picea glauca),* a coniferous tree which thrives in many different types of soil but does not do well in persistently saturated conditions. Spruce tree stands are normally interspersed with pine, aspen, and in a few locations, birch trees. Tree stands which contain pine species (typically *Pinus banksiana*) are generally representative of those which have regenerated following a burning event. Undergrowth in spruce and spruce-mix stands is sparse, but where it does exist, it is populated by mosses and small lichens.

In the Taiga Plains region of the Mackenzie valley, tree stands are interspersed by wetlands and semi-open prairies. Wetlands are dominated by black spruce (*Picea mariana*) and significantly more undergrowth than white spruce stands. Unlike the white spruce, black spruce is tolerant of wet conditions. Wetlands are well established in regions where bedrock has been eroded to create a depression that does not drain well. Semi-open prairies, composed of primarily lacustrine soils, are populated by various grasses and sedge. Like the wetlands aforementioned, these prairies are well-developed and were not preceded by forest cover.

More recent observations of vegetation in the CMV have indicated that white spruce stands, which are typically elevated above surrounding wetlands by a permafrost bulb, have degraded in response to permafrost thaw. Once saturated, stands of spruce cannot thrive for longer than a few years. Baltzer et al. (2014) report that from the edge of these ‘permafrost plateaus’, changes in seasonal thaw, soil moisture, and leaf area index are felt between 3-15m toward the interior. This study also notes that leaf area index and soil moisture are negatively correlated, such that increasingly saturated conditions are resulting in the conversion of once healthy and dense forest stands to wet, boggy depressions.

2.1.4 Soils and Geology

According to the survey of this region from the Canadian Geologic Survey, the majority of the surface soils in the CMV are comprised of glacial till. The northwestern portion of the study area contains some significant regions of sandy soil. Along the Mackenzie River, soils are primarily silt. Throughout the study area, there are small (relative to the other surficial geology types) bedrock outcrops. The thickness of surface soils is highly variable, resultant from the complex and deformed bedrock geology.

Bedrock geology in the CMV consists of three sedimentary provinces within the Northern Foreland Belt. Sedimentary deposits span from the Late Cretaceous to Mid-Devonian and are primarily composed of shale. The thickness of these formations varies from 50m up to the thickest documented unit, the Little Bear Formation. This unit is composed of sandstone and coal, and contains a significant regional aquifer. The Canol Formation is identified as the target oil and gas formation within the CMV (Rudolph et al. 2016). It is a mid-late Devonian black shale, averaging 200m in thickness. This formation outcrops near Norman Wells within the Bogg Creek Watershed. Figure 3 below shows a detailed picture of the CMV's bedrock geology formations. There are two major folds within this region: Twenty-Five Mile Lake syncline, located in the western part of the study area, and Loon Creek anticline, located parallel to the syncline. Several thrust faults are also documented throughout the studied area, as evidenced by both the disjointed formations and the dominant trellis drainage pattern. Detailed reports on the bedrock geology of the CMV may be found in the reports compiled by AMEC (2014), Golder (2015), and Rudolph et al. (2016). Surficial geology for the study area of interest is explored in more detail in the analysis section of this chapter.

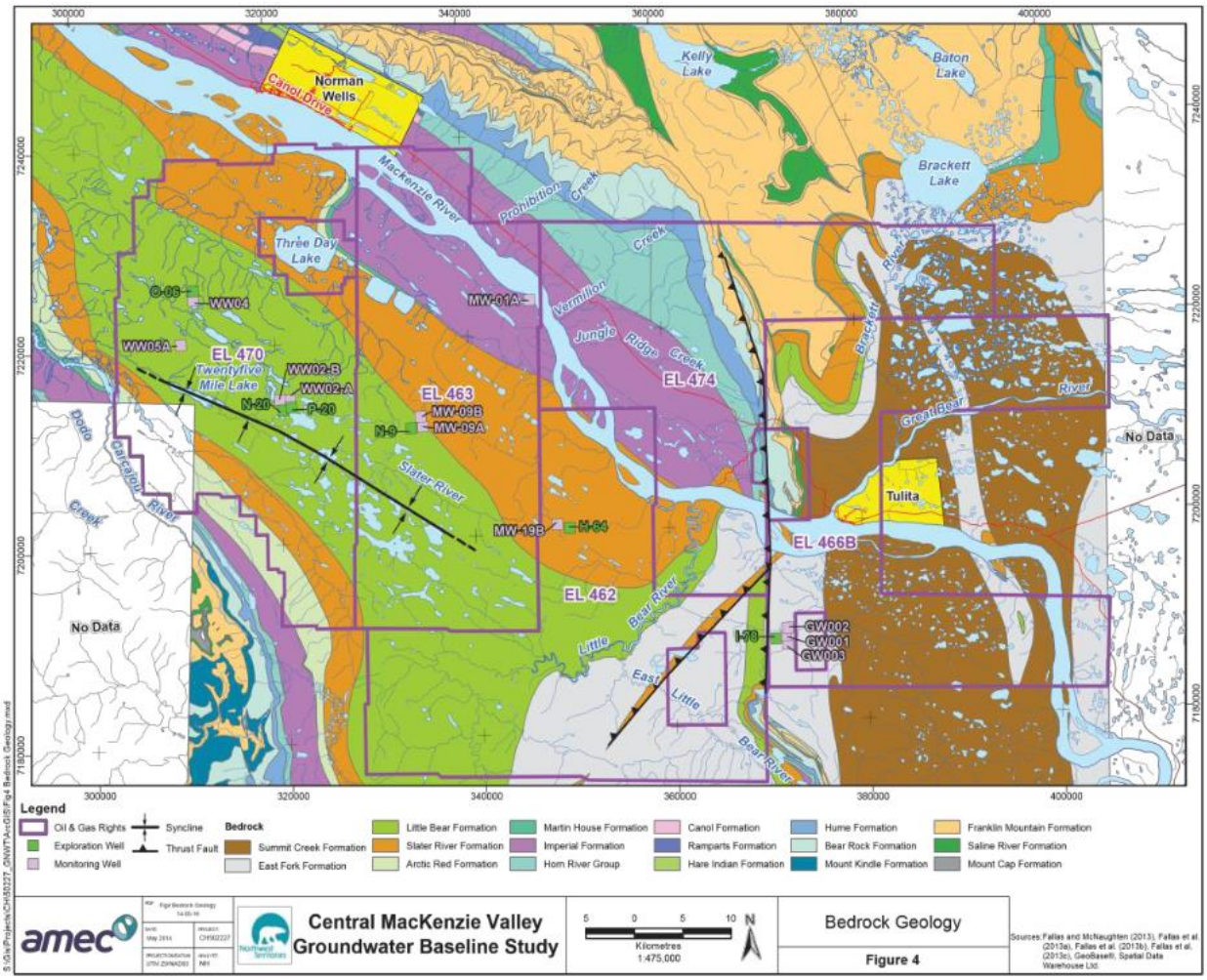

Figure 3. Bedrock Geology formations within the Central MacKenzie Valley (AMEC, 2014).

2.1.5 Hydrogeology, Permafrost, and Hydrology

The most detailed hydrogeological investigations in this study area were performed by Husky, Conoco Phillips, and MGM in the various land leases throughout the CMV as a requirement of the Sahtu Land and Water Board Land Use Permit. Prior to these investigations, which took place between 2012 and 2015, knowledge of the region's hydrogeology was very limited.

Both physical and chemical analyses were performed by the oil and gas companies. Piezometric elevations collected at the monitoring wells indicate a significant aquifer located in the Little Bear sandstone formation in which water flows from west to east at an approximate

velocity of 10cm/day (AMEC, 2014). Within the Little Bear aquifer, water-bearing sandstone layers are suspected to be separated by leaky confining layers. Regional bedrock aquifers are also found in the Martin House, Kee-Scarp Ramparts, and Hume formations (which are primarily sandstone) (Rudolph et al. 2016). No shallow aquifers were reported above the permafrost table, owing to the fact that overburden sediments are relatively thin, and where they are thicker, are composed of fine-grained material.

Permafrost in the CMV is a combination of extensively discontinuous and intermediate discontinuous (AMEC, 2014). It marks the transition zone between these two permafrost classifications. The range of permafrost thickness is extremely large, reportedly varying from 50 to 143m in the Norman Wells area alone. Some areas have no permafrost at all, giving the region the permafrost designation of 'discontinuous'. Figure 4 shows the approximate distribution of permafrost classes within Northern Canada. Thermistor data collected by Husky Oil Ltd. indicates warming ground temperatures for several monitoring stations in the region that are expected to be associated with permafrost thaw and active layer thickening. Taliks (unfrozen regions underneath water bodies), are also found throughout the study area (Rudolph et al. 2016). Groundwater recharge has not been quantified, but it is expected that regions which have lower ice-content permafrost (coarse grained materials) experience more precipitation-sourced recharge than do regions which have higher-ice content permafrost. AMEC notes that groundwater isotopic signatures are highly variable: The Summit Creek aquifer contains relatively modern groundwater, whereas the Little Bear formation contains groundwater as old as 20,000 years.

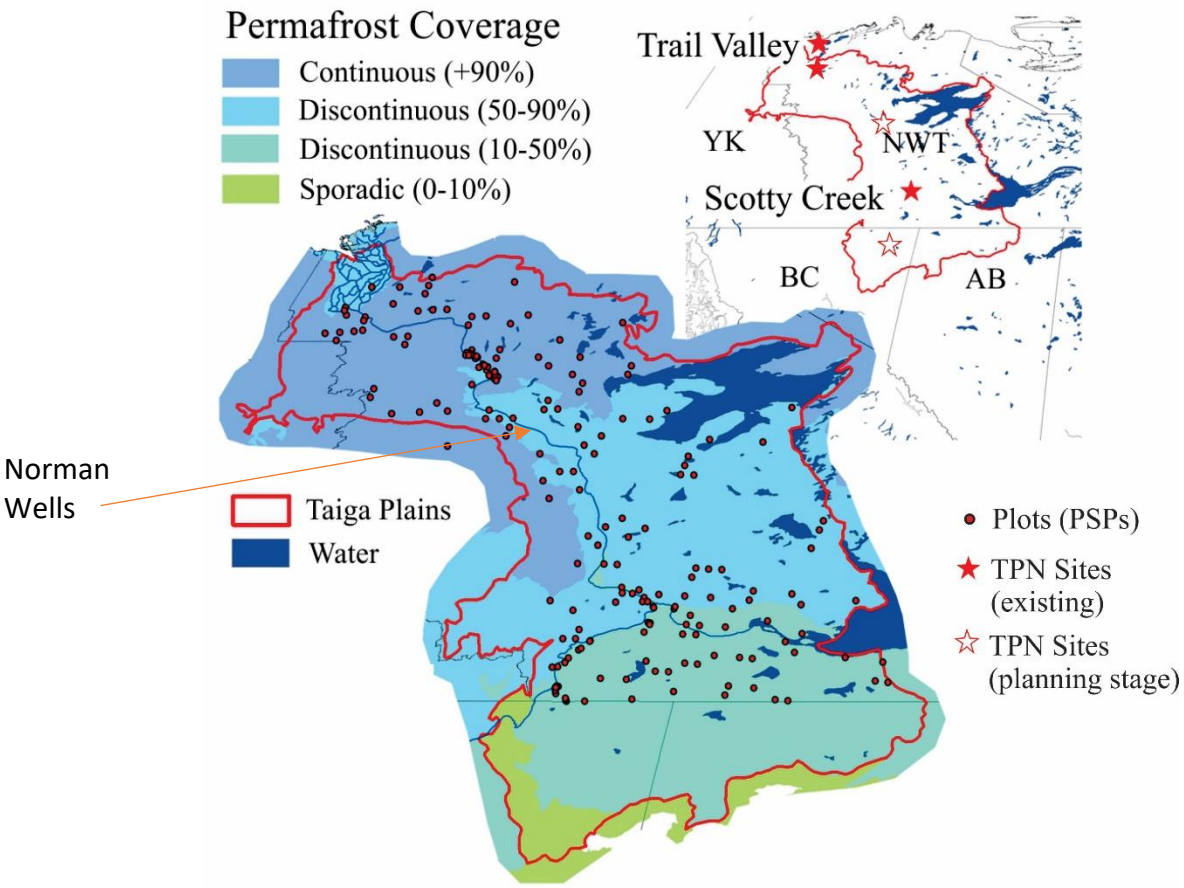

Figure 4. Permafrost distribution in Northwestern Canada showing TPN (Taiga Plains Network) monitoring sites and the approximate location of Norman Wells. (*Taiga Plains Research Network, 2017*)

The Mackenzie River is the largest in Canada, covering over 1.7 million square kilometers and flowing over 4000km from its source to the Beaufort Sea (Kokelj, 2001). A report published in 2001 by the Water Resources Division of Indian and Northern Affairs in Canada details the hydrology of the Sahtu Settlement Area (SSA) as it relates to the Mackenzie River Basin. The SSA intersects with several of the oil and gas leases, and also contains the Bogg Creek Watershed, which is of particular interest for this work.

The Mackenzie basin contains two small sub-basins, Peel River and Great Bear River (Kokelj, 2001). The Great Bear River basin covers most of the lowland area currently occupied by oil and gas leases. This lowland, which is of low relief and high storage capacity, yields consistent flow rates on an intra-annual and inter-annual basis (Kokelj, 2001). It is noted that the

permafrost rich areas discussed previously see greater surface run-off, particularly in sloped regions, due to low rates of infiltration caused by the frozen ground barrier. Hydrometric data indicates that for most monitoring stations, peak discharge occurs in the spring as snow melts and that basin response to rain events are variable (Kokelj, 2001). Overall, the basin has a far greater yield in the western tributaries (316 mm/year) than in the eastern tributaries (130 mm/year). Kokelj (2001) note that this is likely due to lower storage capacity in the west, and greater evaporation coupled with less precipitation in the east.

Within the Bogg Creek Watershed specifically, Bogg Creek drains into the Mackenzie River through a distinct trellis-shaped drainage pattern (Twidale, 2004). The largest lake in this watershed is Three Day Lake, located at the far northwest of the study area. Also within this watershed are several smaller lakes which appear to follow a very linear pattern from northwest to southeast. This is thought to be a function of the distinct bedrock joints which were already in place before the last glaciation when the lakes in this region were formed.

2.2 Background

2.2.1 Icing dynamics and use of remote geophysical sensing methods for GW-SW interactions

Groundwater-surface water interaction points can be identified by the presence of *icings* (also commonly referred to as *aufeis* in other literature). Icings are sheet-like masses of ice which can form on pre-existing river ice, or on the land surface. Three main types of icings are identified: ground type, spring type, and river type. River icings, which form when groundwater discharges through a body of river ice and laps onto a frozen river surface, are not considered in this study. Only land-fast (spring and ground type) icings are considered. These two types of icings are differentiated by the source of groundwater in which they are derived. Spring icings are formed from groundwater springs – where water tends to be sourced from sub-permafrost, deep groundwater reserves – and are often annually recurring features (Carey, 1973; Yoshikawa, 2007). Ground icings, which tend to be temporary or intermittent features, are formed when water in the active layer becomes ‘trapped’ between a downward propagating freezing front and

the top of the permafrost table (Carey, 1973). This may occur when differences in surface topography result in an uneven freezing front, or when soils of differing frost susceptibility interact. The entrapment of water in the shallow subsurface results in a temporary increase in hydrostatic head at that locality, forcing pressurized water to discharge at the surface. This concept is illustrated in Figure 5 a and b.

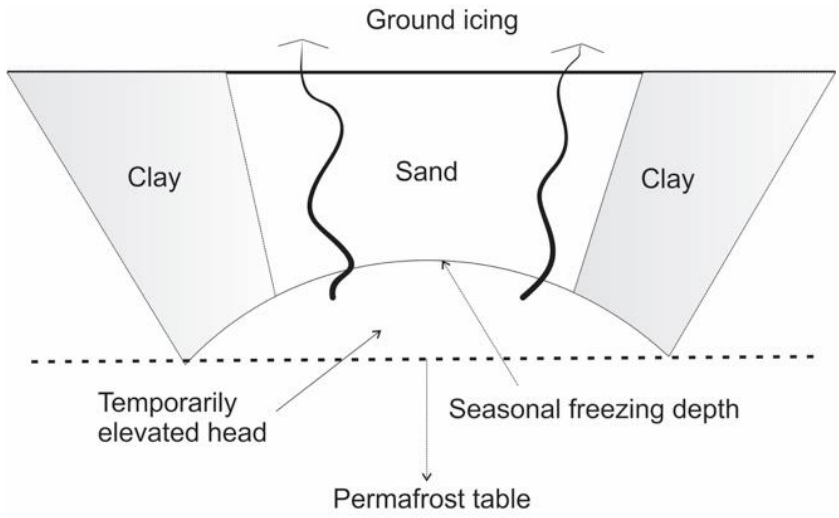

Figure 5a. Formation of a ground icing where hydraulic head has been temporarily elevated in a region below the active layer which is not frozen.

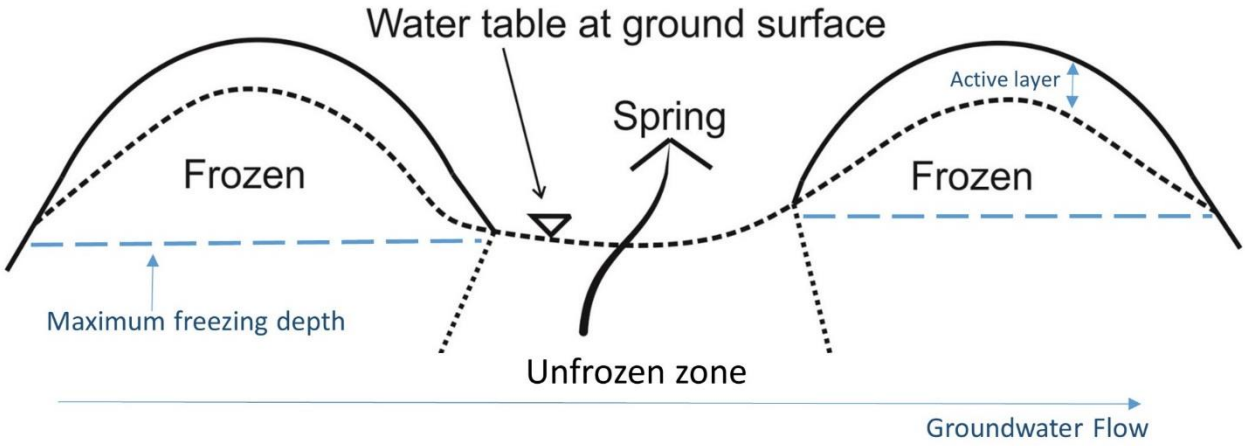

Figure 5b. Formation of a spring icing where a permanent spring exists between two adjacent permafrost plateaus.

It is noted that the mechanics and physical properties governing icing formation, particularly land fast icings, are still poorly understood when compared to the detailed understanding that characterizes many other hydrogeological processes. This is likely due to the nature of icings to occur in subarctic, permafrost bearing climates which are not heavily populated or easily accessed. However, for the purposes of identifying GW-SW interaction points, a detailed understanding of formation processes is not essential.

Remote geophysical instruments have been effective at monitoring and mapping icing distribution in regions where field instrumentation is difficult. The vast majority of remote sensing research focused on icing distribution in North America has examined river type icings in the Brooks Range of Alaska and Northern Yukon. Li et al. (1997) used single-look SAR (Synthetic Aperture Radar) from ERS-1 to monitor the seasonal growth of icings in the Inishak and Echooka river valleys. This study concluded that icings could be separated from other land cover types by observing low coherence values, noisy phase patterns, and large changes in radar backscatter. Yoshikawa et al. (2007) used a combination of NIR/SWIR and thermal infrared data derived from Landsat imagery, and SAR data derived from RADARSAT and ERS-1/2 to examine icing dynamics in another region of the Brooks Range. SAR imagery was able to discriminate icings in the late winter and spring based on surface roughness and wetness characteristics. Some discrete spring locations could be identified by Landsat thermal band data, but the authors note that the coarse spatial resolution of this dataset did result in some difficulty in accomplishing this. Thermal infrared cameras yielded better results.

The most extensive remote sensing study pertaining not specifically to river type icings was carried out by Morse and Wolfe (2014) with the goal of determining icing recurrence over a 24-year period. This work utilized an entire Landsat scene in the Great Slave Lake Region of the NWT, collected for 24 consecutive years. The methodology these researchers developed is used extensively for the work described in this thesis. Morse and Wolfe sequence a series of algorithms (described in more detail in the sections to follow) that extract icings from late spring imagery using multispectral, NIR, and SWIR1 sensors. They establish icing recurrence intervals in order to pinpoint regions which are at risk of infrastructural damage.

Other works not specifically concerned with icings have attempted to use thermal infrared datasets to delineate spring and groundwater discharge zones. Most of these studies are situated in regions that experience summers with high amounts of solar radiation as cold discharging groundwater represents itself as a stark contrast against a hot landscape (Barron and Van Niel, 2009). As such, groundwater discharge is not as easily detectable at Northern latitudes during the summer. Very few studies have attempted to delineate winter discharge zones where a snowpack is present, yet it was shown to be very effective in a study conducted by Sass et al. (2014). This work derived at-satellite brightness temperature from the Landsat thermal infrared band for a study area in the Prairie Parkland of Northern Alberta. It was found that there was good correlation between known spring locations and warm zones (presumably discharge zones) within the snowpack.

2.2.2 Use of Remote Geophysical Methods using Vegetation as a Proxy for Permafrost Thawing

Regions of Northern Canada experiencing extensive permafrost thawing have seen the conversion of forest cover into bogs and swamps as a result of flooded soils which subsequently drain and restrict plant root access to the water table (Connon, et al. 2014). This phenomenon has been observed in great detail in a watershed south of the Central Mackenzie Valley in the Lower Liard River Valley. This watershed, Scotty Creek, has seen the continual conversion of permafrost plateaus bearing coniferous forests into bogs and channel fens as permafrost plateaus thaw and subside (Connon, et al. 2014). Researchers in this region also note that depression of permafrost plateaus causes interconnectivity of once isolated bogs. This process results in an overall wetting of the region such that most types of trees cannot survive longer than 1-2 years (Quinton et al. 2011).

Other Arctic regions experience quite the opposite effect. Climate warming has, in many regions, caused an increase in greenery (Fraser et al. 2011). Whether a region experiences forest degradation or forest growth as a result of climate warming likely depends greatly on not only temperature regimes, but also subsurface variables including the rate of permafrost thaw, subsurface ice content (permafrost ice richness), drainage properties, and initial active layer

saturation conditions. These variables are interactive and quick to change, making it difficult to assess the exact cause of vegetation degradation in Northern regions in situ. Use of remote geophysical imagery has provided a cost-effective method of examining Northern vegetation patterns in areas where field work is not practical.

Vegetation within the watersheds of the Lower Liard River Valley has been examined both in the context of vegetation health and vegetation type. A study by Quinton et al. in 2003 created training sites for land cover classification including bogs, fens, and peat (permafrost) plateaus and used maximum likelihood classification to discern between them. This method proved very effective when used with IKONOS 4m optical imagery. The study notes that very wet areas (such as fens) appear to absorb significantly more infrared light than do less wet areas (such as plateaus). There is a direct correlation between the absorption of infrared light and amount of photosynthesis such that photosynthetically inactive areas will absorb more infrared light. If these areas are also wet, the effect is enhanced. This property of infrared light allows it to be a very good indicator of vegetation health.

The works of Quinton and colleagues are a rare example of vegetation studies applied to very high resolution, small scale study areas in Northern Canada. The majority of remote sensing studies conducted in Northern Canada utilize coarser imagery to study larger scale temporal trends in vegetation health and type. Such studies generally tend to be conducted with the goal of examining vegetation for purposes such as ecosystem mapping and climate change detection, rather than as a proxy for a variable not so easily assessed remotely (ex – subsurface processes). There are several examples of large scale vegetation studies which utilize coarse resolution imagery: In 2005, Fraser et al. apply a Change Screening Analysis technique using 1km resolution SPOT imagery in order to locate regions which warrant further in situ or high-resolution examination. In addition to examining SPOT imagery, the study also incorporates ancillary variables, such as proximity to active forest fires, to generate probability change maps. Several measures of vegetation change are calculated, including inter-annual differences in spatial texture, reflectance, and channel ratios. For each of these metrics, the average separability is determined over the studied time period in order to determine which metrics yield the greatest absolute change. This study was able to produce results with an overall accuracy of 94% for the

given scale. A later study by Fraser et al. (2011) examined vegetation changes using 30m Landsat-TM/ETM+ imagery with a Normalized Difference Vegetation Index (NDVI). The NDVI, taking advantage of the tendency of healthy vegetation to reflect infrared light, provides an estimate of the amount (biomass) of foliage in a vegetated region. This study analyzed four different Canadian national parks and found an increasing greening trend in all four parks. These results are strongly positively correlated with increasing atmospheric temperatures. It is important to note that these results are in contrast to those found by Quinton et al., though for different regions of Northern Canada. It is clear that the reaction of vegetation to climatic changes is complex and spatially variable. Based on an assessment of currently available literature, it appears that permafrost dynamics are not given nearly as much consideration as other climatic variables (namely temperature) with respect to changing vegetation regimes. This is likely due to the difficulty in measuring rates of permafrost thaw in an efficient way; nonetheless, its role in vegetation dynamics for regions which contain some amount of permafrost has been proven significant.

The aforementioned studies performed on large scales are considered to be of coarse resolution. Thirty meter Landsat imagery may be considered medium resolution in some cases, but it is still coarser than much of the more recently available high-resolution optical imagery (ex. IKONOS, Rapid-Eye, Planet-Scope, etc.) which is sub-5m in pixel size. Coarse resolution optical imagery introduces potentially significant error in the classification of vegetation at small scales. Though coarse resolution studies are valuable in that they efficiently assess large areas, they may not detect changes which occur on a small (i.e. a sub-watershed) scale. Where pixels are mixed (they contain more than one landcover type), classification algorithms must assume only one landcover type per pixel. The easiest way to correct errors resulting from these classification schemes is to obtain finer resolution imagery. Though this method is generally preferred, it should be noted that rigorous pixel unmixing methods do exists. Olthof and Fraser (2007) compare two methods of pixel unmixing for sites in Northern Canada: A physically based linear unmixing algorithm and a linear regression and regression tree model. This study compared both 30m and 90m Landsat datasets against 1m/4m IKONOS imagery. It was determined that for all landcover types besides shrubbery, the regression tree model was the most effective unmixing method. When compared to field data, the absolute bias against IKONOS

imagery was only 1.87%. The final unmixing scheme developed by this work was comparable to the results calibrated by local models. This study indicates that coarser resolution imagery can be used effectively when an appropriate unmixing algorithm is selected, however, it is a complex and time-consuming process. Where higher resolution imagery is available, it is likely easier to perform analyses directly on this imagery, provided that computer computation capabilities are satisfactory.

One of the major challenges with all resolutions of remote imagery aiming to draw conclusions about climate change and vegetation is to account for the effects of seasonality. It is common for research in this area to utilize only a few images over a very large temporal scale. This often leads to results which appear to be very dramatic. However, it should be considered that when few non-consecutive images are examined, there is a large amount of error introduced with respect to temporal gaps. Changes in vegetation patterns could be attributed to effects of seasonality, or other climatic variables such as forest fires or infestation, rather than to global climatic changes. The work presented here will aim to account for these confounding variables by examining vegetation for consecutive years, and by only examining vegetated regions which have continually degraded from year to year. This method is expected to eliminate much of the effect of confounding variables as it will examine a long-term trend rather than unique instances.

2.3 Research Objectives

2.3.1 Icing Extraction

The main goal in delineating icings is to locate priority field monitoring locations that will be utilized for in situ work to follow. Icings to be identified as priority monitoring locations in the CMV should be a) icings that are annually recurring, and/or b) icings that are of both spring and ground type; it is expected that contaminant transport processes and relationships to other hydrogeological processes within these two discharge types will be different. Identification of icing type through the use of remote sensing tools presents a new challenge. Due to the nature of ground icings to have only a finite supply of water (Carey, 1973), it is anticipated that in the late winter, spring icings will still be discharging warm groundwater, reaching peak formation in the early spring (Yoshikawa et al. 2007), and that ground icings will have already reached peak

formation. This distinction between the two icing types is the basis for the hypothesis presented here: that late winter thermal anomalies derived from the Landsat thermal band may be able to differentiate icing types when the effects of other land cover types (vegetation, surface water bodies) are muted. It is hypothesized that spring icings will appear in zones that are warmer against the surrounding snowpack due to the property of the snow pack to amplify the heat signature through exchange of sensible heat and heat of fusion during melting induced by groundwater (Becker, 2006). Ground icings then, should appear in colder zones due to a lack of discharging water in the late winter.

Within the main goal of identifying priority monitoring locations, four specific objectives are identified for this section of the thesis:

I. Determine the locations and extent of icings and thermal anomalies for years 2004, 2009, and 2016 using Landsat-4/5 TM and Landsat-8 OLI datasets.
II. Determine the strength of the relationship between the occurrence of icings and thermal anomalies.
III. Differentiate between ground and spring type icings based on their thermal characteristics and occurrence.
IV. Define the relationship between the occurrence of icings and surficial Geology.

2.3.2 Vegetation Monitoring

The main goal in this section of the thesis is to identify areas which have seen continual permafrost degradation for a set of consecutive years from 2012-2017. These regions will then be prioritized as field monitoring locations which warrant consideration for in situ examination of permafrost thaw rates. Permafrost degradation will be inferred from the state of vegetation, as described in the methodology to follow. Based on previous works, it is hypothesized that regions of continually degrading vegetation are associated with permafrost thaw due to the tendency of soils to first be flooded by permafrost thaw, damaging root systems, then to drain and lower the water table such that access by plant roots is restricted. Permafrost degradation has important implications for surface water dynamics, ecosystem health, and access to groundwater resources.

Within the main goal of identifying regions of continually degrading vegetation for in situ monitoring, two specific objectives are defined as follows:

I. Determine the locations in which vegetation has been continually degrading between 2012-2017 using RapidEye-3 imagery
II. Compare regions of continual degradation to thermistor data collected by Husky Energy Inc. to verify the hypothesis that permafrost thaw is associated with degrading vegetation.

2.4 Methods

2.4.1 Automatic Icing Extraction

Three Landsat images per dataset for each of the three years (2004, 2009, and 2016) are utilized in this study. A late spring image is used to discriminate icings, a late winter image to delineate thermal anomalies, and a summer image to generate a water mask used in the icing discrimination process. The images used within this study are listed in Table 1. Locating three images from the same year proved difficult due to the persistent cloud cover in the study area and the poor temporal coverage of Landsat-5 during the winter. The selected years were chosen because three images were available for those years, and cloud cover over the study area was less than 5 percent.

Table 1. Landsat scenes used for analysis.

Year	**Summer Image**	**Winter Image**	**Spring Image**	**Landsat Sensor**	**Snow Depth***
2004	Aug 17th	April 17th	May 29th	L5-TM	35cm
2009	July 30th	March 24th	May 17th	L5-TM	31cm
2016	July 1st	Feb 8th	May 14th	L8-OLI/TIRS	29cm

**Snow depth recorded by Environment Canada at the Norman Wells Climate Station for the date of the late winter image*

A simplified schematic of the pre-analysis processing of the imagery is shown in Figure 6. As aforementioned, the late spring image is used to discriminate icings optically because the snowpack has largely been depleted, yet icings still remain. Both the spring and summer images are converted from digital numbers to Top of Atmosphere Reflectance (TOA) using PCI Geomatica Software. All subsequent processing and analysis is performed in ArcGIS and/or ArcPy 10.3. Results of intermediate steps used to obtain the icing distribution are given in section 2.5.1.

The processing steps used to automatically extract icings closely follow the methodology developed by Morse and Wolfe (2014). After being converted to TOA and clipped to the extent of the study area, the Normalized Difference Snow Index (NDSI) is applied to the image:

$$(1) \qquad NDSI = \frac{Green - SWIR1}{Green + SWIR1}$$

(Hall, et al. 1995)

Using a threshold value of 0.4, ice, snow, water, and marl water are separated from the rest of the land cover types. This algorithm is founded on the principle that snow and ice will absorb most of the incoming short-wave radiation and reflect in the visible portion of the electromagnetic spectrum. Multiple studies have confirmed the effectiveness of the NDSI for this purpose (Salomonson and Appel, 2004; Yun-gang and Chuang, 2006; Hall et al. 1995). All values exceeding 0.4 are isolated from the image and used to mask the original multispectral TOA conversion. At this point in the processing, ice now needs to be separated from snow, water, and turbid water. The MDSII (Maximum Difference Snow and Ice Index) is applied to the image:

$$(2) \qquad MDSII = Green^2 - SWIR1^2$$

(Morse and Wolfe, 2014)

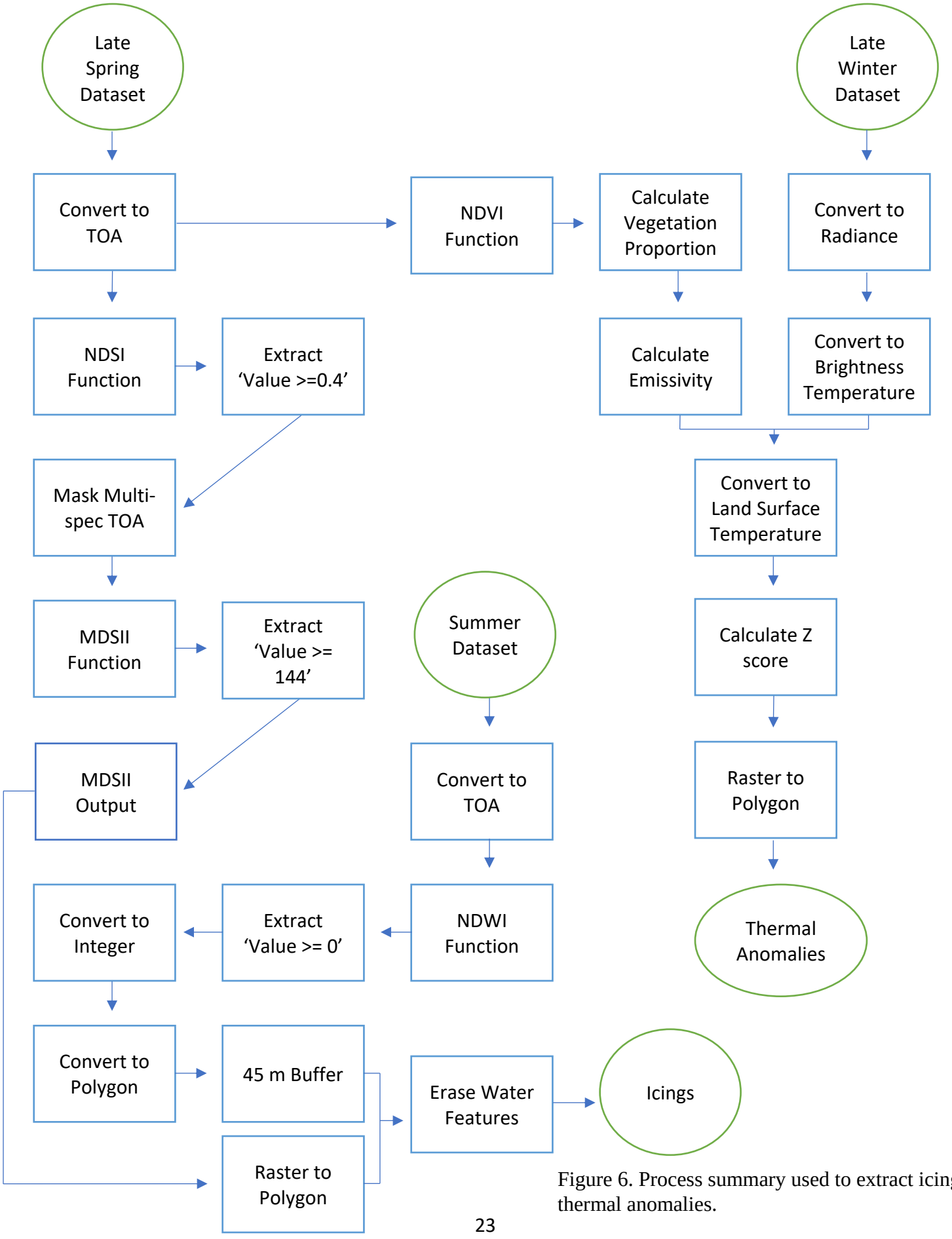

Figure 6. Process summary used to extract icings and thermal anomalies.

In a similar manner to the NDSI, threshold values of the MDSII can be used to discriminate ice from other land cover types. For a study area near Great Slave Lake, NWT, Morse and Wolfe determine a value of 0.144 to be used for discrimination of ice when some snow is still present in the scene, and a value of 0.040 to be used when no snow is present. These threshold values are found to be appropriate for this study area as well. All late-spring scenes used to extract icings are snow free, therefore the MDSII threshold value will separate ice from marl water. The distribution has not been rescaled in this study, therefore a threshold value of 144, rather than 0.144 is used for the discrimination. Values in excess of this threshold are considered to be ice and are extracted from the image.

The MDSII extracts all ice in the study area, including ice on water bodies that may not have been completely melted. In order to remove this ice from the result, a water mask is generated using an image from the summer of that year. As the extent and location of thaw ponds and thermokarst lakes may be variable in this area, separate water masks are generated for each year (rather than just one), in order to most closely approximate the position of surface water bodies at that time. Use of the MDSII to discern marl water also assists with the removal of non-permanent water features that may not be removed by the water mask. To generate the water mask, the NDWI (Normalized Difference Water Index) algorithm is applied to the summer TOA conversion:

$$NDWI = \frac{Green - NIR}{Green + NIR} \quad (3)$$

(McFeeters, 1996)

The result of this algorithm is a range of values from -1 to 1, where positive values are considered to be water. These values are extracted and converted to polygons. As some variability also exists within the stage of rivers and lakes, the polygon mask is grown outwards by 1.5 pixels (45m) to at least partially account for ice that may otherwise have been classified as an icing when it was actually surface water ice (Morse and Wolfe, 2014). The MDSII result is converted from raster format to polygon format, and the water mask is erased from the MDSII polygons to leave only land-fast icings.

2.4.2 Thermal Anomaly Delineation

The spring image is also used to compute a Normalized Difference Vegetation Index (NDVI) that is then used, in part, to identify land-surface temperature in the late winter imagery. A winter NDVI is not suitable for this purpose because the majority of vegetation is snow-covered and therefore does not represent an accurate spectral reflectance. However, vegetation may still play a role in the collection of the thermal infrared data, and thus is computed from spring imagery when icings are observed and when vegetation is no longer snow covered. The NDVI algorithm relies on the property of more dense vegetation to reflect more light in the near-infrared part of the spectrum, and is as follows:

$$(4) \qquad NDVI = \frac{NIR - Red}{NIR + Red}$$

(Rouse, et al. 1973)

Late winter imagery is used to delineate thermal anomalies which are hypothesized to have some correlation to the occurrence of icings. Because the snow pack is very thick in the late winter, it is suspected that it will serve to insulate discharging groundwater, prevent rapid freezing and growth of icings, and warm the surrounding snowpack. To the knowledge of this work, this hypothesis has not been tested in situ on spring or ground type icings and is formed on the basis that heat produced during the freezing of discharging groundwater can dissipate quickly when the snowpack is thin or not present and will be impeded when the snow pack is thick due to the property of the snowpack to act as a strong thermal insulator and absorber of sensible heat (Becker, 2006). This hypothesis is supported by the results of Diaz et al. (2015) which examined the land surface temperature product derived from the VIIRS satellite in snow covered regions. This study concludes that the relationship between absolute ground surface temperature and air temperature above the surface are much better correlated over barren ground than they are when snow covers the ground. This is due to the constancy of the ground temperature when snow is present and reflects the inability of latent heat to escape. Furthermore, this ability of the snow pack to act as an insulator is demonstrated in relation to active layer dynamics, where it serves to delay or prevent complete freezing of the active layer due to the entrapment of heat (Atchley et al. 2016; McKenzie and Voss, 2013). Thus, it is hypothesized that discharging groundwater and

spring icings will be associated with strong, warm, thermal anomalies in the late winter. Ground icings are expected to be associated with cold anomalies. As ground icings generally have a limited supply of water – unlike spring icings which have a continuous supply – they may already have exhausted their water supply at this stage of the winter (Carey, 1973). In this case, they may be represented by cold anomalies as the surrounding snowpack, without a supply of warm water, is not expected to produce a warm thermal signal.

In order to categorize thermal properties of the study area, the thermal infrared bands of Landsat satellites are converted to land-surface temperature through a series of equations which manipulate digital numbers into degrees Celsius, then Z-scores, then thermal anomalies. Band 10 from Landsat-8 OLI/TIRS, or Band 6 from Landsat-5 TM, are used as the inputs for this portion of the processing. The water mask generated for the icing analysis is also used to remove water bodies from the late winter image. This is done to ensure that lake and river ice do not appear as cold anomalies in the distribution. The coldest anomalies present should be the result of icings which are not discharging warm groundwater. To derive land surface temperature, the digital numbers of the image are first converted to Spectral Radiance:

$$(5) \qquad R_\lambda = R_{mult} * DN + R_{add}$$

Where:

$R_\lambda = Spectral\ radiance$
$R_{mult} = Sensor\ radiance\ multipler\ (gain\ coefficient)$
$R_{add} = Sensor\ radiance\ add\ (bias\ coefficient)$
$DN = unaltered\ digital\ number$

(Chander, et al. 2009)

Then to temperature in degrees Kelvin:

$$(6) \qquad T_U = \frac{K_2}{\ln \frac{K_1}{R_u} + 1}$$

Where:

$T_U = Temperature\ (°K)$
$K_2 = Thermal\ constant\ 2\ (°K)$
$K_1 = Thermal\ constant\ 1\ (mW\ cm^{-2} sr^{-1} \mu m^{-1})$
$R_u = Spectral\ Radiance$

(Wukelic, et al. 1989)

Sensor bias and gain coefficients, as well as thermal constants, are obtained from the sensor metadata. In the previous equation, '1' is an assumed emissivity applicable when the determination of absolute temperature is not required.

These equations achieve at-satellite brightness temperature, but do not account for the effects that vegetation may play in the thermal signature. Generally, lower NDVI values are associated with higher at-satellite brightness temperatures (Julien et al. 2011); in this study area this phenomenon is likely attributed to the re-emittance of long-wave radiation by barren ground. To account for interference related to vegetation density, at-satellite brightness temperatures are converted to land surface temperatures using the earlier described NDVIs. First, the NDVI is used to compute a proportion of vegetation (a scaled NDVI):

$$(7) \qquad P_v = \left[\frac{NDVI - NDVI_{min}}{NDVI_{max} - NDVI_{min}}\right]^2$$

(Carlson and Ripley, 1997)

Then the proportion of vegetation is used to calculate the emissivity of vegetation:

$$(8) \qquad e = 0.004 * P_v + 0.986$$

(Cuenca and Sobrino, 2004)

At-satellite brightness temperature and the emissivity values are then used in conjunction to determine the land-surface temperature:

$$(9) \qquad LST = \frac{B_T}{1 + \omega * \left(\frac{B_T}{p}\right) * \ln(e)}$$

Where:

$LST = Land\ surface\ temperature\ (°C)$
$B_T = At\ satellite\ brightness\ temperature\ (°C)$
$e = Emissivity\ of\ vegetation$
$\omega = Wavelength\ of\ emitted\ radiance\ (\mu m)$
$p = h * \frac{c}{s}$
$h = Planck's\ constant\ (1.438 * 10^{-34}\ m\ K)$
$c = Velocity\ of\ light\ (2.2998 *\ 10^{8}\ m\ s^{-1})$
$s = Boltzmann\ constant\ (1.38 *\ 10^{-23}\ J\ K^{-1})$

(Avdan and Jovanovska, 2016)

The result of the land-surface temperature considers the emissivity of vegetation in order to mute its contribution to the thermal signature. At this point, anomalies could be classified. However, if anomalies are to be compared over different time periods, they must be standardized to account for differences in the distributions of temperature at different times. Not all images have the same range of temperatures, nor do all temperature values overlap. As determining absolute temperatures is not the goal of this work, statistical comparison is made possible by first testing the data for normality, and then converting data into z-scores under the assumption that it comes from an initially normal distribution.

Normality within the temperature distribution is assessed by performing a Kolmogorov-Smirnov One Sample Normality test on a subset of the temperature data from each year. As each image contains approximately 7 million pixels, it was not feasible to include all data points in the KS test. Therefore, the images needed to either be down sampled, or a subset needed to be tested. The latter of these was chosen in an effort to maintain the continuity of the temperature measurements. An area of approximately 200,000 pixels was extracted from each temperature

dataset, and within this dataset, 100 pixels were randomly selected to participate in the KS test. The size of the area chosen is given in Figure 7, and its corresponding distribution is given in Figure 8. As with the previously described analysis, water is not included in the temperature distribution. The KS test compares the values of x given by some distribution to the values of x that would be given by a standard normal distribution having a mean of 0 and a standard deviation of 1. Because the KS test used here only includes one sample, a cumulative distribution function is determined for values of the 'normal' sample used as a comparison to the actual temperature distribution. The cumulative distribution function is calculated as the integral between negative infinity and x of the following function:

$$(10) \qquad F(x) = \frac{1}{\sigma\sqrt{2\pi}} e\left(\frac{-(x-\mu)^2}{2\sigma^2}\right)$$

Where μ is the mean and σ is the standard deviation.

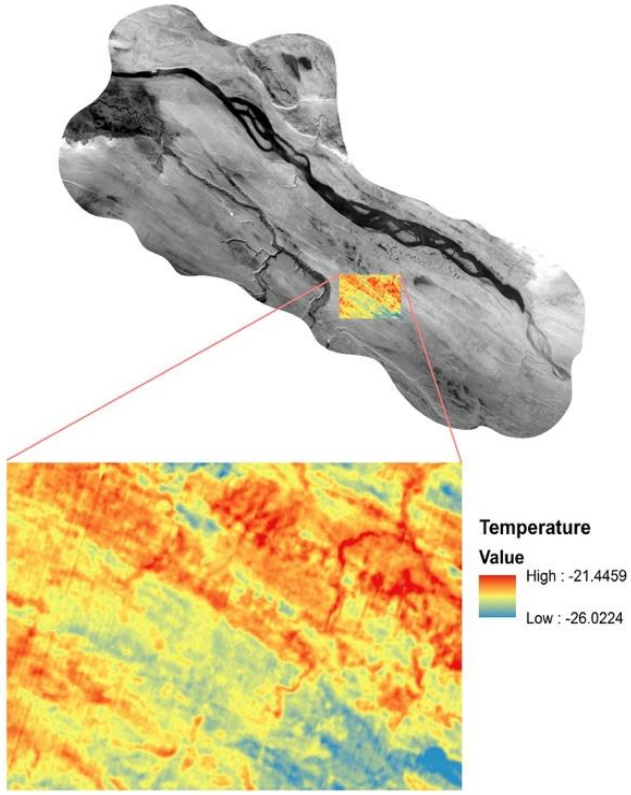

Figure 7. Size of temperature subset selected for KS test (shown for 2016).

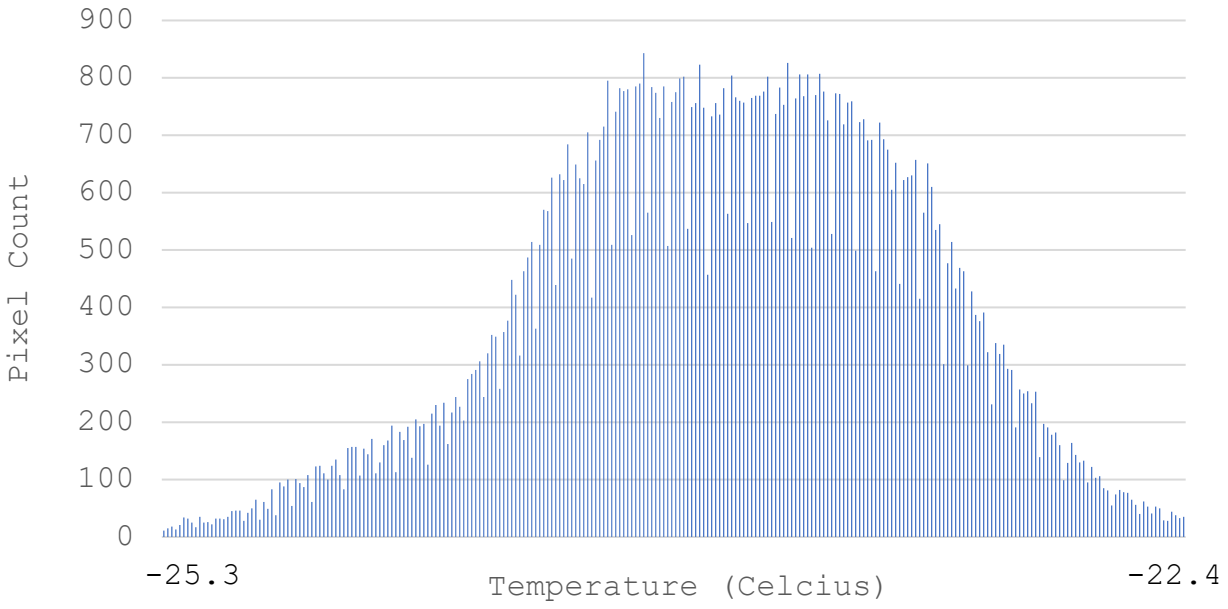

Figure 8. Distribution of temperature given by selected subset (shown for 2016).

The critical value of the KS test for samples of 100 is 0.136 at a significance level of 0.05. When the absolute difference between F(x) (the normal cum. Dist. Function) and Sn (x) (the actual cum. Dist. Function) is less than the critical value given by the KS statistic, that particular value of x is considered to be from a normal distribution. Therefore, if any one value of x has a difference that exceeds the critical value, the entire distribution cannot be normal at the given significance level. Results of the KS test, which did indicate that data were acceptably normal, are given in the results section. Once the normality assumption was satisfied, temperatures were converted into Z-scores using the following equation:

$$(11) \qquad Z = \frac{T_i - T_m}{\sigma}$$

Where:

$Z = Z - score$
$T_i = Pixel\ temperature$ (℃)
$T_m = Mean\ temperature\ of\ all\ pixels$ (℃)
$\sigma = Standard\ deviation\ of\ temperature\ distribution$

(Van Niel et al. 2004)

The Z-score conversion method was also used by Barron and Van Niel in 2009 to classify groundwater discharge zones using thermal anomalies from different time periods, and is used in many other remote sensing applications requiring comparison of a variable over multiple time periods. Z-scores of '0' represent the mean of the data. Positive Z-scores represent temperatures warmer than the mean, with the highest positive score being the strongest warm anomaly. Conversely, negative Z-scores represent temperatures colder than the mean, with the highest negative score being the strongest cold anomaly.

The Z-scores are then reclassified from floating point to integer type data in order to assign ranks of strength to the anomalies. The reclassification scheme is shown in Table 2. After reclassification, the ranked groups are converted into polygons for the analysis described in the next section. The reclassification scheme is arbitrary but is the same for all late winter images regardless of the distribution, thus making them suitable for statistical comparison.

Table 2. Reclassification scheme used to convert Z-scores to integers.

Z-Score	Integer Reclassification
3+	4
2 to 3	3
1 to 2	2
0 to 1	1
0 to -1	-1
-1 to -2	-2
-2 to -3	-3
-3+	-4

2.4.3 Field Verification

As aforementioned, one of the primary reasons for locating icings was to establish in situ groundwater monitoring locations. Upon the successful location of recurring icings, described in the analysis to follow, a field team visited the NWT study site in order to examine groundwater discharge zones in greater detail and to verify the results of the remote analysis performed for this thesis. The field techniques carried out by Andrew Wicke, Brewster Conant Jr., and David Rudolph, are briefly described here.

Several groundwater and surface water sampling procedures were performed on select icing sites which were pre-determined to be the most feasible to reach via helicopter in the time allotted for the field work. This work was performed in late August of 2018. It was not possible to visit every single site identified with the remote imagery, however, these sites may be visited in subsequent field campaigns.

Groundwater and surface water temperatures were collected with a soil temperature probe which contained a thermistor at the bottom of it. The probe is constructed of a hollow aluminum tube which can be inserted directly into surface water or into soil to read temperatures at a certain depth. For this work, the temperature was taken at 4 ft. from the surface, a depth which is well below the regional water table. Temperature of groundwater and surface water are taken in order to determine the contrast between them. This is useful for a few reasons: Firstly, it provides an idea of the contrast that should be visible with a thermal camera in areas where groundwater is discharging at the surface. Secondly, surface water locations which measure colder than surrounding surface water may be attributed to groundwater discharge.

An electro-conductivity meter installed in a YSI probe was used to measure the conductivity of both ground water and surface water. The YSI probe also measures temperature, atmospheric pressure, dissolved oxygen, total dissolved solids, salinity, and pH. EC measurements may also be used to roughly discern groundwater from surface water. Under the assumption that most surface water is precipitation derived, its EC will be quite low as it contains little to no dissolved solids. Groundwater, by contrast, is expected to have higher EC potential as it has collected dissolved solids from soil and dissolved or precipitated rock

minerals. Therefore, surface water which exhibits higher EC relative to other samples in the region may indicate groundwater discharge.

Vertical hydraulic gradients were measured in situ using a Henry probe over a vertical distance of 1 meter. The Henry probe operates like a piezometer, but can readily used in a certain section of the subsurface, then quickly removed and used elsewhere. Measurement of the vertical hydraulic gradient can be indicative of upward groundwater flow paths in regions where the upward gradient is steep compared to surrounding areas. This is of particular interest in terms of verifying icing locations as recurring icings were hypothesized to be associated with springs.

Finally, a high-resolution thermal camera was used to identify temperature anomalies in both surface water and surface land cover. The principle behind the thermal imaging is the same as that of the thermal band Landsat imagery, however, thermal cameras provide much finer resolution imagery.

2.4.4 Characterising Vegetation Using NDVI

The methodology used to extract regions of continually degrading vegetation from remotely sensed imagery, shown in Figure 9, follows a similar sequence to the process chain used to extract icings. RapidEye-3 imagery for the late summer of 2012, 2013, 2014, 2016, and 2017 are obtained from *Planet Labs.* This imagery has a spatial resolution of 5m, and includes three optical and one near infrared band. All images are first converted to Top of Atmosphere using the multiplicative coefficients provided in the image metadata. Following this conversion, each date is mosaicked and clipped to the extent of just the Bogg Creek Watershed.

The pre-processed imagery then has two separate algorithms applied to it: an NDVI (Normalized Difference Vegetation Index), and a NDWI (Normalized Difference Water Index). The NDVI is a measure of vegetation health, under the assumption that healthier vegetation is to produce more foliage, perform more photosynthesis, and therefore reflect greater amounts of infrared light. The NDWI takes advantage of the ability of water features to behave as ‘black bodies’, absorbing almost all wavelengths of visible and infrared light. The NDWI is used to

generate a water mask which is erased from the NDVI result to yield an NDVI for the study region that does not include water. Like the thermal anomaly methodology, water will confuse the results of the analysis and should be excluded when possible.

Consecutive NDVI rasters are then compared by subtracting t_1 (the later time) from t_0 (the earlier time) for each consecutive pair of years. The result provides the amount of change, per each pixel, in the NDVI index between two years. As an NDVI is scaled and has a range of negative 1 to positive 1. Changes which are negative reflect regions in which vegetation health has decreased from the previous year. In addition, its distribution tends to normal with a slight negative skew, as shown in the results section for the year 2012. As aforementioned, effects of seasonality are difficult to address. For this reason, individual pairs of years are not examined uniquely as they may represent only changes which are occurring due to seasonal variation. Rather, each consecutive pair (4 total) are intersected to extract regions which exhibit a negative NDVI change for all 4 pairs. The result is one raster which indicates locations that have seen continual vegetation degradation since 2012.

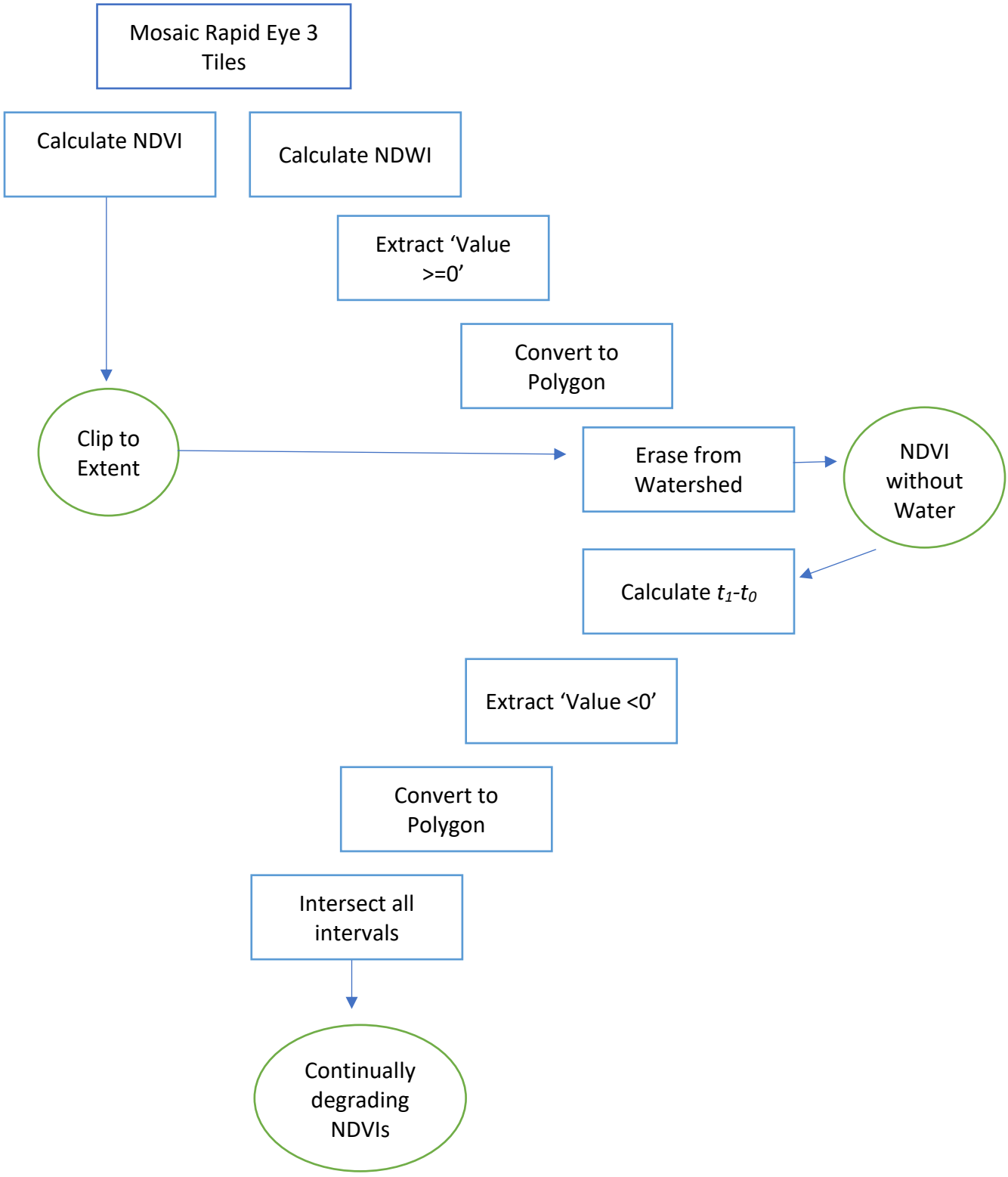

Figure 9. Process chain used to extract regions of continually degrading vegetation.

2.5 Analysis and Results

2.5.1 Results from Image Processing Steps to obtain Icings

As described in the methodology, several image processing steps are required in order to obtain the distribution of icings for a given year. Examples of each step are shown in this section for one of the years sampled.

Firstly, the Normalized Difference Snow Index separated snow, ice, and marl/turbid water from other land cover types:

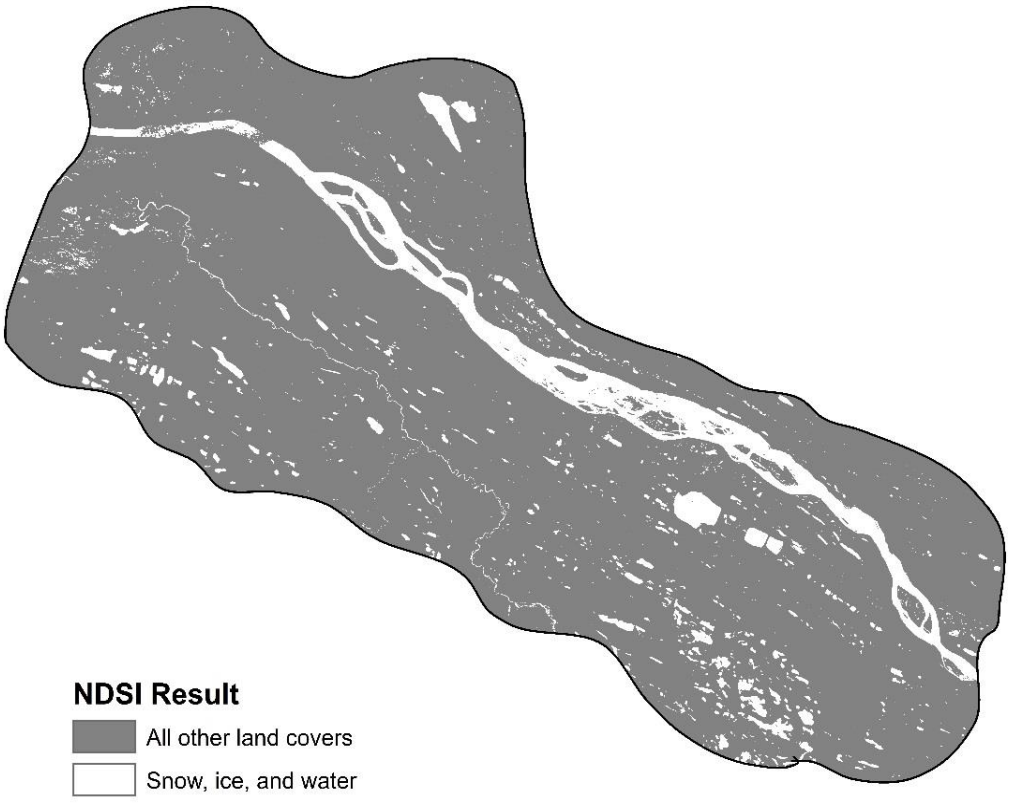

Figure 10. NDSI Result (shown for 2016).

A threshold value of 0.4 successfully separated these landcover types for all years sampled. The NDSI distribution, which is bimodal when applied correctly, is shown below in correspondence to Figure 10 above.

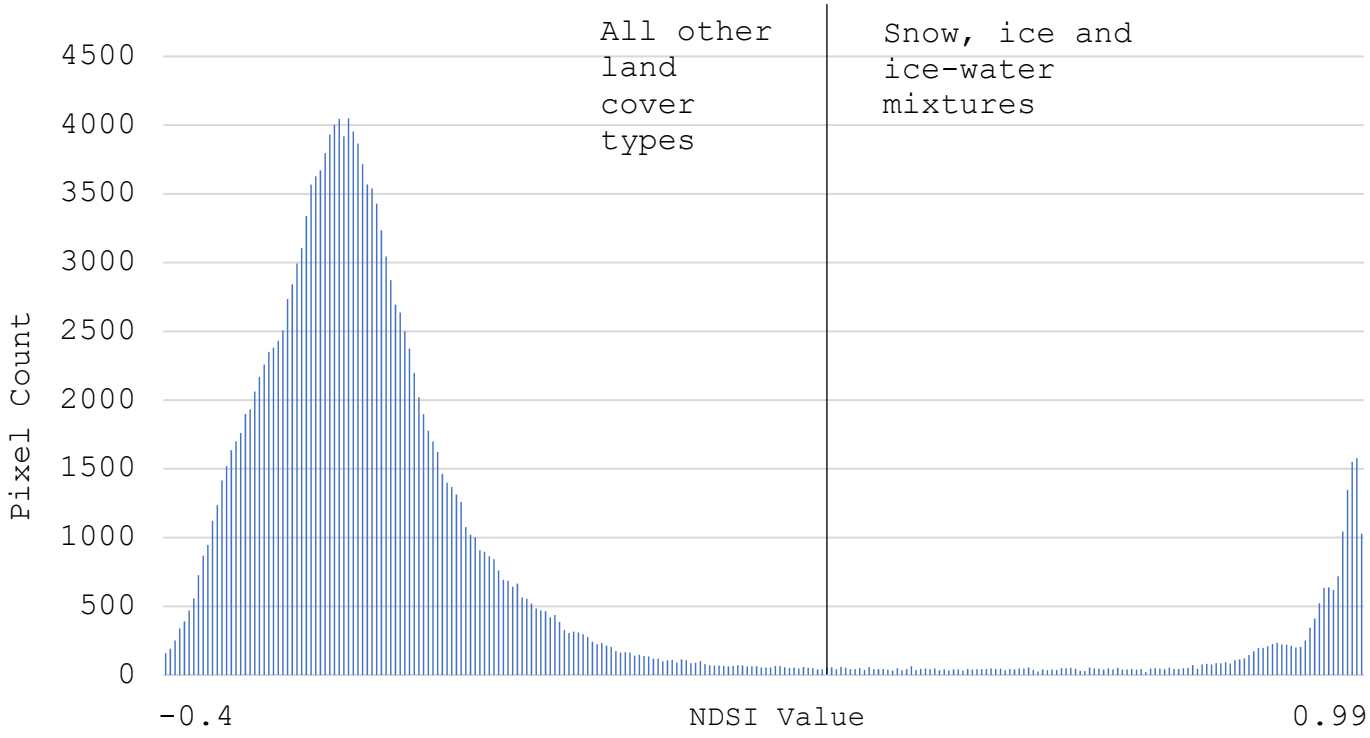

Figure 11. NDSI Result histogram, indicating threshold value of 0.4 (shown for 2016).

The Maximum Difference Snow and Ice Index was then applied to the NDSI result for each year. This index allows ice to be separated from snow (if present) and turbid/marl water:

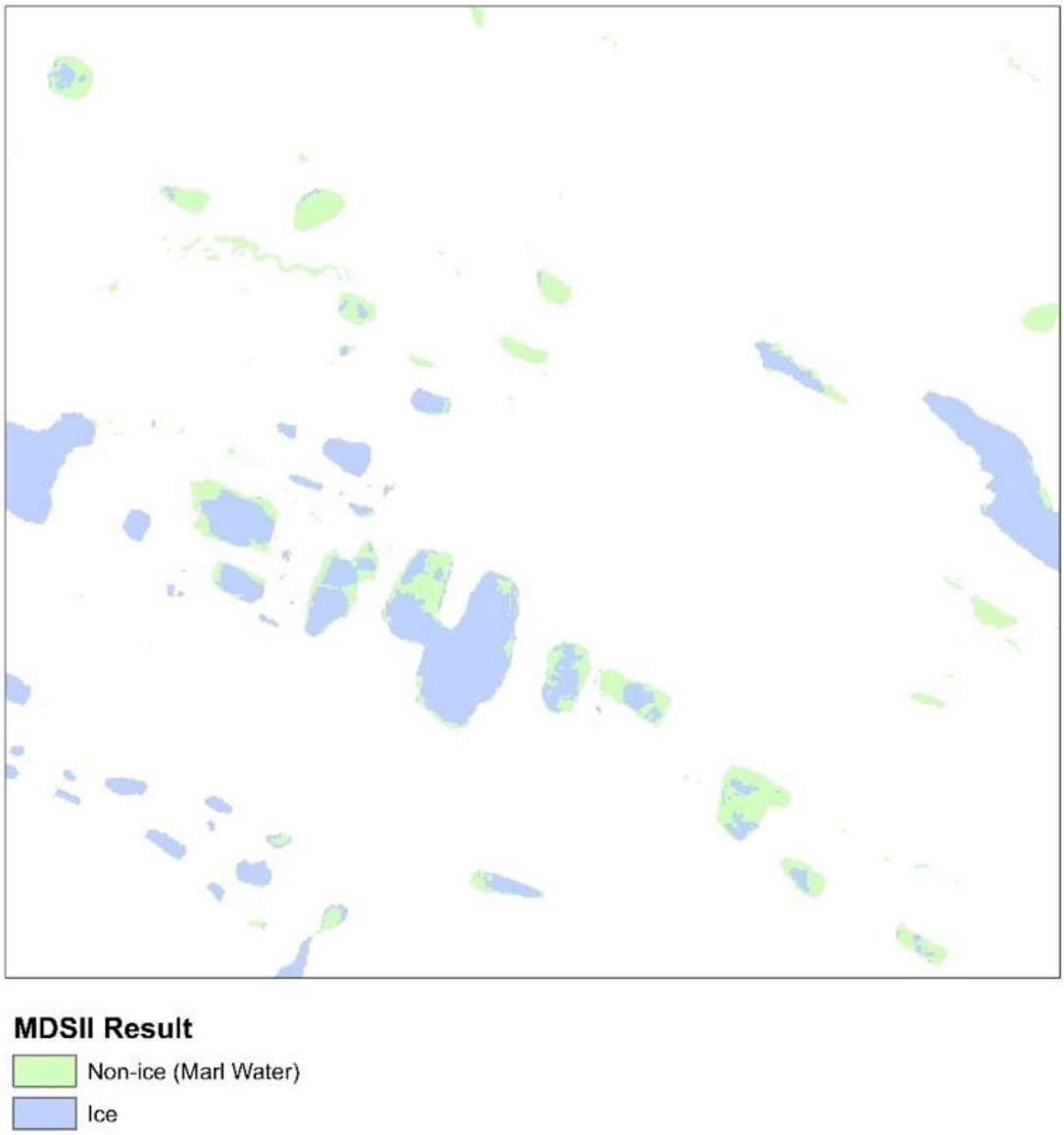

Figure 12. MDSII Result (shown for 2016).

As with the NDSI distribution, the MDSII distribution is also bimodal. However, the threshold value used for the MDSII is 144 (or 0.144 if rescaled):

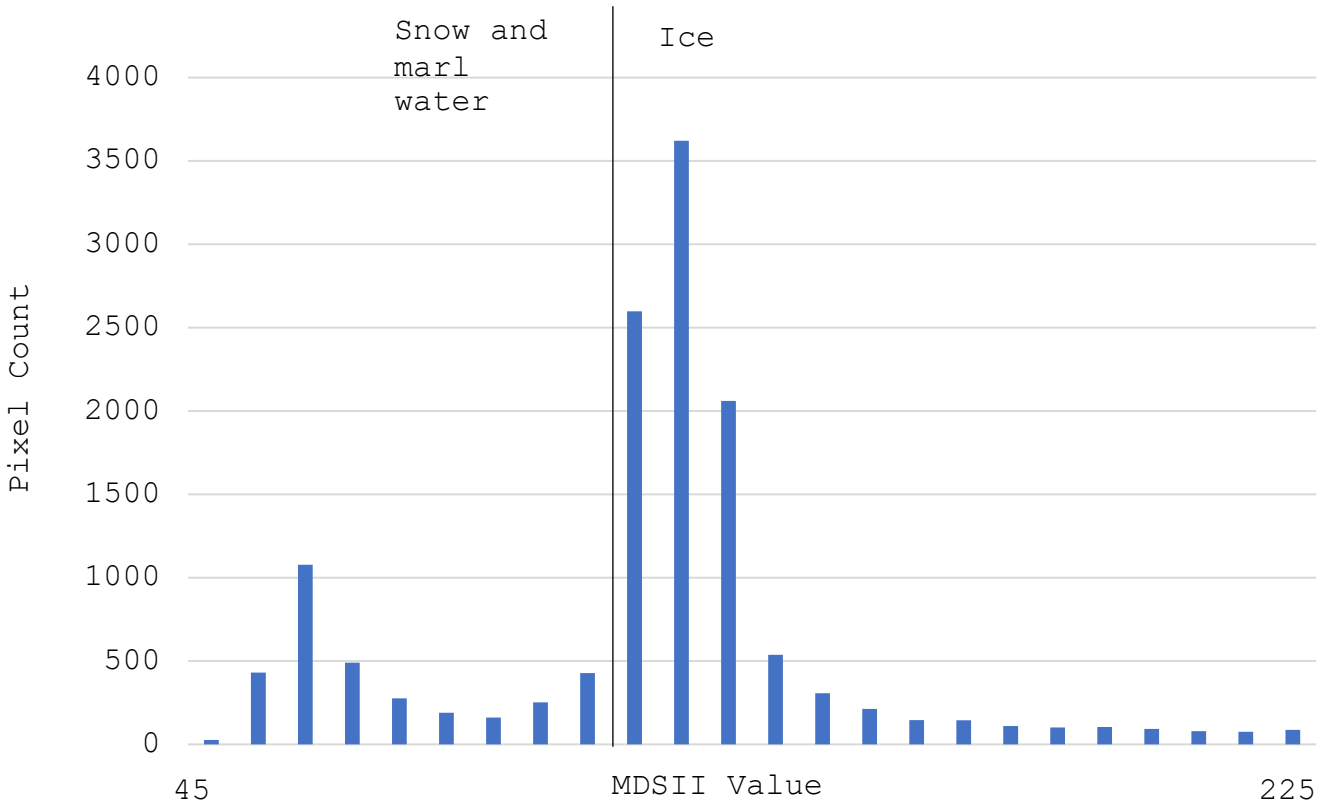

Figure 13. MDSII histogram reduced to show threshold differentiation (shown for 2016).

Once ice features were discriminated, the Normalized Difference Water Index result, shown below, was used to create a water to mask that was then used to eliminate lake and river ice. This is the final step in obtaining the icing distribution.

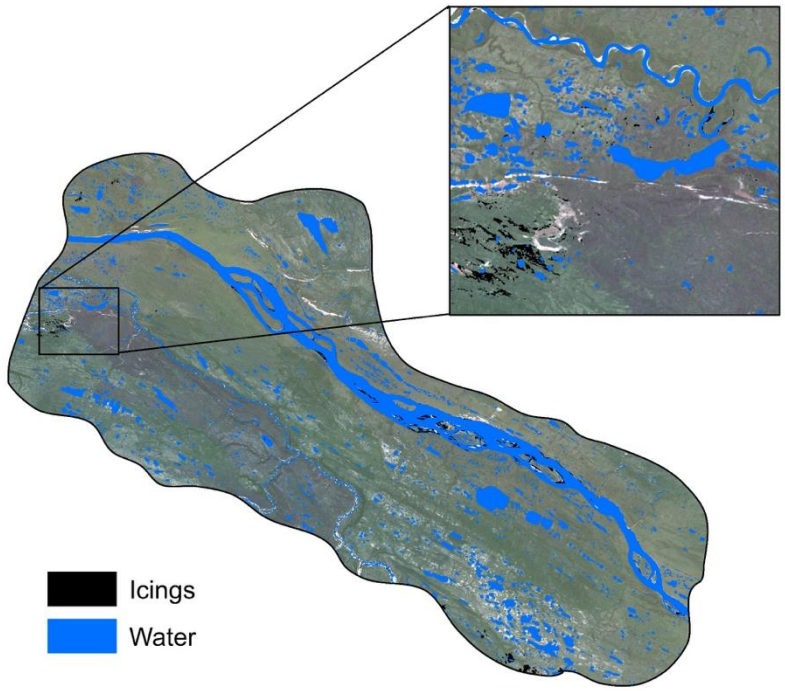

Figure 14. Result of NDWI with icings overlain (shown for 2016).

To delineate thermal anomalies, a Normalized Difference Vegetation Index was created in order to subtract the effects of vegetation from the land surface temperature result. The NDVI result, shown below, provides an idea of regions which contain the most photosynthetically active vegetation (high NDVI index).

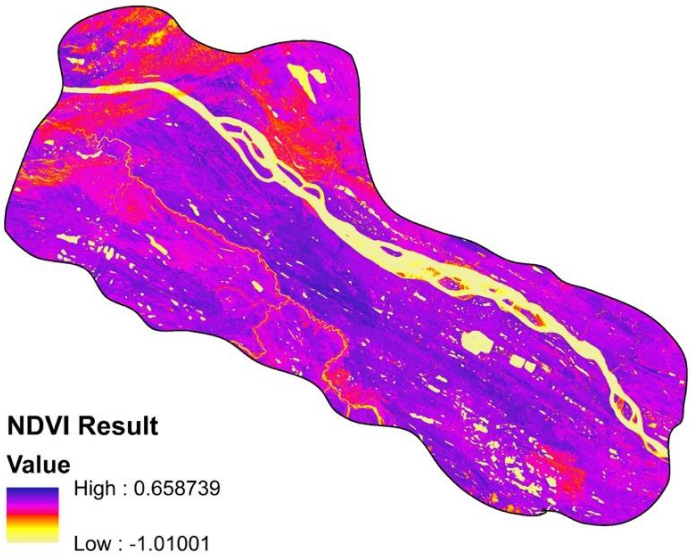

Figure 15. 2016 NDVI Result.

Water pixels are shown to have the lowest NDVI, and forested plateaus are expected to have the highest NDVI. Mid-range NDVI values, though not confirmed by field data, are expected to be attributed to bogs or fens. Such areas can be seen in Figure 15 on the floodplains surrounding the Mackenzie River's tributaries.

The land surface temperature (LST) and standardized LST (Z-scores), are shown in Figure 16. At this point, warmest areas on the LST map are hypothesized to be associated with discharging groundwater. Coldest areas, once water features were removed, were expected to be either inactive icings or snow cover. Effects of thermal inversion and topography are discussed later in this section.

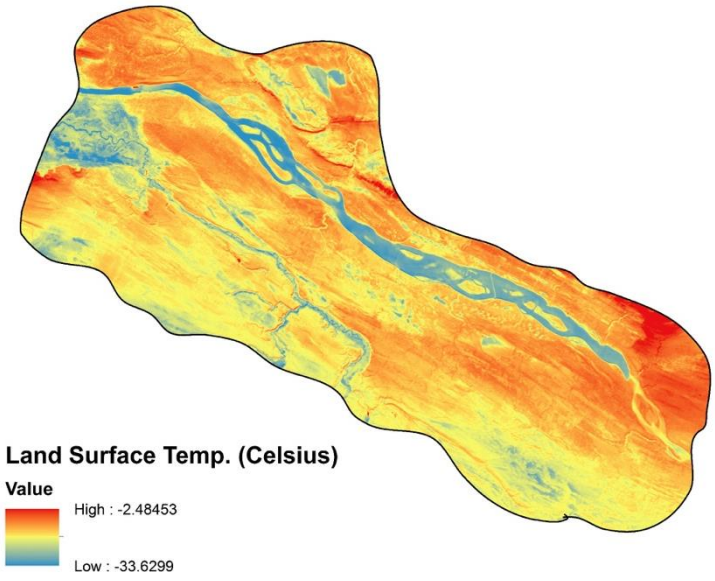

Figure 16a. Land Surface Temperature Result, 2016.

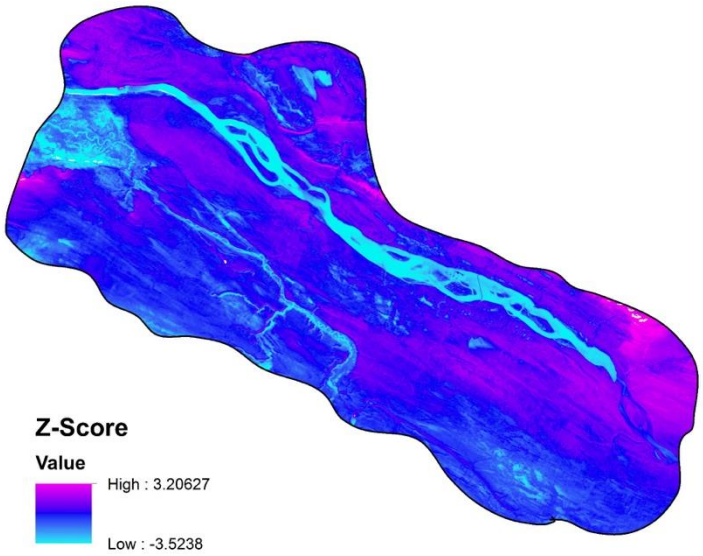

Figure 16b. Z-Score Result, 2016.

Prior to the standardization of the LST result, the KS Normality Test was used to confirm that the temperature distribution came from an acceptably normal population. This was required in order to standardize the data. The actual distribution was compared to what the data should be if it were from a standard normal distribution. If the maximum difference between any two values of X from these distributions exceeded the KS Test's critical value, the data could not be

normal. The critical value for the sample used was 0.136. The maximum absolute difference between these two functions was 0.100, 0.131, and 0.129 for years 2016, 2009, and 2004 respectively. All of the temperature samples were therefore normal, and the results of the KS test on these samples was extrapolated to the entire data set. Modified Normal Q-Q plots are shown in Figure 17 below comparing the values of Sn(x) to F(x) for each year.

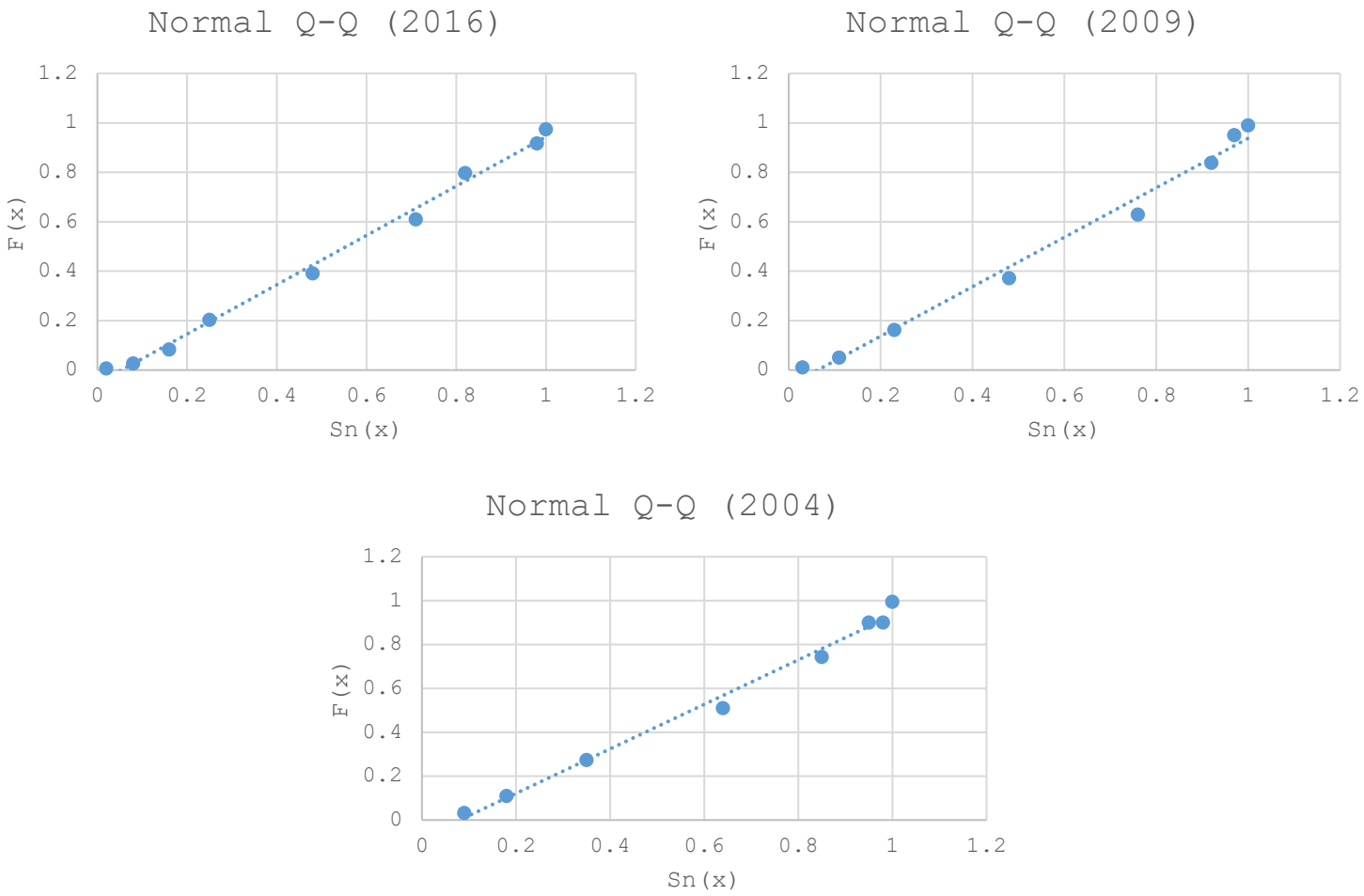

Figure 17. Normal Q-Q plots comparing the measured cumulative distribution function [Sn(x)] to the normal cumulative distribution function [F(x)] for years 2016, 2009, and 2004.

Visually, the Normal Q-Q plots for each year appear very similar. Extreme outliers may have been given by features such as cold clouds, however, any features which were assumed to be outliers were removed from the temperature distribution prior to analysis. Further analysis using the Normal Q-Q plots was therefore not performed.

2.5.2 Icing Occurrence in the Central Mackenzie Valley

The number of discrete icings, as well as the areal extent of icings, was calculated for each year from Landsat imagery for the entire CMV (2004, 2009, and 2016). A subset of this result, underlain by the thermal anomalies, is shown in Figure 18; the distribution of icing count and areal extent compared to thermal anomalies is shown in Figure 19. Icings separated by one or more pixels are considered to be discrete. It is possible that icings within close proximity to one another were part of a larger icing that degenerated, however, this cannot be definitively determined from the imagery. The total areal extent of all icings is 35, 34, and 32 square kilometers for years 2016, 2009, and 2004 respectively. The occurrence of icings, by count as well as by areal extent, was compared to the occurrence of thermal anomalies using a Chi-squared goodness of fit test. The initially continuous distributions of the thermal data were converted to categorical data following the conversion to Z-scores, thus the Chi-squared test is appropriate.

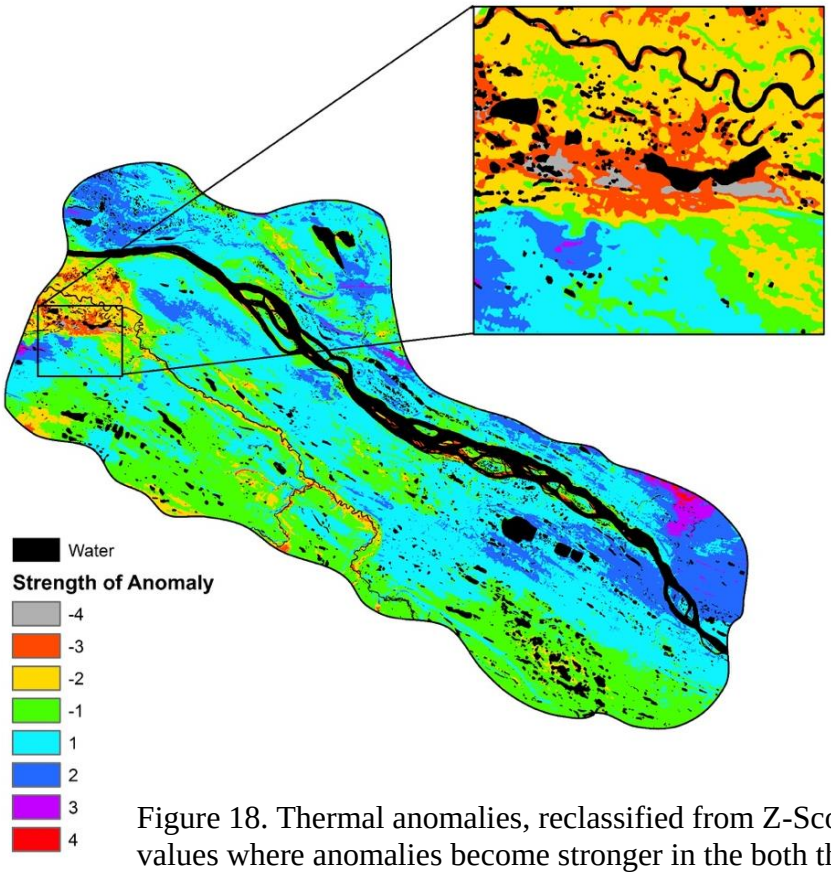

Figure 18. Thermal anomalies, reclassified from Z-Scores to integer values where anomalies become stronger in the both the increasing positive and negative directions.

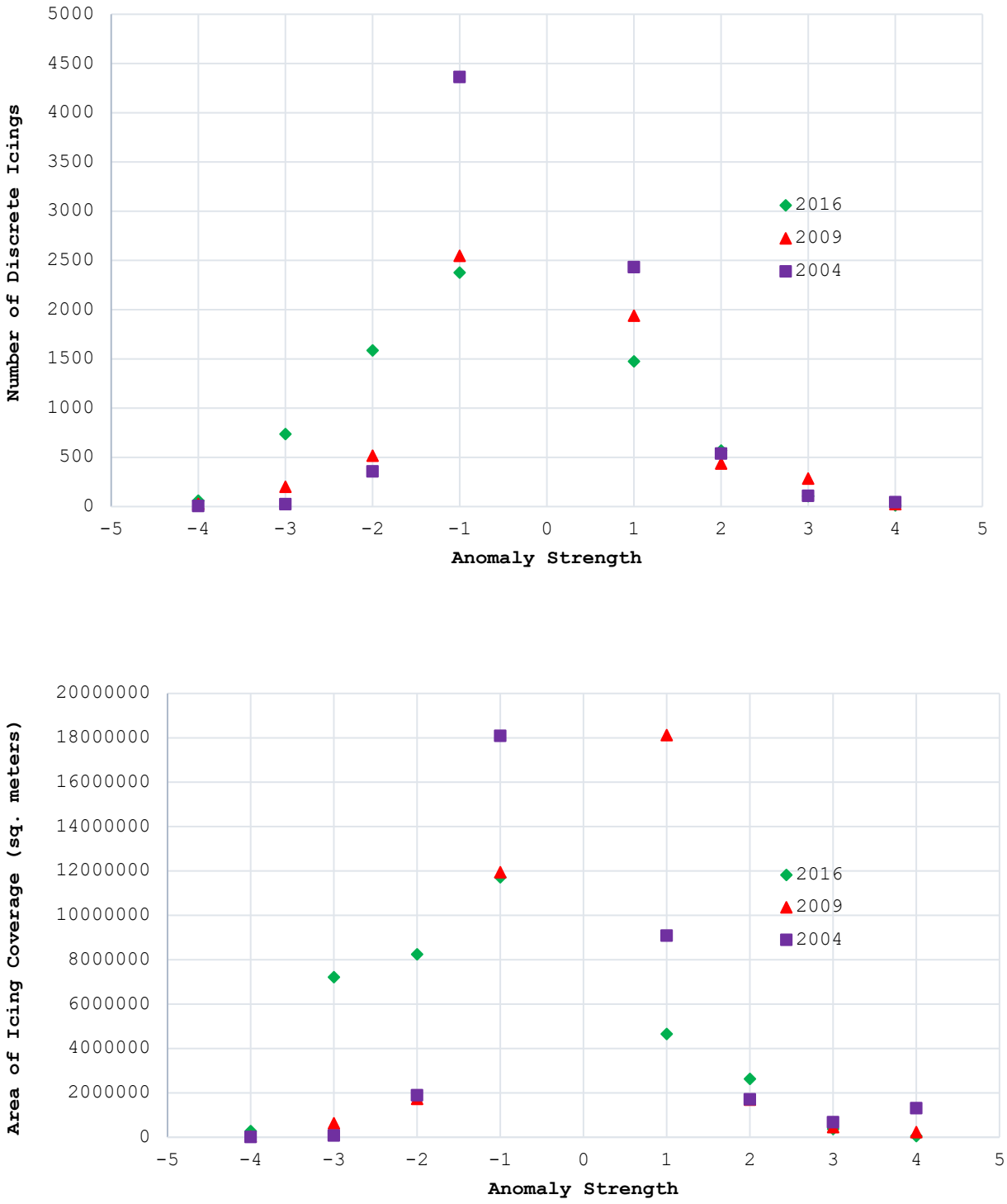

Figure 19. Distribution of icings by count (top) and by areal extent (bottom) in relation to thermal anomalies.

The Chi-Squared test is performed using the data from the current year (t_1) as the observed values, and the data from the previous year (t_0) as the expected values. Therefore, the null and alternate hypotheses are stated as follows:

H_0: There is no significant difference between the observed values of icing count or areal extent when compared to the previous year.
H_1: There is a significant difference between the observed values of icing count or areal extent when compared to the previous year.

There are 8 categories of temperature, and therefore 7 degrees of freedom. A significance level of 0.05 is chosen to perform the test; this corresponds to a critical value of 14.07. For all four tests performed (summarized in Table 3), the value of the test statistic (X^2) is greater than the critical value. Therefore, the null hypothesis is rejected and there is a significant difference in the distributions of icing count and areal coverage from the previous year in all four cases. The Chi-Squared distributions are shown in Figure 20, and are tabulated in Appendix C.

Table 3. Results of Chi-Squared tests.

Test Description	**Test Statistic**	**Outcome**
Comparison of icing count in 2016 to icing count in 2009	3291.93	Reject H_0
Comparison of icing count in 2009 to icing count in 2004	2884.01	Reject H_0
Comparison of icing areal coverage in 2016 to icing areal coverage in 2009	105741202.9	Reject H_0
Comparison of icing areal coverage in 2009 to icing areal coverage in 2004	15342889.8	Reject H_0

It is observed that, overall, there is greater variation in both the discrete icing count and size between the years of 2016 and 2009 than between the years of 2009 and 2004. This is explored further in the discussion to follow.

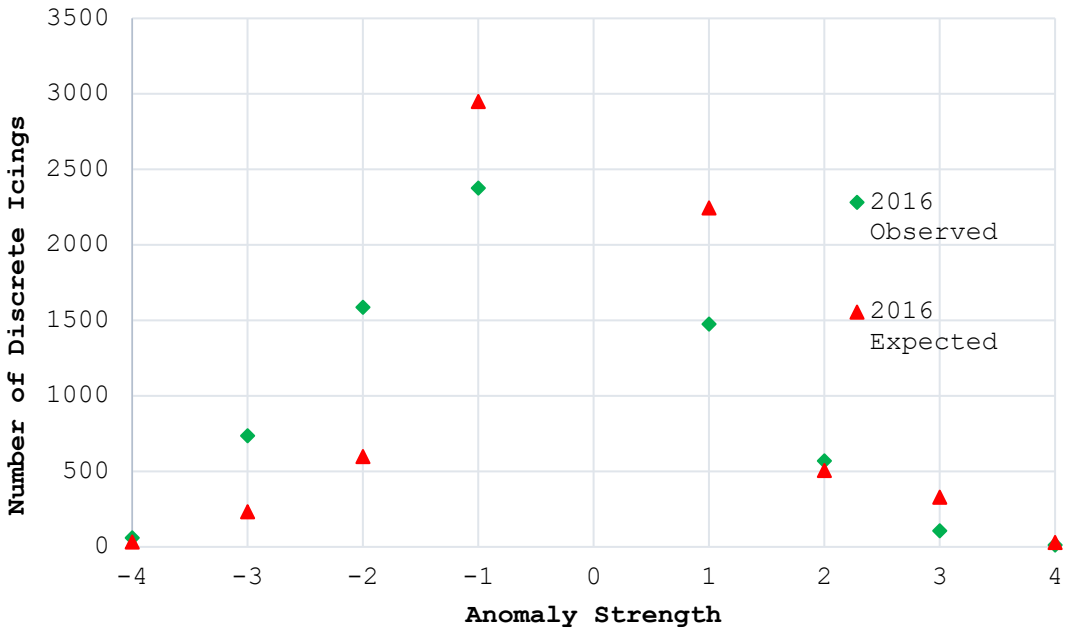

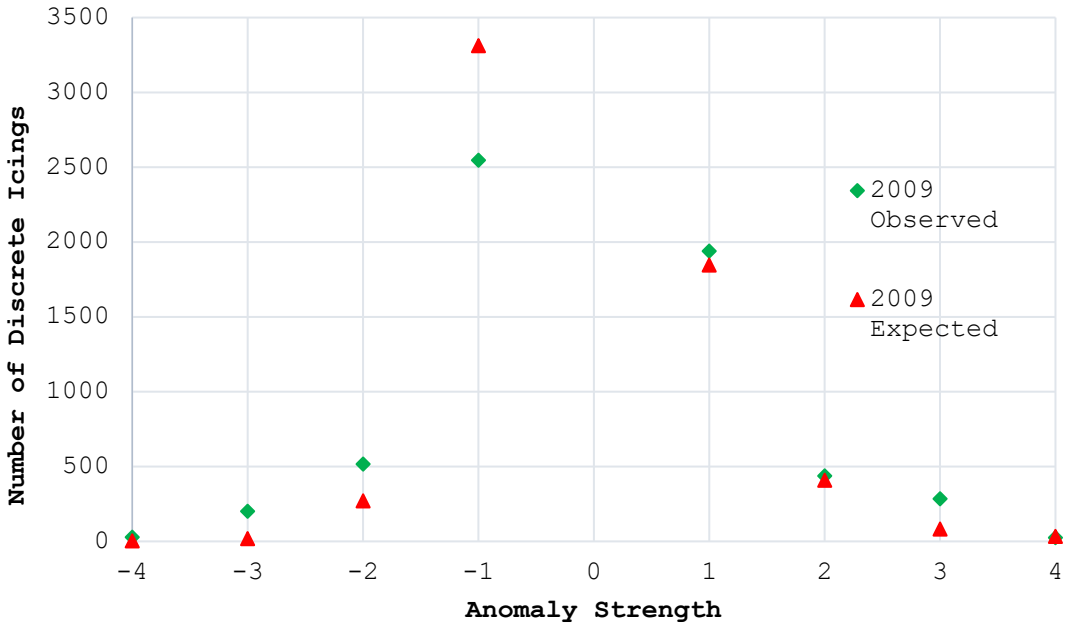

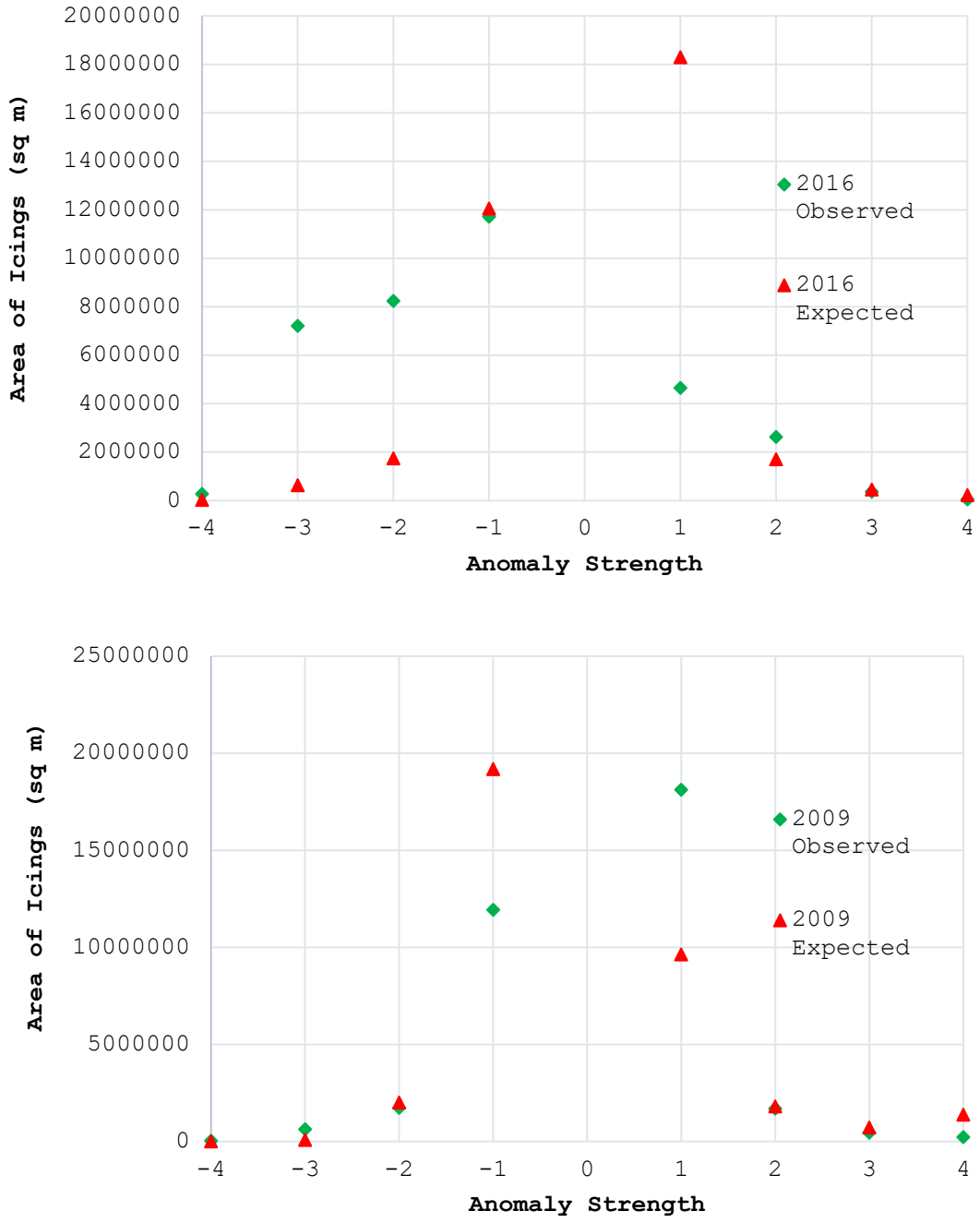

Figure 20. Chi-Squared distributions for the comparison of discrete icing size to thermal anomalies for 2016 and 2009 (top); comparison of areal icing coverage to thermal anomalies for 2016 and 2009 (bottom).

Following the Chi-squared analysis, the discrete icing count and area covered by icings are compared to each other in order to determine the correlation between overall icing coverage and icing count. As shown in Figure 21 below, there was a very strong positive correlation between icing count and coverage for years 2004, 2009, and 2016. Pearson correlation coefficients, given by SPSS, are greater than 0.9 for all years.

Correlations

		Icings16	Area16
Icings16	Pearson Correlation	1	.924**
	Sig. (2-tailed)		0.001
	N	8	8
Area16	Pearson Correlation	.924**	1
	Sig. (2-tailed)	0.001	
	N	8	8

**. Correlation is significant at the 0.01 level (2-tailed).

		Icings09	Area09
Icings09	Pearson Correlation	1	.910**
	Sig. (2-tailed)		0.002
	N	8	8
Area09	Pearson Correlation	.910**	1
	Sig. (2-tailed)	0.002	
	N	8	8

**. Correlation is significant at the 0.01 level (2-tailed).

		Icings04	Area04
Icings04	Pearson Correlation	1	.996**
	Sig. (2-tailed)		0.000
	N	8	8
Area04	Pearson Correlation	.996**	1
	Sig. (2-tailed)	0.000	
	N	8	8

**. Correlation is significant at the 0.01 level (2-tailed).

Figure 21. Results of correlation analyses performed in SPSS for years 2016 (top), 2009 (middle), and 2004 (bottom).

The results of this correlation analysis indicate that increased icing area coverage is associated with a greater amount of discrete icings. In other words, this region is populated by many small icings, rather than few large ones. This is in contrast to icings which have been observed in more mountainous regions such as the Brooks Range or the Yukon Valley. Here, icings tend to be few and very large.

Icing recurrence, or overlap, for all possible year combinations, is shown in Figure 22. These results were determined by performing an intersect of icings for each overlap range. If an icing was found to be within 30m (one pixel) of an icing from a different year, but not quite overlapping, it was included in the intersect as a way to partially account for effects that topographic variation and snowpack density may play in the surface expression of the icing. Given that the purpose of establishing icing recurrences is to locate priority monitoring sites, an intersect threshold value of 30m is assumed to be reasonable. It is determined that the overlap of icings by area are 28.8, 25.0, and 34.8 percent of the total area for overlap ranges 2016-2009, 2016-2004, and 2009-2004 respectively. The overlap of icings for all years is determined to be 12.5%, or 11.1 square km. These icings represent the highest potential for in situ monitoring as they give evidence of recurring groundwater discharge.

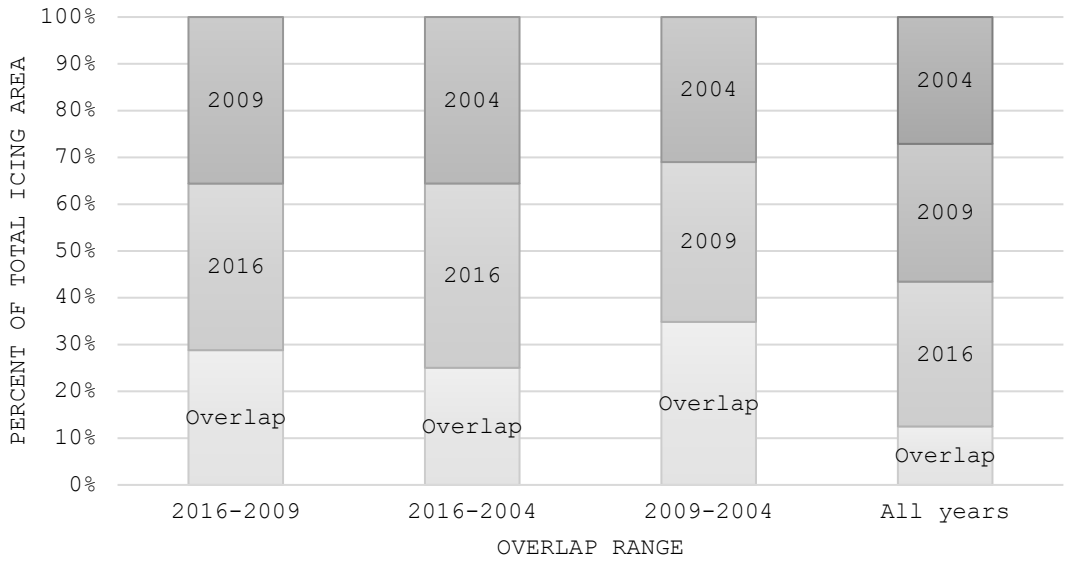

Figure 22. Icing overlap (recurrence) for each possible year combination as a percent of total icing area.

The three-year recurring icings are examined in greater detail as they represent the most promising locations for field monitoring sites, and they are the only icings which can be compared year to year for their representation in thermal anomalies. The strong anomalies (2, 3, 4, -2, -3, -4), which, because they have been converted to z-scores, will always represent approximately 32% of the scene, are amalgamated into strong warm, and strong cold zones. They are then compared to the three-year recurring icing count and areal extent as shown in Table 4. The weak (-1, 1) anomalies are not considered in this comparison; if recurring icings are able to be identified based on winter thermal anomalies, it should be because they are correlated with strong anomalies only. This is considered further in the discussion.

Table 4. Comparison of the area represented by strong anomalies to the discrete count of icings in those areas and the percent area of total icings.

Year	**Warm Area (sq. m)**	**Cold Area (sq. m)**	**Warm Icings***	**Cold Icings***	**Warm Icings (%)**	**Cold Icings (%)**
2016	131722	8292388	121	1097	74.9	6.9
2009	395491	661477	81	235	5.9	4.1
2004	1759459	1186829	260	127	10.7	13.3

** Discrete count of icings occurring separately within strong warm and strong cold zones*

2.5.3 Icing Occurrence in the Bogg Creek Watershed

Following the examination of icings using Landsat 4-5 TM and Landsat 8 OLI datasets, it was determined that it would be beneficial to examine icings in greater detail using higher resolution imagery for just the Bogg Creek Watershed. This region is the proposed site of future field work. Unfortunately, acquiring high resolution imagery for the same dates as the Landsat imagery was not possible due largely to cloud interference with image acquisition. One image from the late spring of 2017 (May 14th) was obtained from RapidEye-3 through Planet Labs (2018). Upon visual inspection of the icings result from the Landsat data (2004, 2009, and 2016) and

RapidEye-3 data (2017), a recurring icing complex was identified within the Bogg Creek Watershed. This is shown in Figure 23 below. The main icing in this complex is very evident in 2004 and 2009, but not in 2016 or 2017. In 2016, there appears to be several smaller icings surrounding the lakes, and in 2017 the icings are negligible.

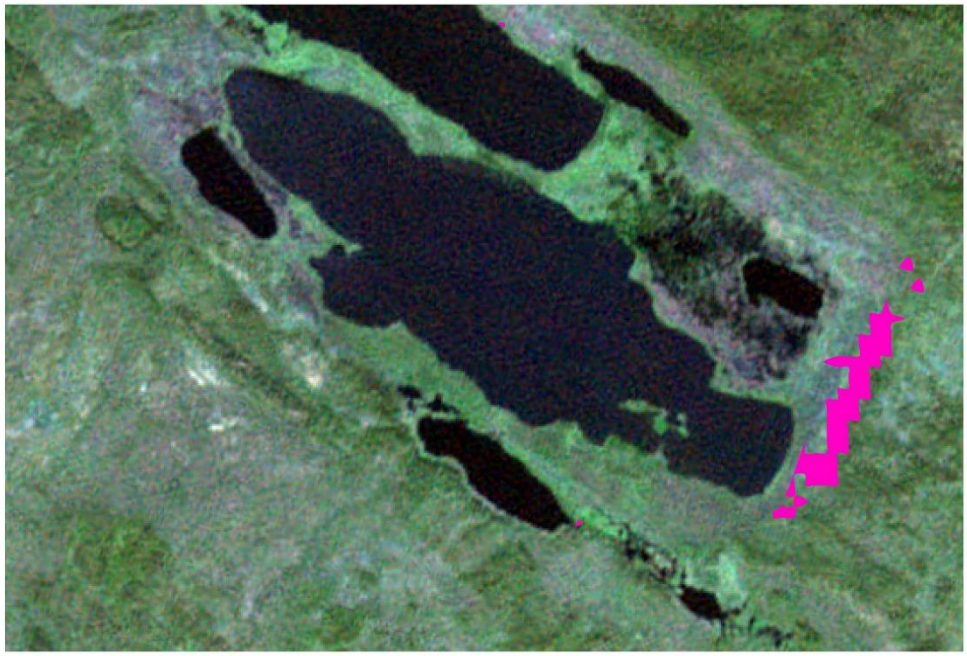

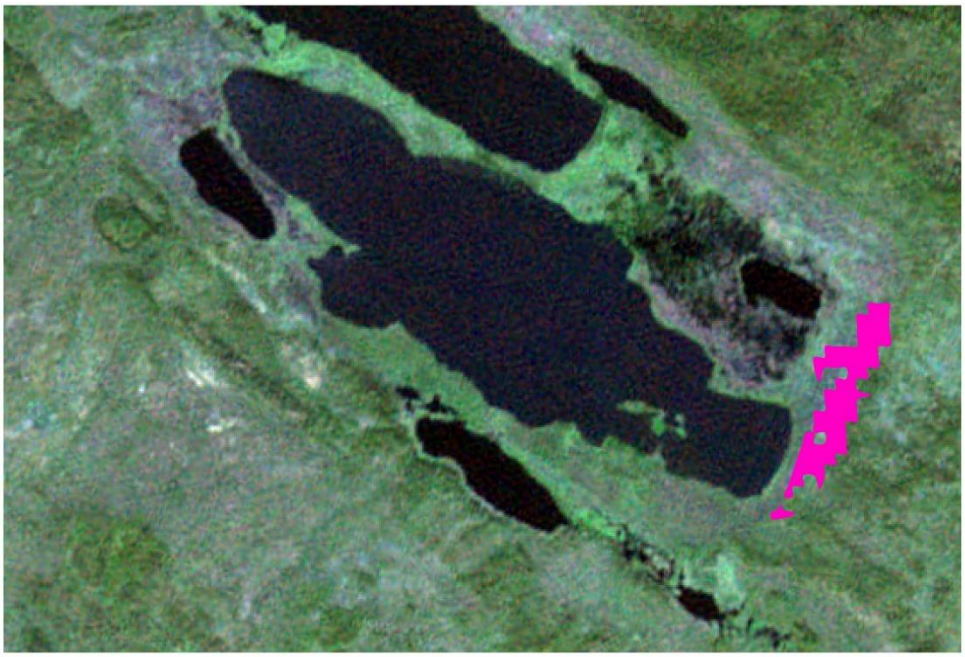

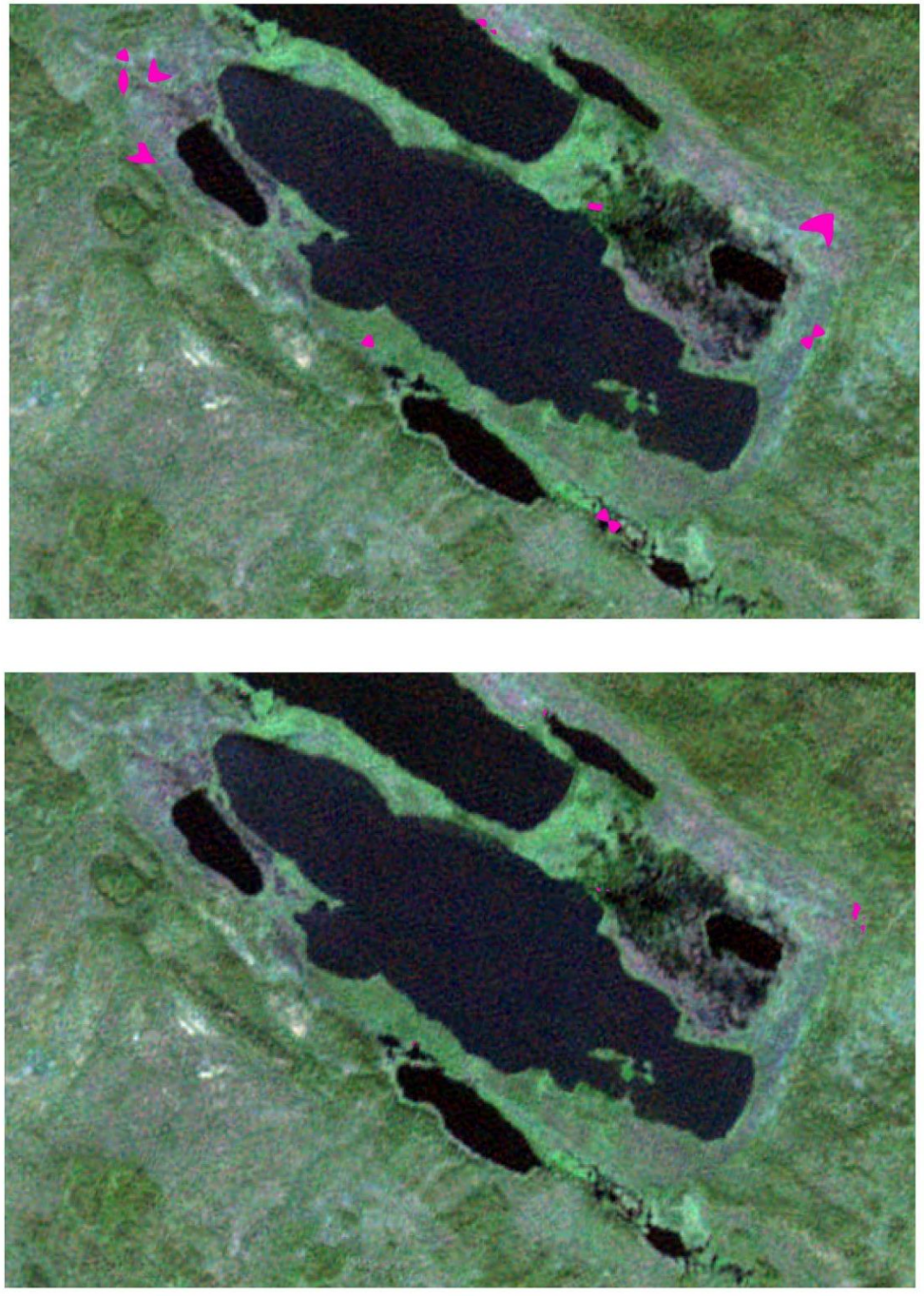

Figure 23. Development of the Bogg Creek Icing Complex (icings shown in pink) from 2004 (top), 2009 (2nd from top), 2016 (3rd from top) and 2017 (bottom) shown with Rapid Eye-3 imagery sourced from Planet Labs.

Icings within the Bogg Creek watershed are of greatest interest for in situ examination. It is expected that of the icings detected in this watershed from all four sampled years, ones which are most likely to exist presently are those which were recurrent in all four sampled years, and/or those which have appeared more recently. Table 5 below categorizes the Bogg Creek icings by which years they appeared in, size for each year that they appeared, whether or not they have been recurrent from 2004-2017, and by whether or not they belong to the main icing complex identified in Figure 23.

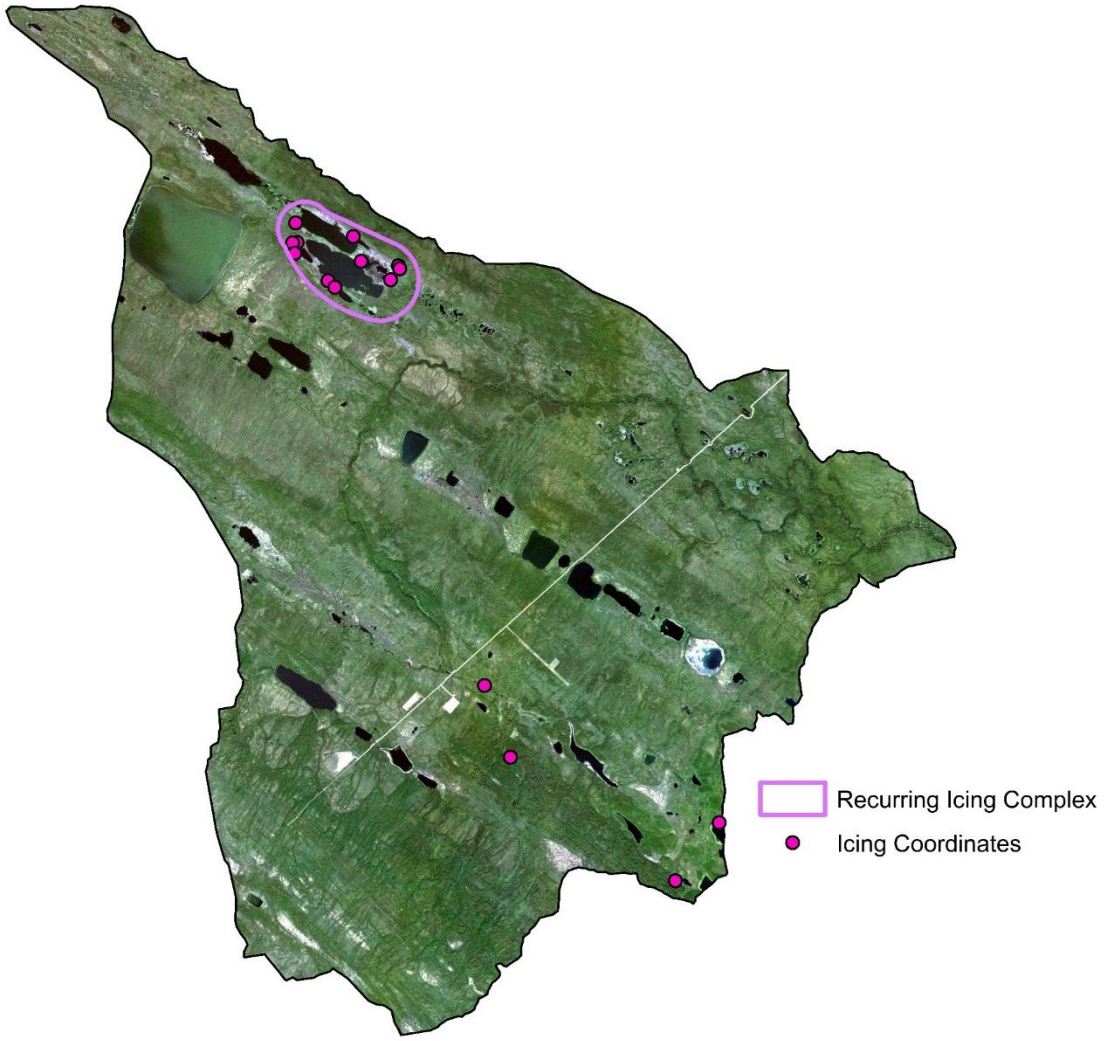

Figure 24. Priority monitoring locations in the Bogg Creek Watershed, given by center coordinates of icings and summarized in Table 5 below (shown with Rapid Eye-3 imagery sourced from Planet Labs).

Table 5. Priority monitoring icings located in the Bogg Creek Watershed between years 2004 and 2017.

Icing	**2016 Size (m^2)**	**2017 Size (m^2)**	**[l]Part of Recurring Complex**	**[Ł]Present in 2004**	**[Ł]Present in 2009**	**[Ł]Coordinates (W)**	**[Ł]Coordinates (N)**
0	4490	720	Yes	Yes	No	126°27'03" W	65°05'19" N
1	Not present	162	Yes	Yes	No	126°27'01" W	65°05'17" N
2	1200	Not present	Yes	Yes	Yes	126°27'16" W	65°05'10" N
3	589	108	Yes	No	No	126°28'01" W	65°05'23" N
4	916	Not present	Yes	No	No	126°28'54" W	65°05'11" N
5	2053	Not present	Yes	No	No	126°29'40" W	65°05'37" N
6	1153	Not present	Yes	No	No	126°29'47" W	65°05'37" N
7	2447	Not present	Yes	No	No	126°29'44" W	65°05'30" N
8	3000	Not present	Yes	No	No	126°29'41" W	65°05'50" N
9	7800	Not present	No	No	No	126°19'18" W	64°59'03" N
10	5005	Not present	No	No	No	126°20'30" W	64°58'26" N
11	916	Not present	No	No	No	126°25'15" W	65°00'40" N
12	916	Not present	No	No	No	126°24'39" W	64°59'52" N
13	Not present	91	Yes	No	No	126°28'43" W	65°05'06" N
14	Not present	178	Yes	No	No	126°28'11" W	65°05'39" N

[Ł]at center of most recent observation (2017), [Ł]within 100m of the most recent observation (2017)
[l]Icings which are part of the recurring complex should be given greatest consideration. Though icings may not recur in the same precise location, the recurring icing complex represents an area which has significant potential for groundwater discharge.

2.5.4 Relationships between Icings and Surficial Geology

Surficial geology datasets, obtained from the Geological Survey of Canada Open File 7289, are also related to the distribution of icings. This is done for two reasons: firstly, as an initial validation of icing occurrence. As icings represent groundwater discharge zones, they should overlie materials which are hydraulically conductive, which are close to the water table, or are conductive via fractures (fractures may be present in impermeable bedrock). Secondly, understanding the relationship between geological features and icings provides important information regarding the dynamics of the flow system.

Primary texture classification is extracted from this dataset and compiled for the study area, shown in Figure 25. As shown in Figure 26, the greatest proportion of icings, by area and count, is found in bedrock outcrops and sand for all years considered. The same is true of the size of icings; largest icings are located within bedrock outcrops and sand.

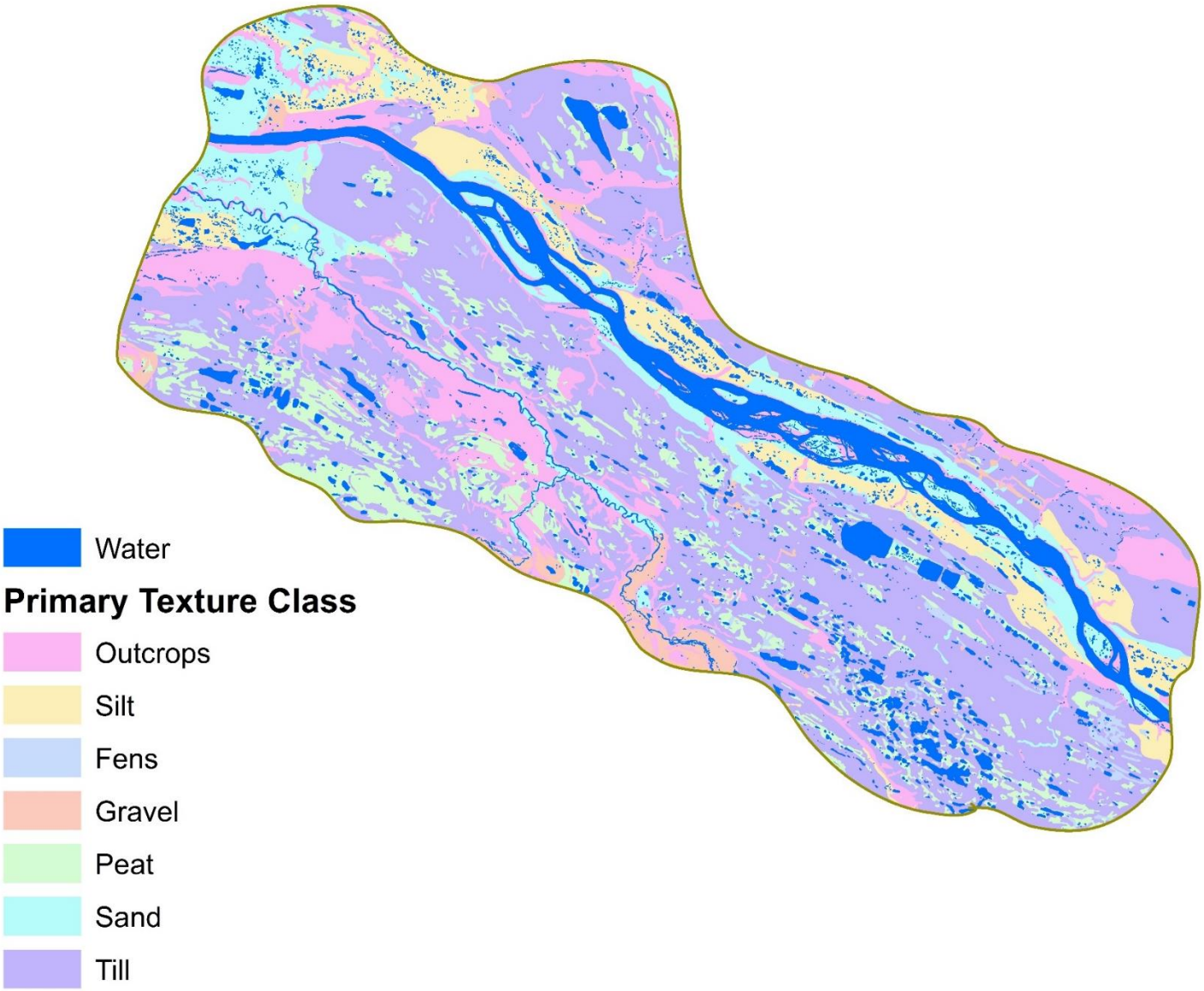

Figure 25. Primary surficial texture classification for the Central Mackenzie Valley obtained from the Canadian Geologic Survey.

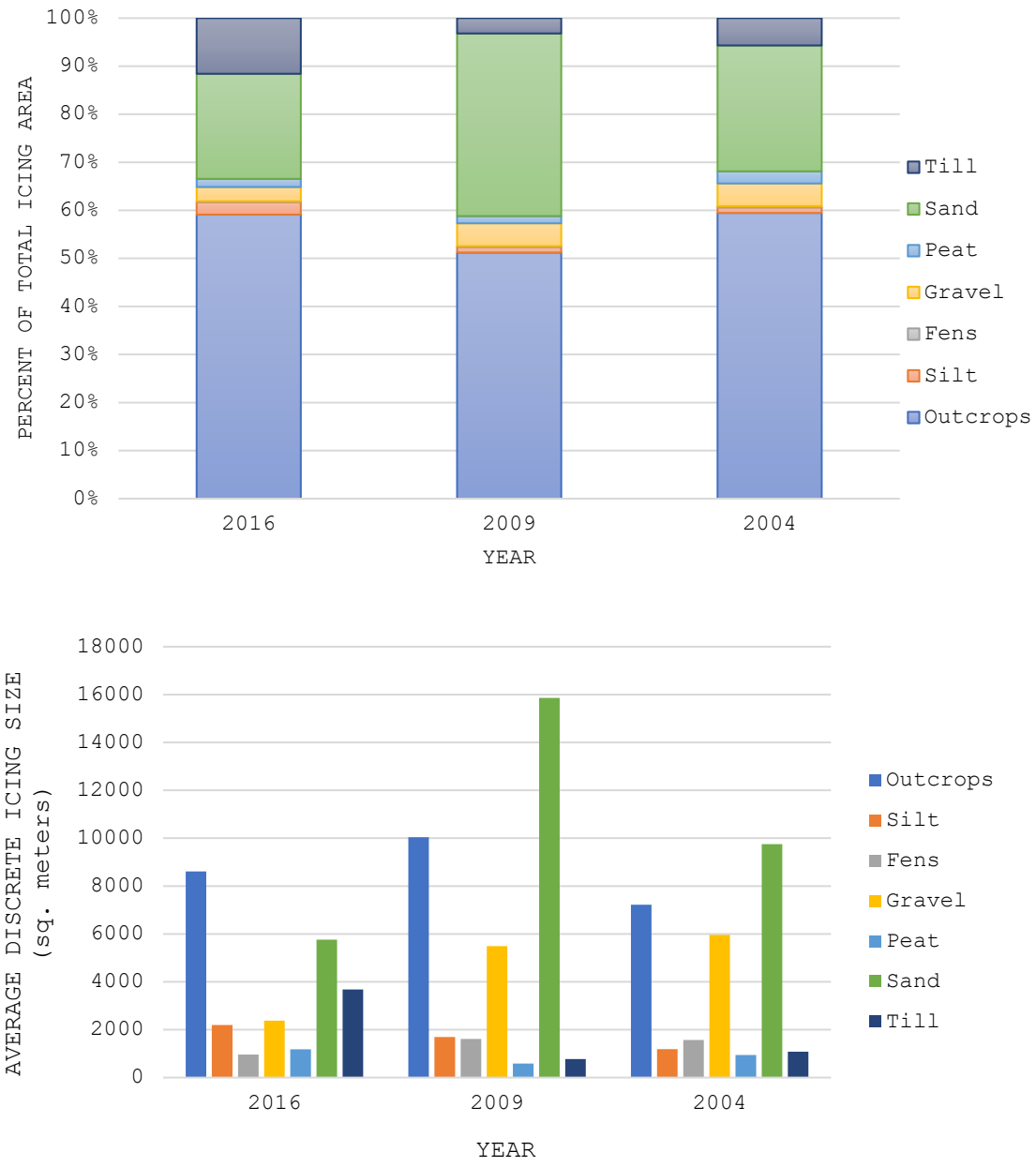

Figure 26. Percent of total icing area for each year (left), and average discrete icing size for each year (right) compared to the primary surficial texture class.

For Bogg Creek specifically, the main icing complex is located in a fen. This appears to be an anomaly given that the remaining icings in the Bogg Creek watershed are located over either sand or bedrock outcrops. This is explored further in the discussion.

2.5.5 Field Results

A brief a summary of the field results pertaining to the methods detailed in section 2.4.3 are given here as verification for some of the predicted icing locations. Not all locations could be visited, but those that were visited and sampled are discussed here.

GW-SW Temperatures and Thermal Imagery: Within approximately 40m and 100m of Icing ID 0 and 1 respectively, (refer to table 5) an average groundwater temperature of 1.7 degrees Celsius at a depth of 1.5m was observed. The average surface water temperature in the same areas was 4.3 degrees Celsius. These measurements provide an estimate of the magnitude of contrast that exists between the shallow subsurface flow system and the surface system. Figure 27 below shows a photograph of a sample being collected from this region, and of the general landscape. Figure 28 shows the same location, as viewed from a thermal camera. It is observed from this thermal image that there is strong agreement between the predicted icing locations (ID 0 and 1) and the cool zones in the thermal image. Zones which are cooler than the surrounding area are represented by reds and oranges.

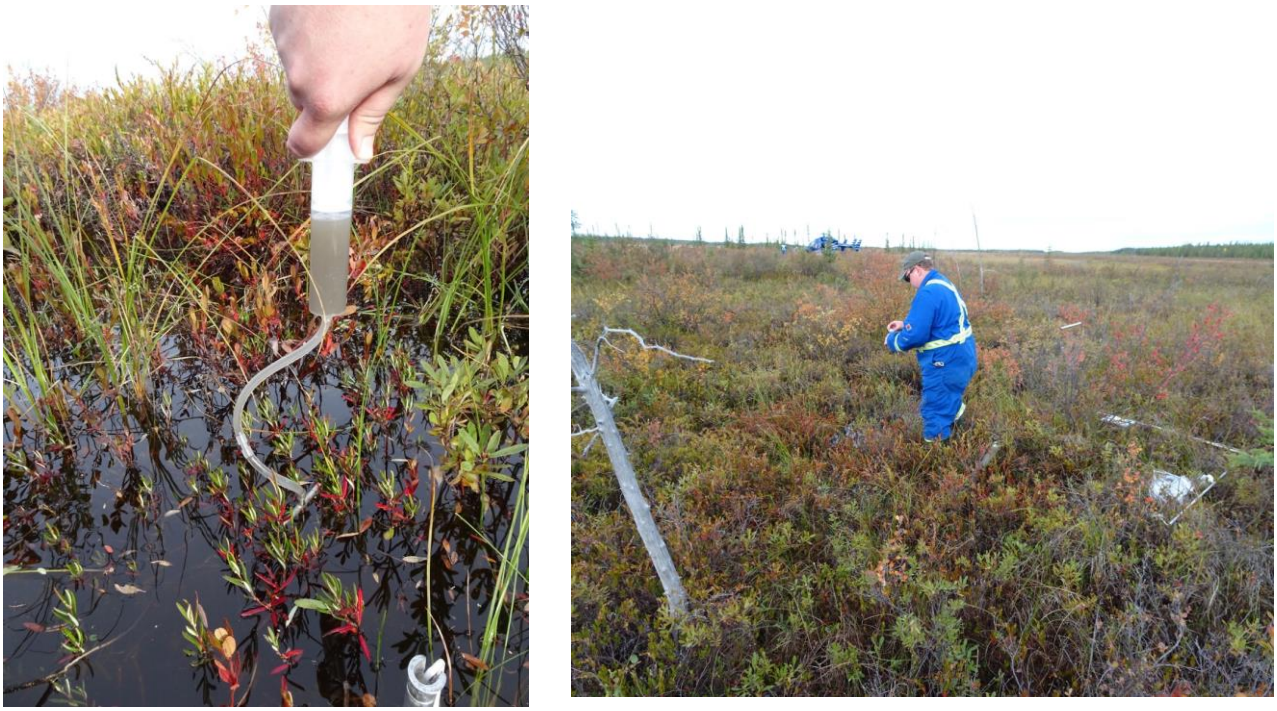

Figure 27. Sample collection performed by Andrew Wicke in the vicinity of Icing ID 0 and 1.

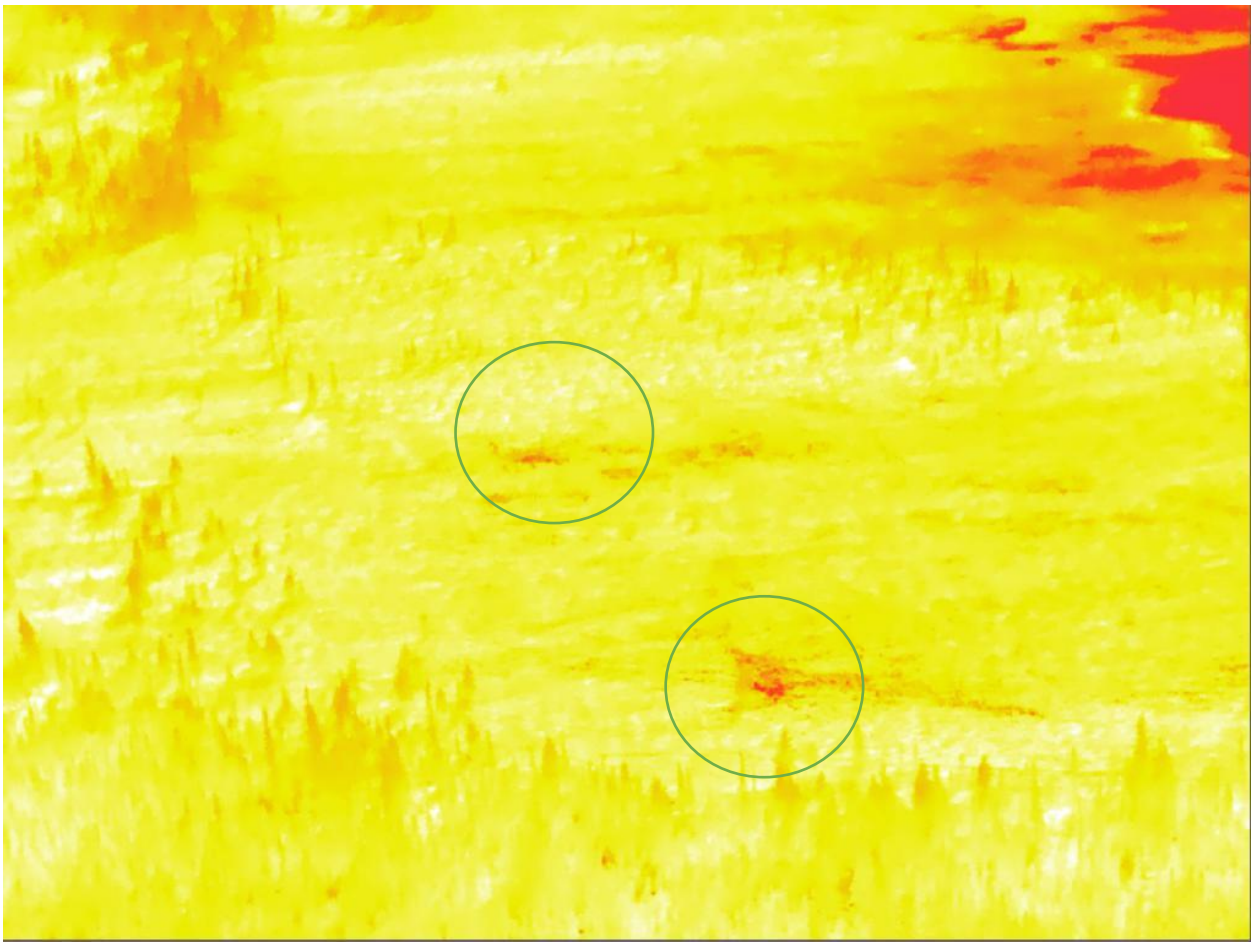

Figure 28. Thermal image collected by Dr. Brewster Conant; cool zones (circled) correspond to icing ID 0 and 1.

Thermal video and imagery were also collected for Icing ID 11, pictured in Figure 29 below. The contrast here between what is presumed to be discharging groundwater is even greater than it is for Icing ID 0 and 1.

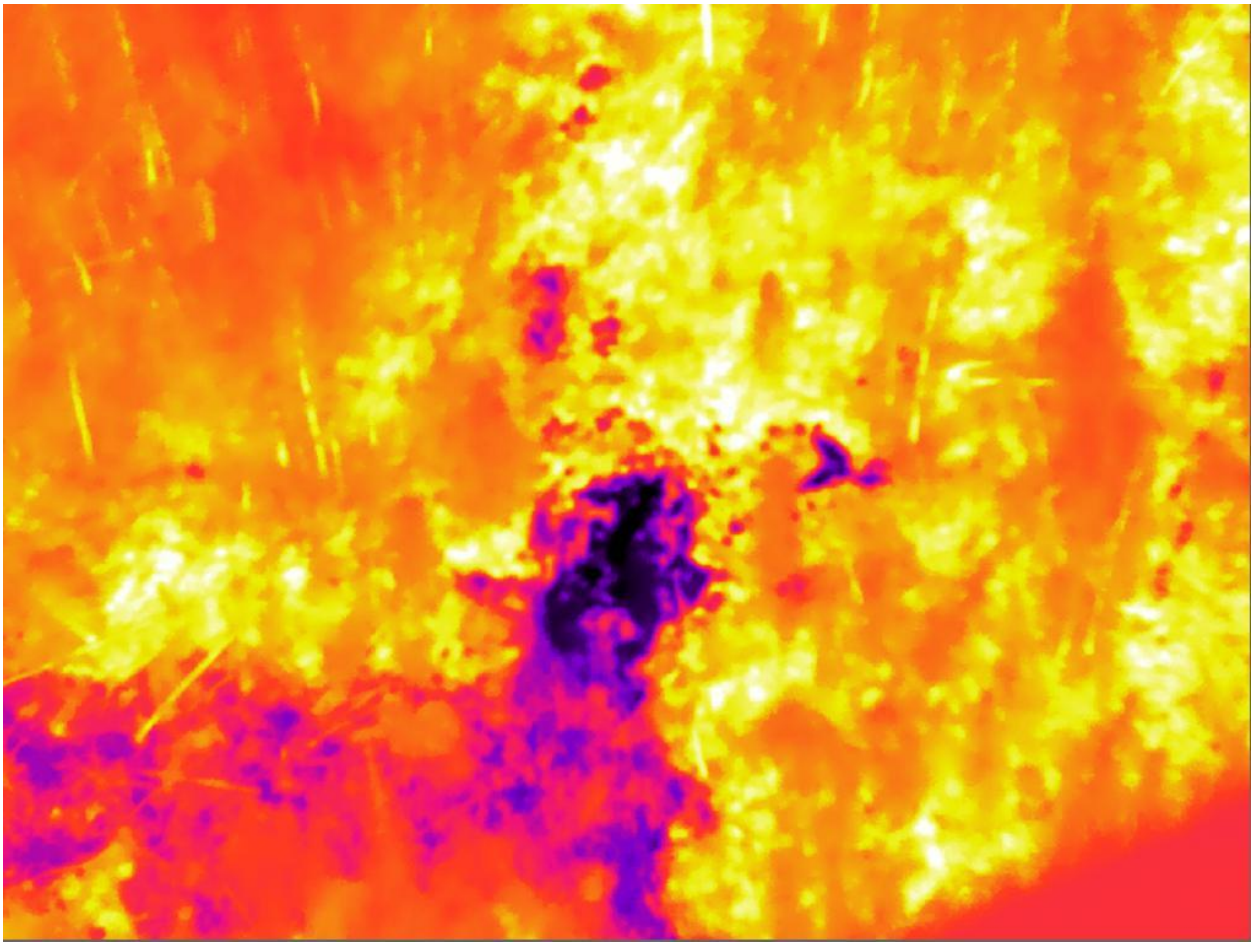

Figure 29. Thermal image collected by Dr. Brewster Conant for Icing ID 11. The icing location (discharging groundwater) is represented by the purple and pink zone.

Electroconductivity (EC) Measurements: EC Measurements for SW in the vicinity of Icing ID 0 and 1 averaged 63 microns/cm. For GW, EC measurements averaged 1629 microns/cm. This result is expected given that much of the bedrock in the area is soluble and therefore is also high in total dissolved solids when compared to surface water. The next field campaign in this region is expected to take place during winter when water can be collected directly from the icings. At this point, the GW EC data could be compared to the icing water EC; this would further verify the source of the icing as groundwater.

Hydraulic Gradient Measurements: Using the Henry Probe, an upward hydraulic gradient of approximately 0.05 cm was observed within the vicinity of Icing ID 0 and 1. This gradient is expected to be a significant contributing factor in the formation of icings in this area. The

presence of this strong upward gradient during the summer indicates that, as hypothesized, the icings in this region are more likely spring type (they are permanent, not intermittent). Additionally, cool water was pooled in topographic lows near the location of the head measurements. This suggests continuous groundwater discharge at the surface.

2.5.6 Results from Image Processing Steps to examine NDVI

As described in the methodology, the first step in locating regions of continually degrading vegetation was to compute the Normalized Difference Vegetation Index for each of the sampled years from 2012-2017. These NDVIs are different than those used for the icings analysis because they are of a higher resolution. 5m RapidEye-3 data was used for the vegetation degradation results shown here, which only cover the Bogg Creek watershed. An example from 2012 and its corresponding histogram are is given below.

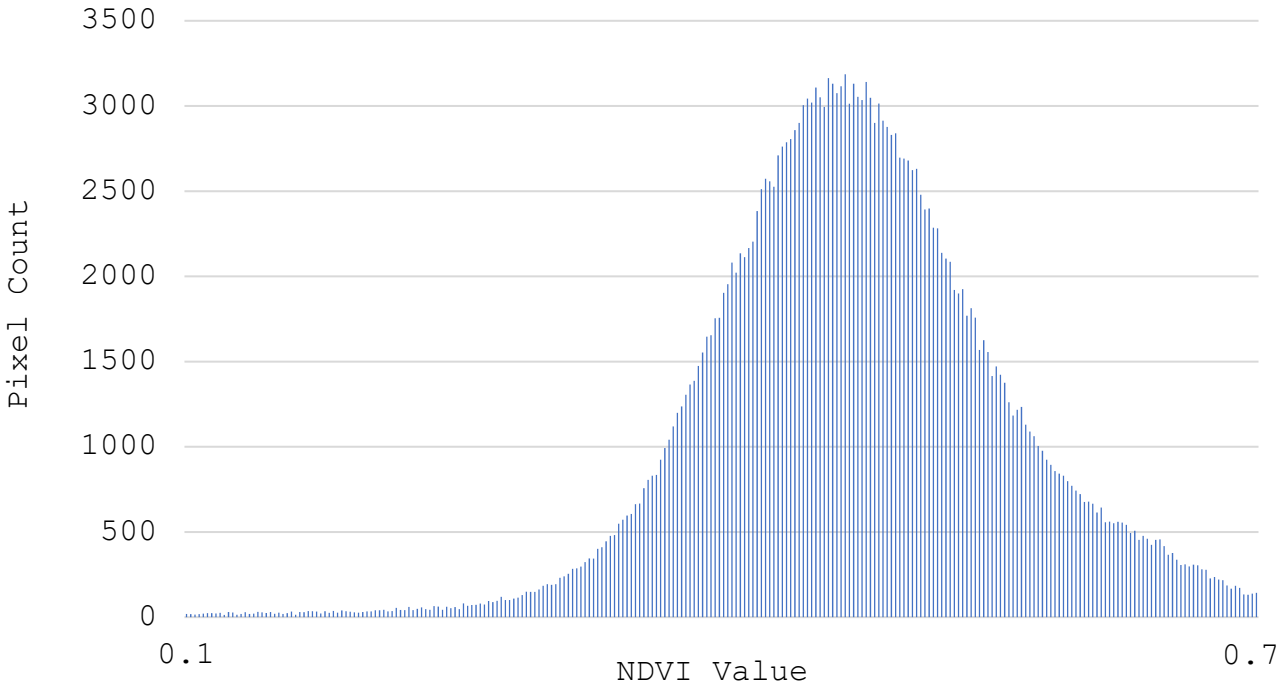

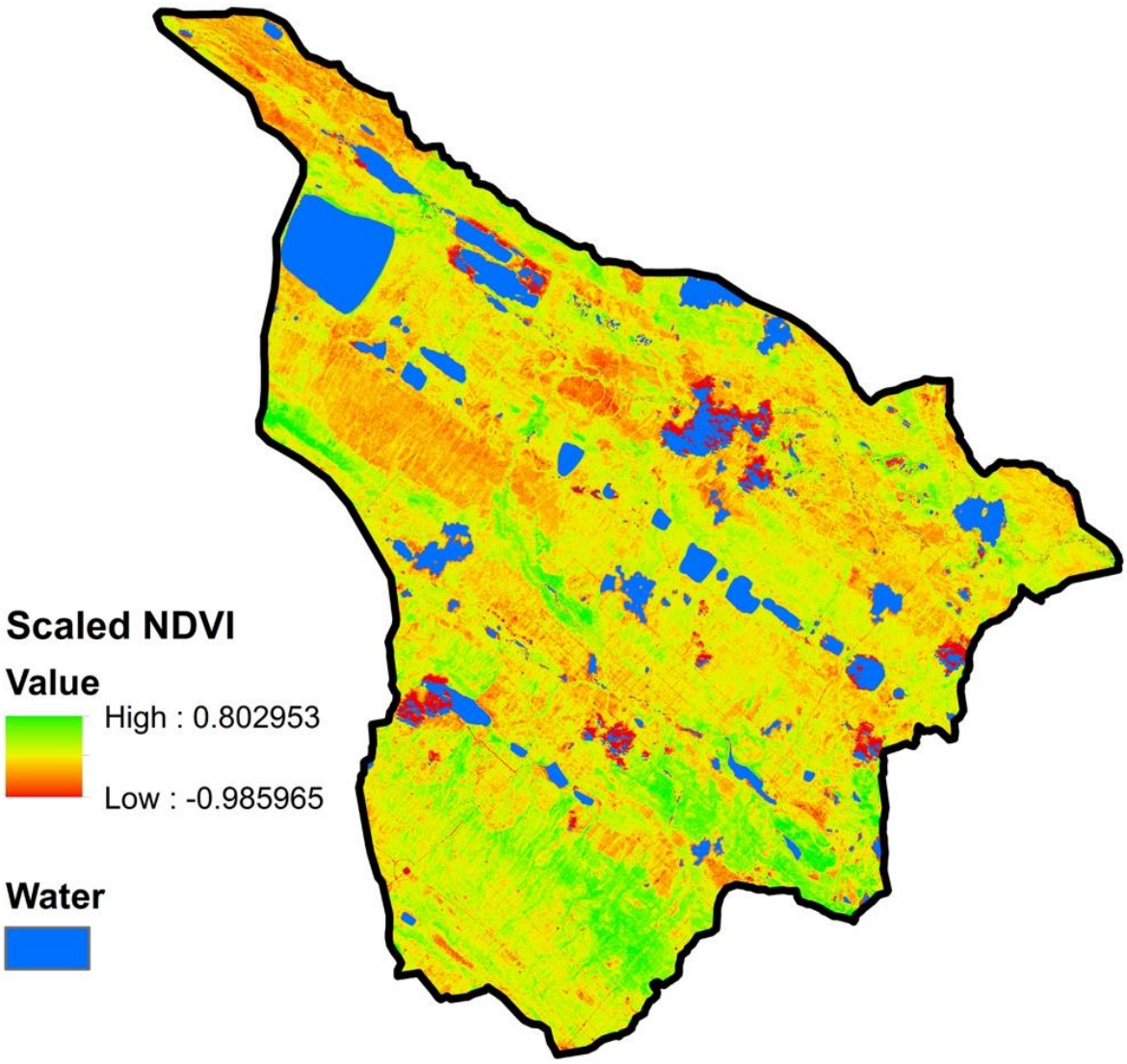

Figure 30. 2012 NDVI result histogram (top) and distribution within the study area (bottom).

The NDVI distributions exhibit a slight negative skew at this point as water bodies have not yet been removed from the analysis. Water bodies are removed before the intersection process.

After the NDVIs are generated, consecutive years are subtracted from each other to find pixels which have a decreasing NDVI. These pixels are then extracted from each set and categorized according to the degree of negative change, described in section 2.5.6. Each of the two-year sets are also intersected with each other to find regions which have been continually degrading since 2012. This result is shown in Figure 31 below and explored further in the discussion.

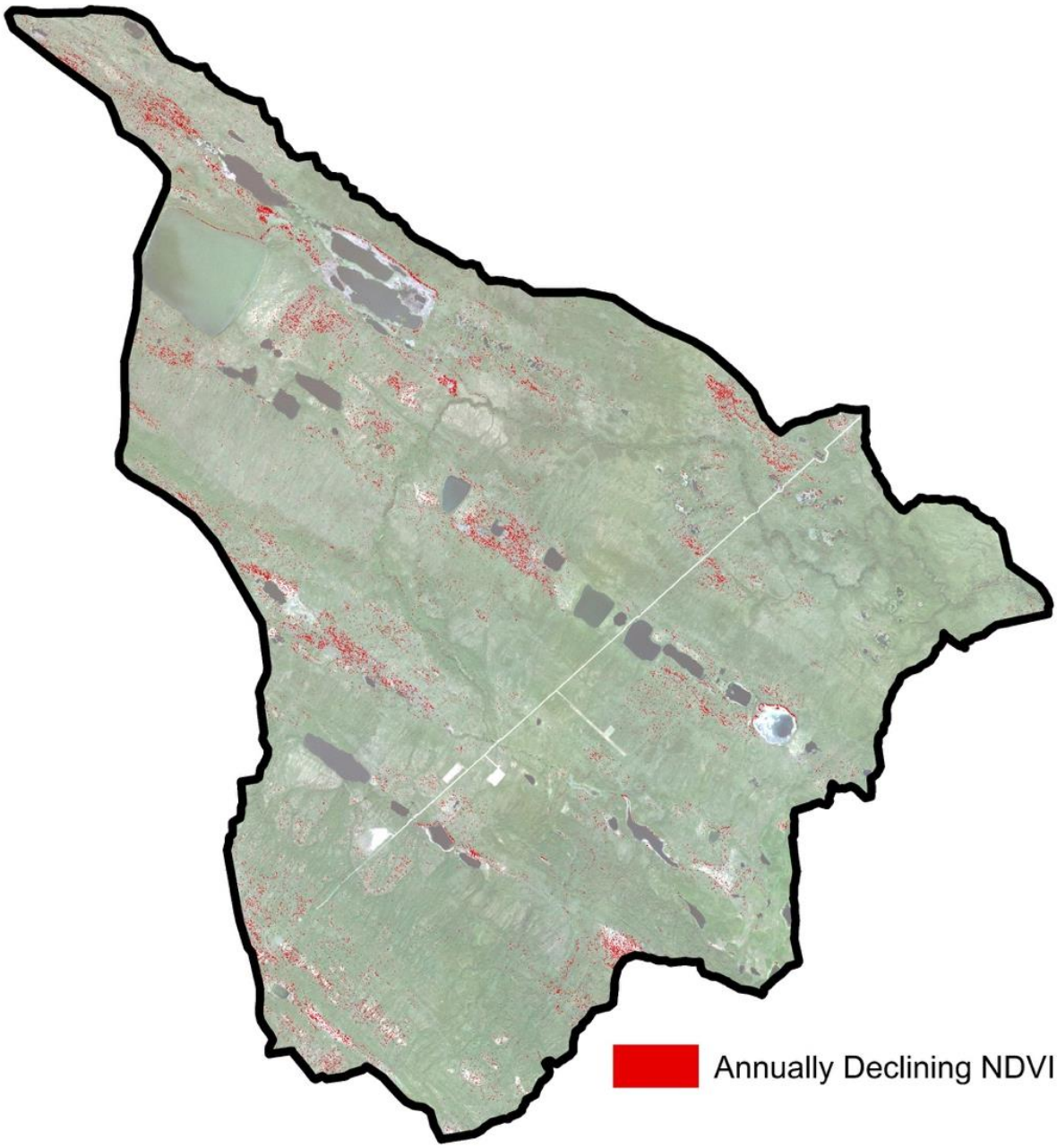

Figure 31. Result of intersect from all 4 pairs of consecutive years; regions of annually declining NDVI indices are shown in red.

2.5.7 Patterns in Vegetation Change

The RapidEye-3 data pertaining to vegetation degradation in the Bogg Creek Watershed is analyzed firstly by determining the proportion of degraded areas which occur within the following NDVI change intervals for each respective year combination (2017/2016, 2016/2014, 2014/2013, and 2013/2012). The intervals used to separate the degraded areas are as follows:

-0.001 to -0.05
-0.05 to -0.1
-0.1 to -0.15
-0.15 to -0.2
-0.2 to -0.25
-0.25 to -0.3
< -0.3

The intervals are arbitrary but are separated by equal class widths. The first interval represents the least amount of change (less degradation), and the last interval represents the greatest amount of change (the most degradation). For each year combination, the total number of pixels as well as the area represented by those pixels is tabulated. This information can be found in Appendix C, and is presented graphically in Figure 32 below.

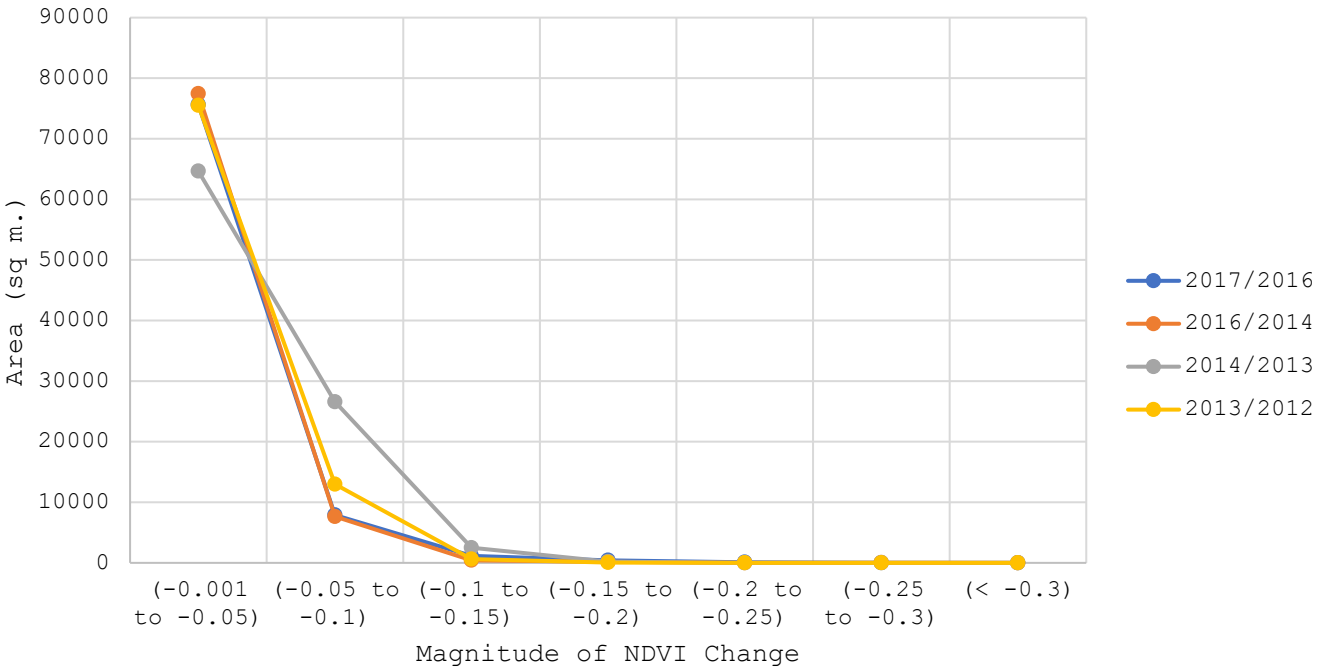

Figure 32. Amount of negative NDVI change, by area, occurring for each of the given year combinations.

The total area within the Bogg Creek Watershed that experienced continuous negative NDVI change is approximately 2 million sq. meters. This represents 1.1% of the entire watershed. When water features are omitted from the study area, degraded regions represent 1.3% of the entire watershed. Upon visual inspection, it is observed in Figure 32 that the vast majority of regions do not experience NDVI changes at the extreme end of the spectrum, but rather experience consistent small NDVI changes. This observation is confirmed by performing a Chi-Squared Goodness of Fit test on the categorical data given by Figure 32. Three separate tests are performed, comparing each two-year NDVI changes to the subsequent two-year NDVI changes. Complete Chi-squared distributions are given in Appendix C, and are summarized by Table 6 below.

For each of the three tests, the null hypothesis (H_0) states that there is no significant difference in the distributions between multiple two-year combinations. In all three cases, the test statistic (X^2) is less than the critical value (12.59). Therefore, the null hypothesis is not rejected, and there is not enough evidence to conclude that a significant difference in these distributions exists at the 0.05 level. This result suggests consistency in the magnitude of NDVI change that occurs on a seasonal basis. Upon visual inspection of Figure 32, this is also evident.

Table 6. Results of Chi-Squared test performed on the distribution of NDVI change for each year combination.

t_1	t_0	X^2	Critical value	Result
2017/2016	2016/2014	0.0196	12.59	H_0 not rejected
2016/2014	2014/2013	0.2174	12.59	H_0 not rejected
2014/2013	2013/2012	0.2185	12.59	H_0 not rejected

Next, the degraded regions (shown in Figure 31) are compared to thermistor data collected by Husky Oil to determine whether there is a spatial relationship between wells which have documented permafrost thaw and regions which have degraded vegetation. As aforementioned, for the purposes of this work, ‘negative NDVI change’ is assumed to be attributed to vegetation that is performing less photosynthesis and is therefore less healthy and less green. Negative NDVI changes could also be the result of increasing wet surface conditions, as water, similarly

to unhealthy vegetation, will absorb infrared light. Though this phenomenon would potentially make the interpretation of the NDVI difficult for most study regions, for this particular study region, it is not problematic. Since vegetation degradation is hypothesized to be attributed to permafrost thaw, and wet surface conditions are a typical side effect of this thaw, the exact cause of the NDVI change is not of importance at this point in the study. Whether it is attributed to actual vegetative loss or to surface wetness, permafrost thaw is still implicated. The goal of this work is not to examine the absolute change in vegetation cover, but rather to use it as a proxy for permafrost thaw.

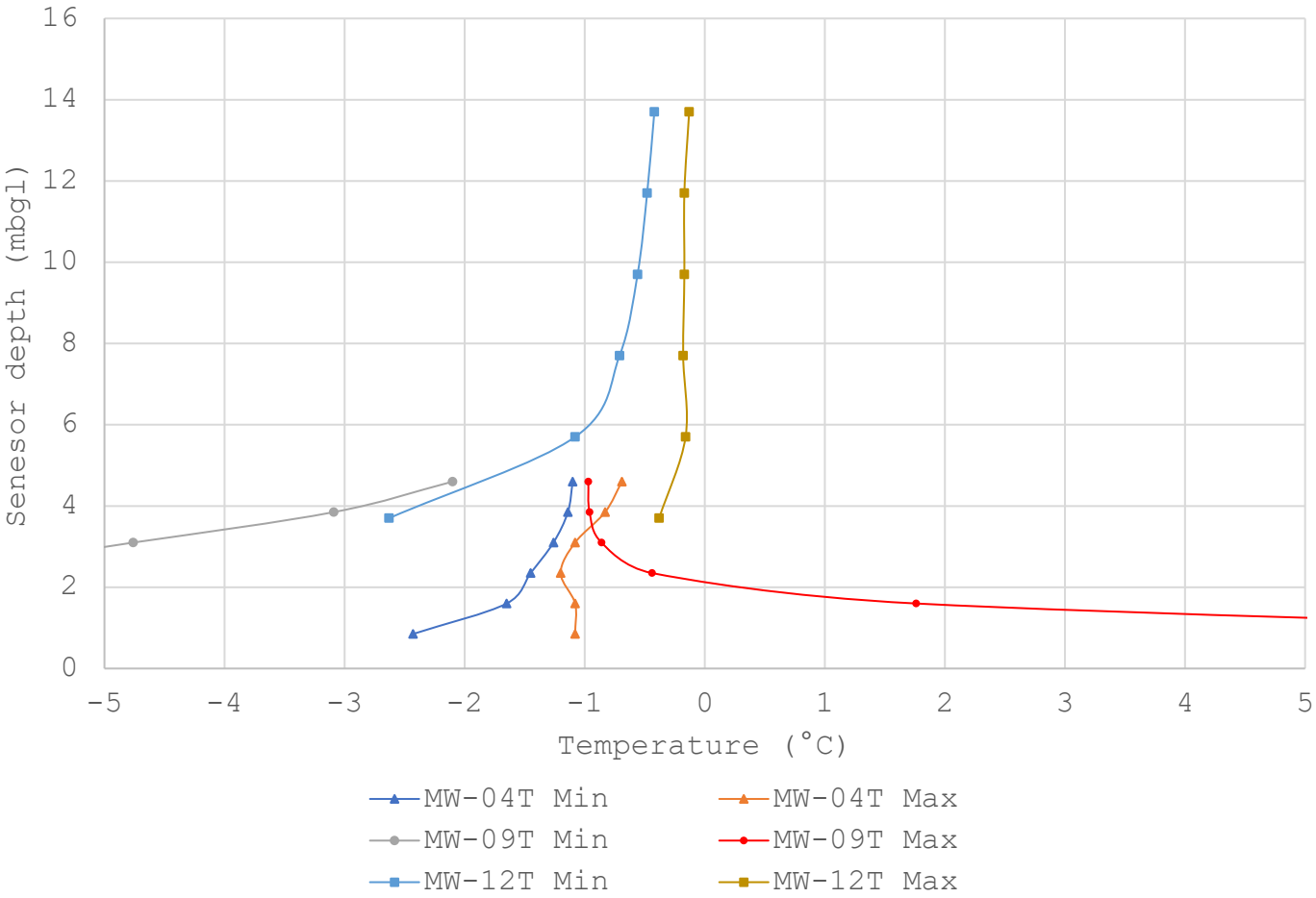

Figure 33. Thermistor data for three monitoring wells within Bogg Creek Watershed, collected and compiled by Husky Oil. Shown are the maximum and minimum temperature profiles between March of 2013 and Sept of 2016.

Figure 33 above illustrates thermistor data given by Husky Oil for three different monitoring locations within the Bogg Creek Watershed (MW-04T, MW-09T, & MW-12T). These monitoring locations are plotted on top of the vegetation degradation map in Figure 31. From early March of 2013 to late September of 2016, thermistor data was collected on a daily basis by Husky Oil. Upon visual inspection of Figure 33 and 34, it can be seen that the regions with the highest concentration of degradation pixels are also regions of greatest permafrost thaw. MW-09T displays the warmest maximum temperature during the studied period, reaching more than 5 degrees Celsius near the ground surface. MW-12T, though it does not quite cross the 0-degree line, sits only slightly below zero for all maximum sensor depths. MW-04T displays the coldest maximum ground temperatures, not exceeding -1 degree Celsius for any depth.

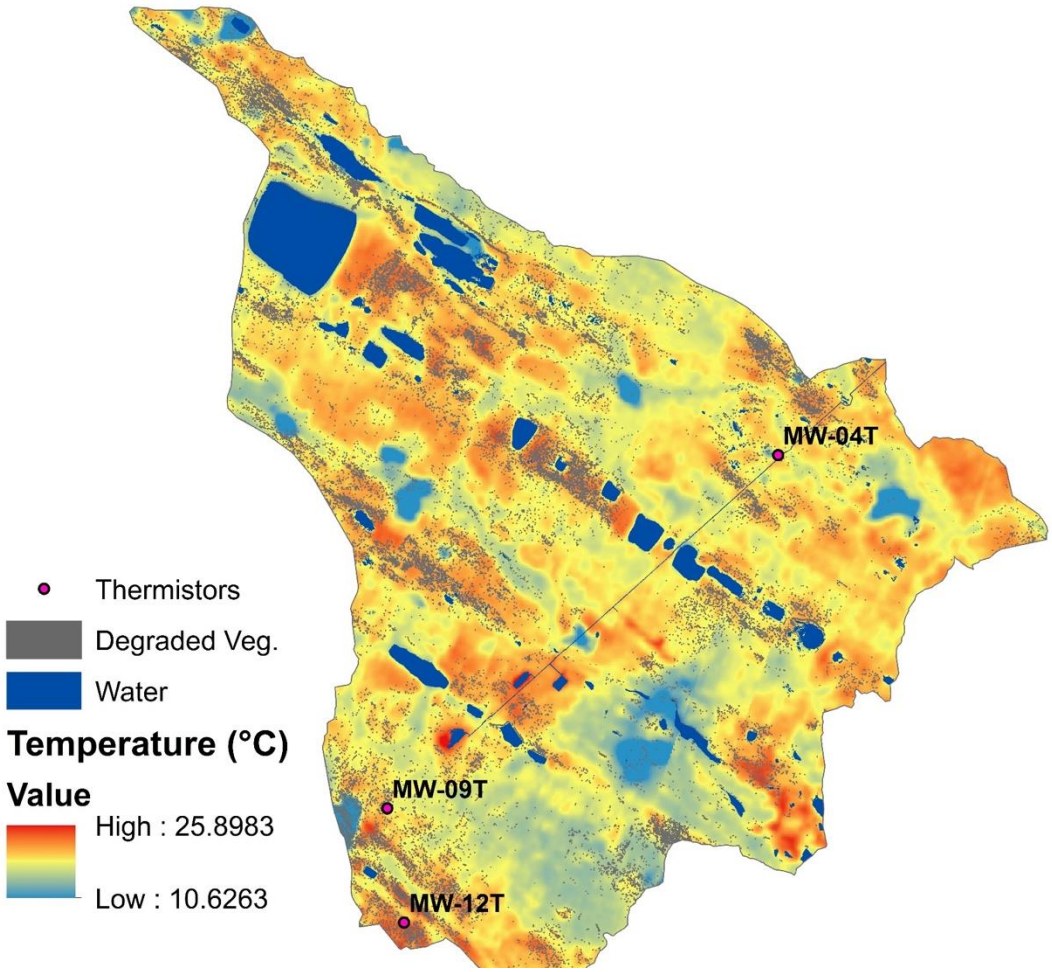

Figure 34. July 2016 Brightness Temperature derived from Landsat 8 OLI, overlain by degraded vegetation regions and thermistor locations.

The relationship between the thermistor data and the degraded vegetation is examined spatially in further detail by creating circular buffers around each monitoring station and then tabulating the number of ‘degraded pixels’ which fall within a certain distance from the monitoring station. A multi-ring buffer is created for each monitoring well using the Multiple Buffer Ring python script tool. Buffering distances are set between 50 and 500m at 50m intervals.

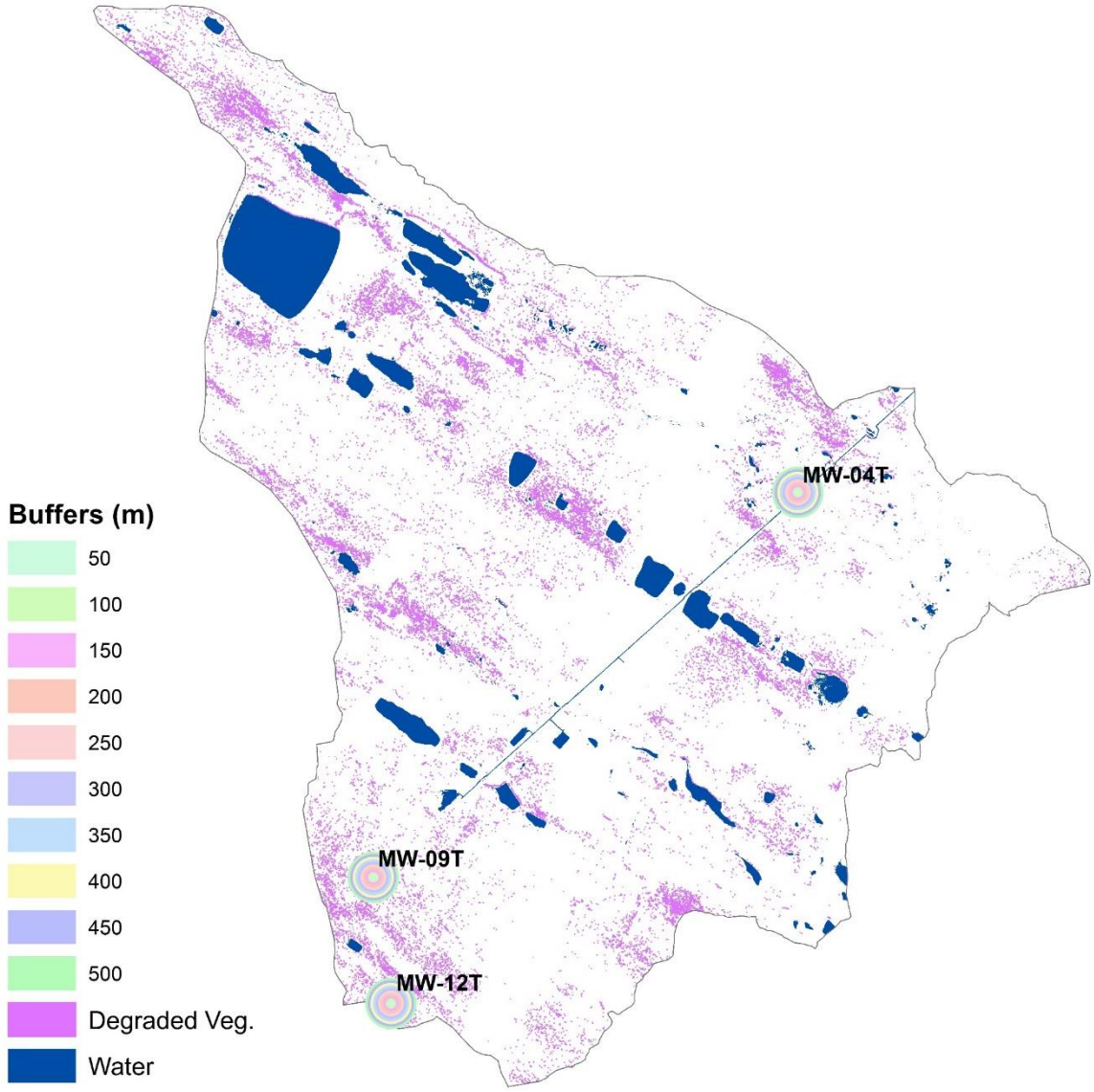

Figure 35. Buffers created to analyze the proximity of degraded NDVI pixels to monitoring stations which contain thermistors.

Of the total proportion of degraded pixels occurring within the buffers of the three thermistor monitoring stations, 0.11 falls within MW-04T, 0.37 falls within MW-09T, and 0.52 falls within MW-12T. The proportion of pixels falling within each buffer ring was not calculated, but can be examined visually in Figure 36 below.

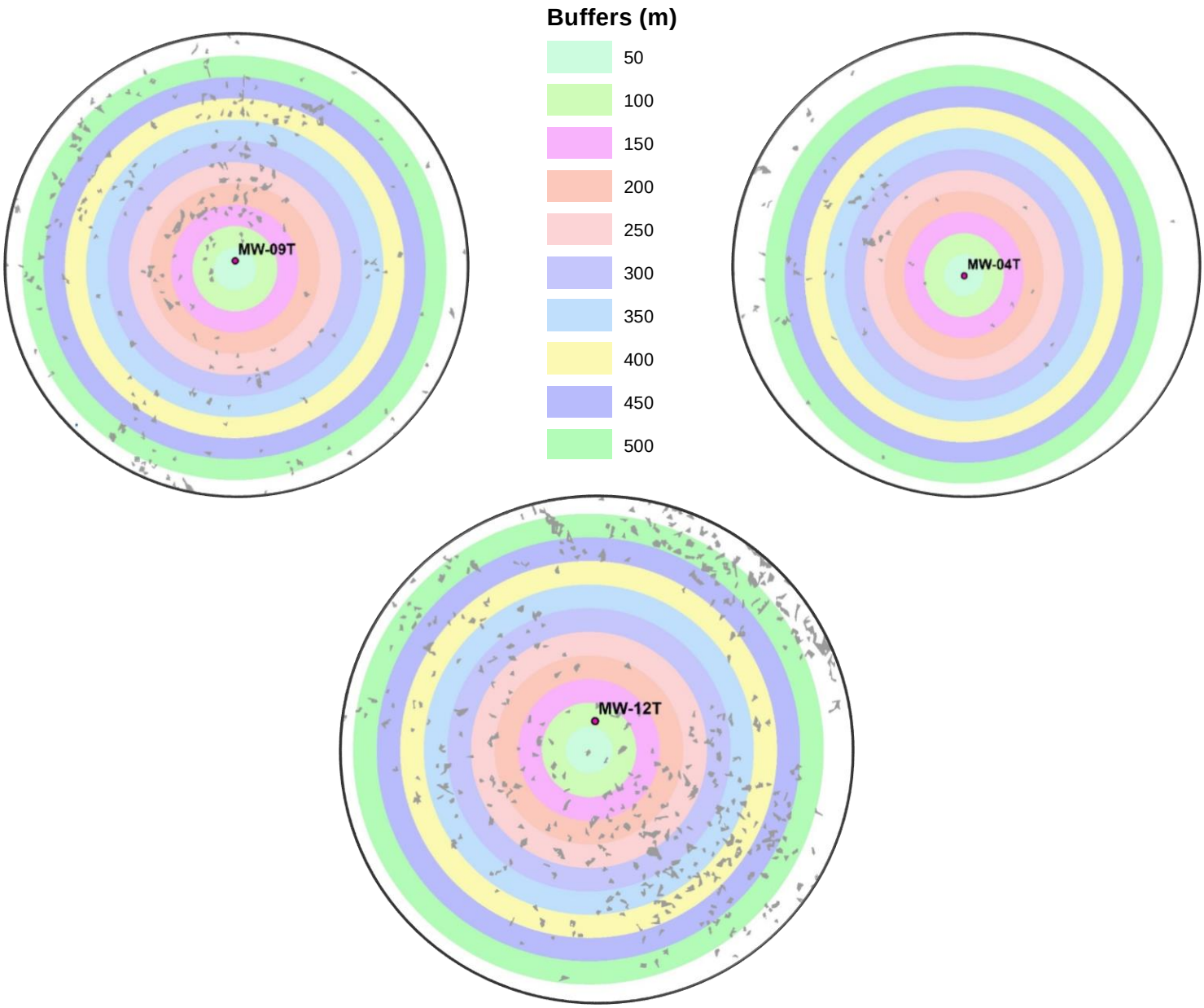

Figure 36. Buffers overlain by degraded vegetation pixels for each of the three thermistor monitoring locations in the Bogg Creek watershed.

Finally, the vegetation degradation map is compared to an at-satellite brightness temperature map generated from a Landsat-8-OLI scene collected on July 1st of 2016. This map is generated following the methodology given in 2.4. In comparing the vegetation and temperature maps, it can be determined whether or not there is a strong relationship between surface temperature and vegetation cover. If there is consistency in this relationship, it indicates that the process used to locate degraded vegetation regions is reliable. When water, clouds, and manmade features are excluded, regions of degraded vegetation should be, on average, warmer than the rest of the scene. As aforementioned, many studies have demonstrated the inverse relationship between the NDVI and the brightness temperature, such that lower NDVIs are attributed to higher brightness temperatures and vice versa. The vegetation degradation regions are overlain onto the 2016 temperature map shown in Figure 34. To quantify the association between temperature and decreasing NDVI, an overlay analysis is performed. The temperature distribution is reclassified into 5 quantiles and the area of degraded vegetation occurring within each of the quantiles is calculated. This data is displayed in Table 7. The greatest amount of degraded vegetation (by area) occurs in the highest temperature quantile, the least amount of degraded vegetation (by area) occurs in the lowest temperature quantile, and more than 60% of the total degraded area occurs in the highest two quantiles.

Table 7. Result of overlay analysis between the July 2016 brightness temperature distribution and the regions of degraded vegetation (decreasing NDVI).

Quantile (°C)	**Area intersecting with degraded vegetation (m^2)**	**Percent of total area**
10.6 – 20.4	141873	6.7
20.4 – 21.2	210671	10.0
21.2 – 21.6	338389	16.0
21.6 – 22.2	566447	26.8
22.2 – 25.9	858140	40.6

2.6 Discussion

2.6.1 Distinguishing Spring and Ground Type Icings

As aforementioned, it was anticipated that icings would be segregated into either strong warm (2, 3, 4), or strong cold anomalies (-2, -3, -4) and that this property could be used to distinguish spring from ground icings. This discernment is important when establishing field monitoring sites as different mechanisms and physical processes within these two types of icings may affect the way that contaminants are moved to the surface and the way that icings interact with the flow system. This hypothesis forms its basis from the previously reviewed literature on icing phenomena, which indicates that ground icings may exhaust their supply of groundwater at some point during the winter and that spring icings have a continuous supply through the winter, reaching peak formation in the late spring (Carey, 1973; Kane, 1981; Yoshikawa et al. 2007). Weak anomalies (1, -1) would then represent unaffected snowpack – snow that does not contain either active or inactive icings.

As the majority of icings did fall within weak warm and cold anomalies, this suggests that the presence of icings, whether discharging groundwater or not, does not strongly affect the land surface temperature in the majority of cases. The icings falling in the weak warm may be discharging enough warm groundwater to fall above the mean temperature, but not enough to appear in the strong warm. Similarly, the icings falling in the weak cold may affect the LST enough to fall below the mean, but not enough to appear in the strong cold. In theory, it is possible that the mean of the data (the 0 level Z-Score) could distinguish ground from spring icings, however, the results provide insufficient evidence to support this conclusion. If an icing were classified as spring type because it fell *just* above the mean Z-Score of 0, it may in fact be a ground icing that is still discharging warm water in the late winter or that has a low ice content. The same argument may be made for an icing classified as ground type because it fell just below the mean. Perhaps this is in fact a spring type icing which is discharging a small amount of groundwater on that particular day. These examples are to say that because the weak anomalies represent values closest to the mean, their contrast is not sufficient to discriminate icing types. Additionally, if the icings are distinguished from one another using the entire dataset, there is likely room for a large degree of error in classifying those icings which lie in the weak anomalies. So, the icings which do fall into strong warm and cold anomalies may be more

definitively classed as either spring or ground type based on current definitions of their physical occurrence, but because the majority do not fall into these strong anomalies, it is concluded that thermal anomalies may not be an ideal variable for discriminating icing type at this resolution. The spatial resolution of the Landsat thermal band is only 120m (re-sampled to 30m) and therefore may be too coarse to detect temperature changes resulting from groundwater discharge. This is especially true when the discharge locations are small and discrete, as they seem to be in this region. Fine resolution thermal cameras would likely be more successful at discriminating spring and ground type icings in this region. Mundy et al. (2017) utilize thermal cameras to identify groundwater seeps in a limestone quarry in Quebec, Canada, and find that the cameras are able to identify small seeps in both the summer and the winter. Use of fine resolution cameras for identifying GW discharge should also be explored in the CMV in both the winter and summer. This would offer insight not only into the location of discharge zones but would provide information regarding whether the discharge zones are temporary, intermittent, or permanent features. It should also be noted that there are other factors besides discharging groundwater that may play a role in determining land surface temperature. These include snow pack density and differential thermal insulation (Diaz et al. 2015). Several measures were taken to try and account for variation in the expression of the anomalies. These included: Conversion to land surface temperature rather than brightness temperature, removal of water bodies from the distribution, selection of images with a similar snow depth, selection of cloud-free images, selection of images taken at the same time of day, and temperature standardization.

2.6.2 Recurring Icings and Implications

As the initial results described above do not provide promising evidence for classifying icings based on coarse resolution thermal anomalies, the 3-year recurring icings were examined in more detail. The fact that the minority of icings observed in the study region (12.5% by area) recur in each observed year suggests that the majority of icings are intermittent or temporary. Though it is possible for ground type icings to recur in the same location year to year, it is expected that these recurring icings are more likely spring type as there is greater evidence to suggest that springs yield recurring icings (Yoshikawa, et al. 2007). The hypothesis described in the previous section is re-tested but using only the 3-year recurring icings and no relationship was found

between either extent or count with the strong anomalies. This result is not surprising given that the majority of icings from all years coincide with weak anomalies. As the results indicated in Table 4 are so variable, no definitive conclusions are drawn regarding the type of icings that 3-year recurrences are likely to be. This does not mean that the 3-year recurring icings aren't of spring type, but it does suggest a large degree of variability in the hydrogeological regime, and that spring and ground type icings may not simply be distinguished based on the amount of water they are discharging in the late winter. Nonetheless, these 3-year recurring icings do provide promising locations for field monitoring, where further in-situ work may be able to classify their type more definitively. It has been demonstrated by field observations that ground icings contain more organic material (appearing brown in color) than due spring icings (Carey, 1973), and also that carbonate precipitates are found in spring-derived icings (Hall, 1980). These variables warrant further investigation in the CMV and in Bogg Creek. In this work, the observations that a) 87.5% of the icings by area do not recur in all years, and b) upon visual inspection, the distribution of anomalies is not consistent, further supports the conclusion that these icings are intermittent and occur in different places on an annual basis. It is interesting to note that in 2016, warm icings cover far more area than they do in 2009 or 2004 (74.9%, 5.9%, 10.7% for years 2016, 2009, and 2004 respectively). This may indicate that more groundwater springs are becoming active in the spring months as permafrost continues to thaw. Several studies in Northern Canada and Alaska observe an increase in the amount of groundwater discharge as permafrost thaws and the active layer thickens. Walvoord et al. (2012) calibrate a model using data from the Yukon Flats Basin and find that projected future permafrost thaw results in increased river discharge from GW contributions, increased overall GW flux, and increased lateral reach of groundwater discharge in low-lying areas. Evans and Ge (2017), also using numerical modelling techniques, projected the amount of groundwater discharge that will occur on hillslopes following a 100-year warming period that induces permafrost thaw. They also observe significant increase in GW discharge following climate warming. These findings lend strong evidence to suggest that increasing proportions of warm icings in the CMV during late winter/early spring (when the surrounding landscape is still colder than discharging groundwater) could be, at the very least, partially resultant of permafrost thawing.

It is also observed that the distributions of icings (by size and count) within thermal anomalies between 2004-2009 and 2009-2016 are significantly different such that the magnitude

of change between 2009 and 2016 is far greater than between 2004 and 2009. Owing to the fact that there is a large amount of data missing within these intervals, it is difficult to make a definite conclusion regarding why the magnitude of change is so great between 2009 and 2016. It is expected that recent changes in climate and the state of permafrost play a role.

2.6.3 Localized Icings in the Bogg Creek Watershed

The occurrence of icings within Bogg Creek is minimal when compared to the occurrence of icings throughout the entire CMV. As aforementioned, there was one major icing hotspot (complex) identified in northwestern region of the watershed. The primary surficial texture class in this region is 'fen', therefore it follows that the water table in this region is likely close to the surface and has strong potential for GW-surface interactions. Based on the recurrence of icings in this region, they are more likely of spring (permanent type). Whether they are sourced from deep or shallow springs cannot be determined at this point, but given that they occur in a fen environment, it is most likely that if shallow spring icings exist, they would be in this region. It is recommended that geochemical and isotopic methods should be used in situ to identify the source water feeding these icings.

In 2004 and 2009, a substantially larger icing exists in on the eastern side of the two lakes which is not present in 2016 and 2017. This may be a function of less water availability due to permafrost thaw. As described earlier, permafrost thaw in this region generally results in a two-fold landscape change. Firstly, a region of surface permafrost thaws, raising the water table and causing surface inundation. This water is trapped by the still existing permafrost beneath it and cannot drain. Subsequently, permafrost thaw progresses to a greater depth until the initially trapped water above it has a drainage route. At this point, the water table lowers to a point which is below its initial position. So, if icings in this complex are sourced from shallow springs, it follows that late stage permafrost thaw may restrict the amount of water that is available to them. This is a possible cause of the decreased extent of the icing complex in 2016 and 2017. Precipitation patterns may also play a role in the occurrence of this icing complex. Total precipitation from January to April was 34.7, 53.4, 119.4, and 81.6 mm for years 2004, 2009, 2016, and 2017 respectively at Norman Wells Climate Station A (Environment Canada, 2018). This precipitation falls almost entirely as snow. When the icings are detected, the majority of

snow has already melted, therefore, in years when Jan-April precipitation was greater (2016, 2017), it is possible that spring snow melt may cause icings to disappear more quickly than in years where Jan-April precipitation is less (2004, 2009). Conversely, it is possible that greater snow accumulation (which is positively correlated to the Jan-April precipitation) could serve to better insulate and preserve icings. The association between icing occurrence and precipitation may be significant, but requires more in situ observation.

2.6.4 Characteristics of the Hydrogeologic System

Though the distribution of icings within their respective anomalies is similar, the overall distribution of icings is highly inconsistent. However, this inconsistency does not appear to affect the overall areal coverage of icings from year to year. The consistency in the total areal coverage of icings suggests that the water available from the subsurface during winter is also consistent. Yoshikawa et al. (2007) conclude that icings monitored in the Brooks Range of Alaska are not nearly as sensitive to climate change as they are to source groundwater properties. It is suspected that this is also the case for icings in the CMV. As there have been numerous studies in the last few decades detailing dramatic climate changes in Northern latitudes, yet icing coverage remains consistent in the CMV, this lends evidence to the idea that climatic changes are not adversely affecting the volume of groundwater discharge during the winter. This information in itself is invaluable, as it provides an indication of the amount of groundwater that discharges to the surface during the winter. This metric can be used in part to characterize the overall hydrologic system of the area, and to determine what proportion of water available in the system is derived from a subsurface source. Areal coverage on its own is not particularly useful for this purpose, therefore, an empirical equation first proposed by Sokolov in 1973 is suggested to compute the volume of icings:

$$V = b * F^n \quad (12)$$

where V = volume of icings,

b and n = aufeis growth coefficients, and

F = the area of icing coverage, derived from satellite imagery

Empirical coefficients to be used in this equation were determined for an aufeis field in the Brooks Range of Alaska in 1981 by Hall and Roswell:

$$V = 0.96 * F^{1.09} \quad (13)$$

These coefficients are used here to establish an initial estimate of the volume represented by icings in the Central Mackenzie Valley region. This information is not used for any further analysis in this study, but simply to provide a baseline for the volume of discharging water that may be used to better understand the hydrogeologic system, and to establish initial or boundary conditions used in future numerical models. Using this equation, total volumes of icings are found to be 161, 159, and 149 million cubic meters for years 2016, 2009, and 2004 respectively. In situ studies would be required to refine these coefficients for more precise use in the CMV, and/or to assess the applicability of the Brooks Range coefficients for use in this study area. Several factors may influence icing/aufeis growth coefficients. These include: soil type and structure, amount of source water, elevation, and icing type.

2.6.5 Relationship between Surficial Geology and Icings

As shown in numerous studies, and in particular for regions where icings develop (Romanovskii et al., 1996), groundwater discharges at the surface where materials are most permeable. Therefore, it was hypothesized that icings would also occur in areas of higher permeability geology as they are sourced from groundwater. This hypothesis is well supported by the results indicated in Figure 26. Sand, having one of the highest hydraulic conductivities of all subsurface materials, is very proficient at transporting subsurface water and yielded the second highest amount of icings (by area) for all years. Bedrock outcrops yielded the highest amount of icings for all years. Bedrock in the region is primarily late Devonian to early Cretaceous shale and sandstone (Rudolph, et al. 2016). Some of the sandstone formations in the area have been confirmed to contain productive aquifers, and therefore may dispel water at the surface. Bedrock shale, whether or not it contains water, is a highly impermeable lithology. This implies that fractures within shale formations could provide more conductive transportation routes for subsurface water. Bedrock outcrops and sand are also representative of the largest icings in the

study area, for all years. Therefore, more permeable materials may provide a more consistent flow of subsurface water, allowing icings to grow larger than they would in less permeable materials. Several studies examine the discharging groundwater resultant from bedrock fractures. One in particular, Jardine et al. (1999), use a tracer experiment to determine the contribution of a fractured shale matrix to the overall movement of contaminated groundwater in a region. Relative to the total amount of contaminant transport between two points, the contribution by the shale matrix is large. These findings indicate that fractured shale (and bedrock in general) not only holds potential to influence the dynamics of icing growth, but also the movement of contaminants through the subsurface. Transport of fluids through shale is of particular concern for this region as oil exploration is targeted largely at the reserves stored in shale units.

The exposed bedrock in the area requires further investigation to determine the extent and nature of possible fractures that are dispelling water. The Geological Survey of Canada has mapped, in detail, a system of thrust faults and folds in the region that may be related to the discharge of water. However, given that icings can be as small as 25 sq. meters, small localized fractures are expected to play an important role. It is also possible that the presence of bedrock at the surface may be a good indicator of whether an icing is of spring or ground type. It seems more plausible that icings present over low permeability bedrock would be sourced from a spring since they would need to be transported through a fracture. Additionally, it is found that the correlation between the three-year recurring icings and the presence of bedrock is strong. This provides further evidence to suggest that these recurring icings are primarily of spring type. Therefore, it is proposed that of the three-year recurring icings, field monitoring sites should contain a good mix of icings that occur over exposed bedrock and icings that occur over sand.

2.6.6 Vegetation Degradation and Climate

The results of the vegetation analyses strongly support the hypothesis that permafrost thaw is correlated with both decreased vegetation health and with increased surface wetness. As a significant difference in the vegetation degradation between consecutive two-year combinations could not be detected, it is concluded that NDVI is declining at a relatively consistent rate. That is to say that fast, extreme changes in vegetation patterns have not yet been observed, but rather

that slow and gradual changes are occurring. This is also supported by the fact that most of the degraded regions fall within the less extreme side of the change spectrum indicated in Figure 32. Regions experiencing very extreme changes are negligible and also are not intersecting over consecutive years. These extreme changes are therefore more likely to be attributed to a variable besides permafrost thaw, such as infestation or age. The changes occurring on the non-extreme end of the spectrum suggest a parallel between the rate of permafrost thaw and rate of forest degradation. As permafrost in this region is ice rich, it requires significantly more heat to thaw completely than does ice poor permafrost (Xiaoliang, et al. 2012). This often prevents dramatic changes from occurring over short periods of time. Whether the declining NDVI reflects actual vegetative decline or increased surface wetness does not influence the results of this analysis. Both factors imply a loss of permafrost. The strong association of the surface temperature and the declining NDVI regions supports this conclusion.

As an initial validation of the NDVI results, degraded regions were compared to thermistor data collected by Husky Energy Ltd. Using a buffering technique, it was determined that the greatest proportion of degraded pixels occur surrounding MW-09T and MW-12T. Much less degradation occurred surrounding MW-04T. This is expected, given that the warmest ground temperatures experienced at MW-04T are still well below zero. The area surrounding MW-04T has likely not undergone extensive permafrost thaw yet, and consequently still maintains healthy vegetation. The other two monitoring stations, by contrast, have experienced warmer maximum ground temperatures and are more likely to be in regions which have experienced significant permafrost loss. It is noted that the areas in which the monitoring stations are located have been cleared of vegetation to allow easy access. Lack of vegetation results in greater snowfall which leads to greater insulation of the subsurface (Atchley, et al. 2016). This may cause the ground in the immediate area of the monitoring stations to be warmer than the surrounding vegetated area due to the entrapment of latent heat. However, because all of the monitoring stations would experience this phenomenon in the same way, the results of the buffer analysis are unchanged. The absolute temperature in the thermistor profiles may be artificially warm, but as they are compared relative to one another, this is not a limitation in the interpretation of the NDVI.

With respect to the establishment of field monitoring locations, any of the degraded regions represent places which could be examined in greater detail to establish information about rates of permafrost thaw, contribution to the flow system, etc. There are a few regions near the main icing complex which have very dense degradation pixels. These places are recommended as the priority field monitoring locations as they are nearby the icings and would minimize the need to travel to further locations within the study area.

2.6.7 Limitations and Recommendations

Though this work has been able to effectively accomplish the outlined objectives, there are a few limitations that should be acknowledged. Firstly, icings within the study region may not have been detected by the algorithm for a few reasons:

- They were narrower than the minimum pixel resolution of 5m for RapidEye-3 or 30m for Landsat 4-5 TM/8 OLI.
- They were located on a slope or in a gully at the bottom of a slope that is shaded by topography of higher elevation
- They were covered in organic matter which decreased their albedo sufficiently and prevented them from exhibiting distinctive spectral signatures
- They had melted in the early spring

As previously discussed, the thermal analysis was severely limited by its coarse resolution of 120m. It would likely have been more effective in regions where icings and groundwater discharge zones are more extensive. However, because this region exhibits many small icings, the thermal imagery was not of great use. Additionally, the usefulness of the higher resolution RapidEye-3 data compared to the medium resolution Landsat data could not be quantified due to challenges in acquiring images from the same time periods for both of these datasets. The only RapidEye-3 image that could be used was from the spring of 2017; A parallel Landsat image could not be obtained at this time due to persistent cloud cover. Because many of the icings detected in the Bogg Creek Watershed using the RapidEye-3 data were smaller than the Landsat pixel size of 900 square meters, it is expected that the analyses performed on the Landsat data may have neglected to detect icings smaller than 900 square meters. Future works may consider using even higher resolution optical imagery to track icings over a longer temporal period.

Refining the temporal scale would provide greater evidence to suggest which icings represent permanent groundwater-surface water interactions. Use of SAR imagery (such as Radarsat) may also be of good use in this study region as it is not impeded by cloud cover. As this region exhibits very persistent cloud cover, use of radar backscatter and surface roughness properties are recommended as a method that may be tested in the future.

In order to verify and further explore the results of the icings analysis, the identified locations of recurrent icings should be examined in situ. As aforementioned, the source of water feeding icings may be detected in several ways including the degree of organic matter present on top of the icing, the temperature of the water feeding the icing, and the geochemical makeup of the icing. Isotopic signatures are recommended as a method of determining whether an icing may be sourced from deep groundwater or from shallow active layer water. An analysis of this kind would provide concrete evidence as to whether an icing is of spring or ground type, information which is invaluable in characterizing the overall flow system. Additionally, quantifying the volume of water occupying icings will be important in order to determine the magnitude of the spring which may be feeding it. It is recommended that any data collected which measures the approximate volume of water in an icing be used to refine the aufeis growth coefficient described in the discussion.

The vegetation analysis was limited by the fact that it does not differentiate between lack of photosynthesis and the presence of surface water. Though the results given by the comparison to thermal imagery and monitoring thermistors indicate that this limitation did not have a significant impact on the results, it is possible that there are some small localized regions which become wet in the summer and do not experience vegetative decline. However, these areas are likely negligible as the majority of forest cover in the study area is very intolerant to saturated conditions. Following this, the fact that vegetation was not first classified by type could be considered a limitation in the interpretation of the NDVI results. Nonetheless, the results provide a good initial idea of where the effects of permafrost loss are being experienced. Future works should verify the results of the vegetation analyses by assessing soil saturation and permafrost loss (active layer thickening) in situ. Non-remote geophysical methods such as GPR (ground-penetrating radar) are expected to be effective for this purpose.

2.7 Conclusions

2.7.1 Icing Occurrence

The locations, sizes, and recurrence of icings within the Central Mackenzie Valley and the Bogg Creek Watershed were determined for years 2004, 2009, 2016, and 2017 using a combination of medium resolution Landsat 4-5 TM/8 OLI and RapidEye-3 imagery. Additionally, thermal anomalies were calculated using the Landsat thermal band for years 2004, 2009, and 2016. Following these results, several important conclusions regarding icing occurrence were made:

I. The amount of winter groundwater discharging in this region is stable from year to year, even though the spatial distribution of icings is not.
II. Ground and spring icings may not function in the same way across all regions; that is to say that ground icings may still discharge water late in the winter, and spring icings may undergo periods of little or no discharge.
III. Due to variability in the distribution of recurring icings within thermal anomalies, and the large overall proportion of icings in weak anomalies for all years, coarse resolution thermal data should not be used to definitively distinguish ground and spring type icings. It should be used only to make suggestions as to the mechanisms governing their formation.
IV. Icings are well correlated with the occurrence of sand (a highly permeable material), and bedrock (a material that is suspected to contain fractures). The presence or absence of bedrock at the surface may be used to establish icing type in situ.
V. Priority icing/groundwater discharge monitoring locations were established for the Bogg Creek watershed in a region which is classified as a fen. The icings in this region are annually recurrent and are likely sourced from shallow springs.

2.7.2 Patterns in Vegetation Health

RapidEye-3 data was obtained for years 2011-2017 in the late summer (peak vegetation) in order to pinpoint regions of annually decreasing NDVI. Approximately 2 square km of vegetated area was identified as having a degrading NDVI since 2011. This represents 1.1% of the entire watershed. Following the results of Quinton et al. (2011) and Baltzer et al. (2014), these areas are hypothesized to reflect regions which are beginning to see permafrost degradation and associated surface wetness increase. They represent locations which warrant further in situ consideration to

determine the impact of permafrost thaw on both the flow system and the ecosystem. Though 2 sq. km may seem an insignificant amount of vegetation to be concerned with, it is anticipated that the patterns in vegetation will continue to degrade as permafrost thaws and eventually see the conversion to more water tolerant landcover types such as bogs and fens. This holds important implications for the dynamics of the flow system and for functions within this fragile Northern ecosystem.

References

Abdalla, B. A., Fan, C., Mckinnon, C., Kenny, W. G., & Gaffard, V. (2015). Numerical Evaluation of Cyclic Frost Heave Growth in Arctic Pipelines and Introduction to Frost Heave.

Abdul Aziz, O. I., & Burn, D. H. (2006). Trends and variability in the hydrological regime of the Mackenzie River Basin. *Journal of Hydrology*, *319*(1–4), 282–294. https://doi.org/10.1016/j.jhydrol.2005.06.039

AMEC. (2013). *Central Mackenzie Valley Subsurface Groundwater Baseline Study*. *Indigenous and Northern Affairs Canada and the North, Northern Petroleum Resources*. Retrieved from https://www.aadnc-aandc.gc.ca/eng/1100100036430/1100100036431

Arenson, L. U., Azmatch, T. F., & Sego, D. C. (2008). A new hypothesis on ice lens formation in frost-susceptible soils. *Ninth International Conference on Permafrost*, (June), 59–64.

Atchley, A. L., Coon, E. T., Painter, S. L., Harp, D. R., & Wilson, C. J. (2016). Influences and interactions of inundation, peat, and snow on active layer thickness. *Geophysical Research Letters*, *43*(10), 5116–5123. https://doi.org/10.1002/2016GL068550

Avdan, U., & Jovanovska, G. (2016). Algorithm for automated mapping of land surface temperature using LANDSAT 8 satellite data. *Journal of Sensors*, *2016*, 1–8. https://doi.org/10.1155/2016/1480307

Azmatch, T. F., Sego, D. C., Arenson, L. U., & Biggar, K. W. (2012). New ice lens initiation condition for frost heave in fine-grained soils. *Cold Regions Science and Technology*, *82*, 8–13. https://doi.org/10.1016/j.coldregions.2012.05.003

Baltzer, J. L., Veness, T., Chasmer, L. E., Sniderhan, A. E., & Quinton, W. L. (2014). Forests on thawing permafrost: Fragmentation, edge effects, and net forest loss. *Global Change Biology*, *20*(3), 824–834. https://doi.org/10.1111/gcb.12349

Barron, O., & Niel, T. G. Van. (2009). Application of thermal remote sensing to delineate groundwater discharge zones. *International Journal of Water*, *5*(2), 109. https://doi.org/10.1504/IJW.2009.028721

Becker, M. W. (2006). Potential for satellite remote sensing of ground water. *Ground Water*, *44*(2), 306–318. https://doi.org/10.1111/j.1745-6584.2005.00123.x

Cao, Y. G., & Liu, C. (2006). Normalized difference snow index simulation for snow-cover mapping in forest by GeoSail model. *Chinese Geographical Science*, *16*(2), 171–175. https://doi.org/10.1007/s11769-006-0013-6

Carey, K. L. (1973). Icings Developed from Surface and Ground Water. *Cold Regions Science and Engineering*, (III-D3).

Carlson, T. N., & Ripley, D. A. (1997). On the Relation between NDVI, Fractional Vegetation Cover, and Leaf Area Index. *Remote Sensing of Environment*, (62), 241–252.

Chander, G., Markham, B. L., & Helder, D. L. (2009). Summary of current radiometric calibration coefficients for Landsat MSS, TM, ETM+, and EO-1 ALI sensors. *Remote Sensing of Environment*, *113*(5), 893–903. https://doi.org/10.1016/j.rse.2009.01.007

Connon, R. F., Quinton, W. L., Craig, J. R., & Hayashi, M. (2014). Changing hydrologic connectivity due to permafrost thaw in the lower Liard River valley, NWT, Canada. *Hydrological Processes*, *28*(14), 4163–4178. https://doi.org/10.1002/hyp.10206

Cuenca, Juan, & Sobrino, J. A. (2004). Experimental measurements for studying angular and spectral variation of thermal infrared emissivity. *Applied Optics*, *43*(23), 4598. https://doi.org/10.1364/AO.43.004598

Dyke, L. D. (2001). Shoreline permafrost along the Mackenzie River. *Bulletin of the Geological Survey of Canada*, (547), 143–151.

Evans, S. G., & Ge, S. (2017). Contrasting hydrogeologic responses to warming in permafrost and seasonally frozen ground hillslopes. *Geophysical Research Letters*, *44*(4), 1803–1813. https://doi.org/10.1002/2016GL072009

Fraser, R. H., Abuelgasim, A., & Latifovic, R. (2005). A method for detecting large-scale forest cover change using coarse spatial resolution imagery. *Remote Sensing of Environment*, *95*(4), 414–427. https://doi.org/10.1016/j.rse.2004.12.014

Fraser, R. H., Olthof, I., Carrière, M., Deschamps, A., & Pouliot, D. (2011). Detecting long-term changes to vegetation in northern Canada using the Landsat satellite image archive. *Environmental Research Letters*, *6*(4). https://doi.org/10.1088/1748-9326/6/4/045502

Fraser, R., McLennan, D., Ponomarenko, S., & Olthof, I. (2012). Image-based predictive ecosystem mapping in Canadian arctic parks. *International Journal of Applied Earth Observation and Geoinformation*, *14*(1), 129–138. https://doi.org/10.1016/j.jag.2011.08.013

Fu, Z., Yu, B., Zhao, Y., & Kawaguchi, Y. (2014). Numerical Simulation of Frost Heave in Soils Around the Buried Oil Pipeline in Island Talik Permafrost Region. *Advances in Mechanical Engineering*.

Girardin, M. P., Bouriaud, O., Hogg, E. H., Kurz, W., Zimmermann, N. E., Metsaranta, J. M., … Bhatti, J. (2016). No growth stimulation of Canada's boreal forest under half-century of combined warming and CO 2 fertilization. *Proceedings of the National Academy of Sciences*, *113*(52), E8406–E8414. https://doi.org/10.1073/pnas.1610156113

Golder Assosiates. (2015). *Central Mackenzie Surface Water and Groundwater Baseline Assessment*.

Hall, D. K. (1980). Mineral precipitation in North Slope river icings. *Arctic*, *33*(2), 343–348.

Hall, D. K., Riggs, G. A., & Salomonson, V. V. (1995). Developemnt of Methods for Mapping Global Snow Cover Using Moderate Reolution Imaging Spectroradiometer Data. *Remote Sensing of Environment*, (54), 127–140.

Hawlader, B. C., Morgan, V., & Clark, J. I. (2006). Modelling of pipeline under differential frost heave considering post-peak reduction of uplift resistance in frozen soil. *Canadian Geotechnical Journal*, (43), 282–293.

Jardine, P. M., Sanford, W. E., Gwo, J. P., Reedy, O. C., Hicks, D. S., Riggs, J. S., & Bailey, W. B. (1999). Quantifying diffusive mass transfer in fractured shale bedrock. *Water Resources Research*, *35*(7), 2015–2030. https://doi.org/10.1029/1999WR900043

Julien, Y., Sobrino, J. A., Mattar, C., Ruescas, A. B., Jiménez-Muñoz, J. C., Sòria, G., … Cuenca, J. (2011). Temporal analysis of normalized difference vegetation index (NDVI) and land surface temperature (LST) parameters to detect changes in the Iberian land cover between 1981 and 2001. *International Journal of Remote Sensing*, *32*(7), 2057–2068. https://doi.org/10.1080/01431161003762363

Kane, D. L. (1981). Physical mechanics of aufeis growth. *Canadian Journal of Civil Engineering*, *8*(2), 186–195. https://doi.org/10.1139/l81-026

Kokelj, S. A. (2001). Hydrologic Overview of the Gwich ' in and Sahtu Settlement Areas. *Water Resources*, (December).

Kot, V. A. (2017). Solution of the Classical Stefan Problem: Neumann Condition. *Journal of Engineering Physics and Thermophysics*, *90*(4), 889–917. https://doi.org/10.1007/s10891-017-1638-2

Kurylyk, B. L., Hayashi, M., Quinton, W. L., McKenzie, J. M., & Voss, C. I. (2016). Influence of vertical and lateral heat transfer on permafrost thaw, peatland landscape transition, and groundwater flow. *Water Resources Research*, (52), 3787–3814. https://doi.org/10.1002/2014WR016618.Received

Lewis, K. C., Zyvoloski, G. A., Travis, B., Wilson, C., & Rowland, J. (2012). Drainage subsidence associated with Arctic permafrost degradation. *Journal of Geophysical Research: Earth Surface*, *117*(4), 1–18. https://doi.org/10.1029/2011JF002284

Li, S., Benson, C., Shapiro, L., & Dean, K. (1997). Aufeis in the Ivishak River, Alaska, mapped from satellite radar interferometry. *Remote Sensing of Environment*, *60*(2), 131–139. https://doi.org/10.1016/S0034-4257(96)00167-8

Li, S., Zhang, M., Pei, W., & Lai, Y. (2018). Experimental and numerical simulations on heat-water-mechanics interaction mechanism in a freezing soil. *Applied Thermal Engineering*, 132(Complete), 209-220. doi:10.1016/j.applthermaleng.2017.12.061

Liu, L., Schaefer, K., Zhang, T., & Wahr, J. (2012). Estimating 1992-2000 average active layer thickness on the Alaskan North Slope from remotely sensed surface subsidence. *Journal of Geophysical Research: Earth Surface*, *117*(1), 1–14. https://doi.org/10.1029/2011JF002041

Loh, L. J., Bandara, G. C., Weber, G. L., & Remcho, V. T. (2015). Detection of water contamination from hydraulic fracturing wastewater: A μpAD for bromide analysis in natural waters. *Analyst*, *140*(16), 5501–5507. https://doi.org/10.1039/c5an00807g

McFeeters, S. K. (1996). The use of the Normalized Difference Water Index (NDWI) in the delineation of open water features. *International Journal of Remote Sensing*, *17*(7), 1425–1432. https://doi.org/10.1080/01431169608948714

McKenzie, J. M., & Voss, C. I. (2013). Permafrost thaw in a nested groundwater-flow system. *Hydrogeology Journal*, *21*(1), 299–316. https://doi.org/10.1007/s10040-012-0942-3

McKenzie, J. M., Voss, C. I., & Siegel, D. I. (2007). Groundwater flow with energy transport and water-ice phase change: Numerical simulations, benchmarks, and application to freezing in peat bogs. *Advances in Water Resources*, *30*(4), 966–983. https://doi.org/10.1016/j.advwatres.2006.08.008

Ming, F., Zhang, Y., & Li, D. qing. (2016). Experimental and theoretical investigations into the formation of ice lenses in deformable porous media. *Geosciences Journal*, *20*(5), 667–679. https://doi.org/10.1007/s12303-016-0005-1

Molson, J. W., & Frind, E. O. (2017). *Heatflow - Smoker: DENSITY-DEPENDENT FLOW AND ADVECTIVE-DISPERSIVE TRANSPORT OF THERMAL ENERGY, MASS OR RESIDENCE TIME IN THREE-DIMENSIONAL POROUS OR DISCRETELY-FRACTURED POROUS MEDIA*.

Morse, P. D., & Wolfe, S. A. (2015). Geological and meteorological controls on icing (aufeis) dynamics (1985 to 2014) in subarctic Canada. *Journal of Geophysical Research F: Earth Surface*, *120*(9), 1670–1686. https://doi.org/10.1002/2015JF003534

Mundy, E., Gleeson, T., Roberts, M., Baraer, M., & McKenzie, J. M. (2017). Thermal Imagery of Groundwater Seeps: Possibilities and Limitations. *Groundwater*, *55*(2), 160–170. https://doi.org/10.1111/gwat.12451

Narita, K., Harada, K., Saito, K., Sawada, Y., Fukuda, M., & Tsuyuzaki, S. (2015). Vegetation and Permafrost Thaw Depth 10 Years after a Tundra Fire in 2002, Seward Peninsula, Alaska. *Arctic, Antarctic, and Alpine Research*, *47*(3), 547–559. https://doi.org/10.1657/AAAR0013-031

Niel, K. P. Van, Laffan, S. W., & Lees, B. G. (2004). Effect of Error in the DEM on Environmental Variables for Predictive Vegetation Modelling. *Journal of Vegetation Science*, *15*(6), 747–756. https://doi.org/10.1658/1100-9233(2004)015[0747:EOEITD]2.0.CO;2

Nixon, J.F. (1991) Discrete ice lens theory for frost heave in soils. *Canadian Geotechnical Journal*, 28(6), 843-859.

NWT Government, E. C. (2012). Climate Observations in the Northwest Territories (1957-2012). Retrieved from http://www.enr.gov.nt.ca/node/3697

Olthof, I., & Fraser, R. H. (2007). Mapping northern land cover fractions using Landsat ETM+. *Remote Sensing of Environment*, *107*(3), 496–509. https://doi.org/10.1016/j.rse.2006.10.009

Pérez Díaz, C., Lakhankar, T., Romanov, P., Khanbilvardi, R., & Yu, Y. (2015). Evaluation of VIIRS Land Surface Temperature Using CREST-SAFE Air, Snow Surface, and Soil Temperature Data. *Geosciences*, *5*(4), 334–360. https://doi.org/10.3390/geosciences5040334

Quinton, W. L., Hayashi, M., & Chasmer, L. E. (2011). Permafrost-thaw-induced land-cover change in the Canadian subarctic: Implications for water resources. *Hydrological Processes*, *25*(1), 152–158. https://doi.org/10.1002/hyp.7894

Quinton, W. L., Hayashi, M., & Pietroniro, A. (2003). Connectivity and storage functions of channel fens and flat bogs in northern basins. *Hydrological Processes*, *17*(18), 3665–3684. https://doi.org/10.1002/hyp.1369

Röder, A., Udelhoven, T., Hill, J., del Barrio, G., & Tsiourlis, G. (2008). Trend analysis of Landsat-TM and -ETM+ imagery to monitor grazing impact in a rangeland ecosystem in Northern Greece. *Remote Sensing of Environment*, *112*(6), 2863–2875. https://doi.org/10.1016/j.rse.2008.01.018

Rouse, J. W., Hass, R. H., Schell, J. A., & Deering, D. W. (1973). Monitoring vegetation systems in the great plains with ERTS. *Third Earth Resources Technology Satellite (ERTS) Symposium*, *1*, 309–317. https://doi.org/citeulike-article-id:12009708

Rudolph, D. L., Lotimer, T., & Barker, J. F. (2016). *Final Report Baseline Hydrogeological Evaluation of Central Mackenzie Valley Oil and Gas Exploration Areas Sahtu Region , Northwest Territories*.

Salomonson, V. V., & Appel, I. (2004). Estimating fractional snow cover from MODIS using the normalized difference snow index. *Remote Sensing of Environment*, *89*(3), 351–360. https://doi.org/10.1016/j.rse.2003.10.016

Sass, G. Z., Creed, I. F., Riddell, J., & Bayley, S. E. (2014). Regional-scale mapping of groundwater discharge zones using thermal satellite imagery. *Hydrological Processes*, *28*(23), 5662–5673. https://doi.org/10.1002/hyp.10068

Shimamura, Y., Izumi, T., & Matsuyama, H. (2006). Evaluation of a useful method to identify snow-covered areas under vegetation - Comparisons among a newly proposed snow index, normalized difference snow index, and visible reflectance. *International Journal of Remote Sensing*, *27*(21), 4867–4884. https://doi.org/10.1080/01431160600639693

Solomon, A. (1966). Some Remarks on the Stefan Problem. *Mathematics of Computation*, *20*(95), 347–360.

Twidale, C. R. (2004). River patterns and their meaning. *Earth-Science Reviews*, *67*(3–4), 159–218. https://doi.org/10.1016/j.earscirev.2004.03.001

Unger, A. J. A. (2008). Earth 456 / 656: An Introduction to Numerical Methods in Groundwater Flow and Contaminant Transport Modelling.

Walvoord, M. A., Voss, C. I., & Wellman, T. P. (2012). Influence of permafrost distribution on groundwater flow in the context of climate-driven permafrost thaw: Example from Yukon Flats Basin, Alaska, United States. *Water Resources Research*, *48*(7), 1–17. https://doi.org/10.1029/2011WR011595

Wang, S., Qi, J., Yu, F., & Yao, X. (2013). A novel method for estimating settlement of embankments in cold regions. *Cold Regions Science and Technology*, *88*, 50–58. https://doi.org/10.1016/j.coldregions.2012.12.009

Wu, Y., Sheng, Y., Wang, Y., Jin, H., & Chen, W. (2010). Stresses and deformations in a buried oil pipeline subject to differential frost heave in permafrost regions. *Cold Regions Science and Technology*, *64*(3), 256–261. https://doi.org/10.1016/j.coldregions.2010.07.004

Wukelic, G. E., Gibbons, D. E., Martucci, L. M., & Foote, H. P. (1989). Radiometric calibration of Landsat Thematic Mapper thermal band. *Remote Sensing of Environment*, *28*(C), 339–347. https://doi.org/10.1016/0034-4257(89)90125-9

Xu, J., Abdalla, B., Eltaher, A., & Jukes, P. (2009). Permafrost Thawing-Pipeline Interaction Advanced Finite Element Model. *Proceedings of the ASME 28th International Conference on Ocean, Offshore and Arctic Engineering OMAE 2009*, 1–6. https://doi.org/10.1115/OMAE2009-79554

Yoshikawa, K., Hinzman, L. D., & Kane, D. L. (2007). Spring and aufeis (icing) hydrology in Brooks Range, Alaska. *Journal of Geophysical Research: Biogeosciences*, *112*(4), 1–14. https://doi.org/10.1029/2006JG000294

Y.W., Jame. (1997). Heat and Mass Transfer in Freezing Soil, University of Saskatchewan, Saskatoon, Sask, *PhD thesis*.

Zoltai, S. C., Tarnocai, C., Mills, G. F., & Veldhuis, H. (1988). Wetlands of Subarctic Canada. *Polyscience Publications, 3*, 55–96.

Appendix A: Conceptualization of a model for frost heave induced pipe/main damage

A.1 Frost Heave in Southern Ontario

In recent years, numerical models which solve the heat transport equation in freezing and thawing soils have become an effective means of understanding the dynamic impact that freezing will have on the shallow subsurface. Such models have many applications in the subsurface: They can be used to predict the rate of permafrost thaw, to understand how freezing and thawing affects frost heave and settlement, and to determine the effect that freezing may have on subsurface infrastructure such as pipes and water mains. The latter of these will be the focus for this work. Upon completion of a comprehensive literature review, it was concluded that the majority of numerical modelling efforts aimed at quantifying the effects of frost heave on underground structures are described for the case where a freezing front surpasses the structure of interest. However, it is observed in Southern Ontario that pipe and water main damage occurs during the freezing of the subsurface even when the freezing front does not surpass the structure. In the winter of 2017-2018, the city of Toronto reported approximately 120 water main breaks and 250 frozen pipe service calls (Sasitharan, 2018). In the winter previous, only about 20 water main breaks occurred. Increasingly dramatic changes in daily weather patterns are most likely to blame for these incidents. Environment Canada data indicates more frequent and faster changes in temperature during the 2017-2018 season when compared to the 2016-2017 season. When air temperatures drop quickly, rapid and non-uniform propagation of the freezing front can occur. As mentioned above, the freezing front does not generally surpass pipes and mains even after a dramatic drop in temperature. This raises the question: What processes are responsible for the damage of these underground structures? The research conducted here addresses two unique problems involving the breakage of pipes and mains which are not encompassed by the freezing zone. These are described in ‘Research Objectives’.

A.2 Research Objectives

The work presented here aims to establish conceptual hypotheses for two different cases of differential stress causing pipe/main breakage in the subsurface. Following the conceptual development of these problems, future numerical works and field monitoring will test the hypotheses that are established. Therefore, the conceptual explanations given here were

developed with numerical principles in mind. The two problems and general hypotheses to be addressed are as follows:

I. A frost-susceptible soil (i.e. silt) interacts with a soil of lesser frost-susceptibility (i.e. sand) at a vertical interface within the vadose zone. A pipe/main exists at some depth below the maximum reaches of the freezing front, and a water table exists at some depth below the pipe. Freezing occurs from the surface downward and causes differential stress to be exerted on the pipe/main at the interface of the different soil types.
II. The conditions of case I apply, and at some point, a break in the water main occurs. This break in the water main provides a local source of water to the vadose zone which can increase soil water content and provide more water for freezing and soil expansion, thereby creating a localized region of differential stress acting on the main.

It is noted that these two cases aim to fill gaps which currently exist in the numerical modelling of frost heave/thaw settlement. These gaps include: frost heave in the unsaturated zone, exertion of differential stress *above* a pipe/main, leakage and freezing of pipe/main water in the subsurface, and non-uniform surface water infiltration resulting in differential stress in the subsurface. The sections to follow will summarize the current state of analytical and numerical freeze-thaw modelling, then will detail the hypothetical outcomes of the two cases described above

A.3 Background

A.3.1 Analytical Solutions for Heat Transport

Early numerical models applied to freezing and thawing domains were discretized using analytical solutions to the Stefan Problem (Solomon, 1966). This problem, in the context of hydrogeology, applies a one-dimensional freezing front to a soil column where there is a strict separation between frozen and unfrozen soil. This method of separation is often referred to as front or forward tracking. There is no ‘slushy’ zone, or, in other words, ice saturation must either be 0 or 1. The Stefan problem is originally defined according to the following principles (Solomon, 1966):

- A one-dimensional, semi-infinite domain

- Constant and uniform initial temperature and density at time t=0
- Initiation of phase change releases latent heat
- Each of the two phases are characterized by unique specific heat and thermal conductivity values
- Time-variable specific heat flow is present at the surface only (semi-bounded)
- Phase change temperature is fixed

Many different solutions to the Stefan problem have been proposed. Notable among these are solutions which satisfy the Neumann boundary condition (where specific heat flow is a fixed derivative of time). This boundary condition most closely approximates the behavior of heat in a deformable (i.e. soil) matrix. A recent polynomial solution to the Stefan Problem defines the temperature distribution resulting from the analytical solution as follows (Kot, 2017):

$$(14) \qquad \overline{T}(\overline{x},\overline{t}) = \begin{cases} \overline{T}(\overline{x},\overline{t}), & 0 \le \overline{x} \le \overline{s}(t), \quad \overline{t} > 0, \\ T_m, & \overline{x} \ge \overline{s}(t), \quad \overline{t} > 0 \end{cases}$$

Where the heat conduction equation is satisfied by the following conditions:

$$(15) \qquad \frac{\partial \overline{T}}{\partial \overline{t}} = \kappa \frac{\partial^2 \overline{T}}{\partial \overline{x}^2}, \qquad 0 < \overline{x} < \overline{s}(\overline{t}), \qquad \overline{t} > 0,$$

$$-\lambda \frac{\partial \overline{T}(0,t)}{\partial \overline{x}} = Q(\overline{t}), \qquad \overline{t} > 0$$

and the conditions at the phase change boundary are:

$$(16) \qquad \overline{T}\left(\overline{s}(\overline{t}),\overline{t}\right) = \overline{T}_m, \qquad \overline{t} > 0,$$

$$-\lambda \frac{\partial \overline{T}(\overline{s}(\overline{t}),\overline{t})}{\partial \overline{x}} = \rho L \frac{d\overline{s}(\overline{t})}{d\overline{t}}, \qquad \overline{t} > 0$$

and the initial condition applied to the phase change front is:

$$(17) \qquad \overline{s}(0) = 0$$

Where:

$Q = specfic\ heat\ flux\ at\ surface,$

$T = temperature$

$T_m = temperature\ of\ phase\ change,$

$t = time$

$s = position\ of\ the\ phase\ change\ boundary$

$\lambda = heat\ conductivity\ coefficient$

$\rho = density$

$\kappa = thermal\ diffusivity: \frac{\lambda}{c\rho};\ c = specific\ heat\ capacity$

Though the Stefan Problem was an important development in the design of heat transport models, it was limited by its strict freezing front. In reality, ice saturation varies between 0 (unsaturated) and 1 (completely saturated). The Lundardini analytical solution – which has been adapted for use in more recent heat transport models – provided a slushy zone which could accommodate ice saturation values between 0 and 1 (Lundardini, 1985). The Lundardini solution is an exact analytical solution which solves a problem identical to the Stefan Problem, but with the addition of a slushy zone. The slushy zone introduces non-linearity into the problem because it is not strictly defined by a singular temperature. Therefore, a freezing function must be chosen to describe the relationship between temperature and saturation. In the design of a heat transport model, no one freezing function may always be applicable. As they are empirically determined, certain functions are more applicable to certain conditions (i.e. degree of heterogeneity, initial saturation, porosity, etc.). Many heat transport models will include a choice of several freezing functions, or the option to include a subroutine with an alternative freezing function.

The heat conduction equation, whose conditions detailed in equation 15 must be satisfied to solve the Stefan problem using analytical solutions, can be described as:

$$(18) \qquad \left(C - L\rho_i \frac{\partial \theta_i}{\partial T}\right)\frac{\partial T}{\partial t} = \nabla(\lambda_e \nabla t)$$

Where:

$C = volumetric\ heat\ capactity$

$L = latent\ heat\ of\ phase\ change$

$\rho_i = density\ of\ ice$

$\theta_i = volumetric\ fraction\ of\ ice$

$\lambda_e = heat\ conductivity\ of\ soil$

$T = temperature$

$t = time$

(Hawlader, et al. 2006)

In some cases, an equivalent or apparent heat capacity is used to replace the latent heat of phase change, such as in the works of Fu, et al. (2014) on numerical simulations of frost heave, and in McKenzie et al. (2007) on the simulation of groundwater flow with heat transport. Nevertheless, these equations form the basis for numerical simulations of heat transport in a porous medium.

A.3.2 Defining Moisture Migration and Frost Heave

When the subsurface is subjected to freezing and thawing, it also undergoes volumetric change as a result of phase change. Primary frost heave causes water to freeze and expand the soil skeleton (in situ freezing) and secondary frost heave causes moisture to migrate into the freezing front. The former of these is easily simulated numerically through use of a freezing function which defines the relationship between saturation and temperature. Most commonly, freezing functions are linear, as follows:

$$(19) \qquad S_w = mT + 1\ if\ T > Bt\ or\ S_w = residual\ saturation\ if\ T < Bt$$

Where S_w is the saturation of water, m is the slope of the function, T is the temperature, and Bt is the temperature at which residual saturation (remaining unfrozen water) is reached (MacKenzie, et al. 2007). A freezing function must be defined to account for the freezing point depression of water as water saturation decreases. This hysteresis results from the amplification of capillary forces induced by the conversion of water to ice (MacKenzie, et al. 2007). Capillary forces are amplified in this way because as water freezes, a greater proportion of the remaining water exists in thin films. At some point, a residual saturation is reached and a continued decrease in temperature will not freeze residually remaining water. Super cooled water will always remain at below freezing temperatures because dissolved solids are largely excluded from the freezing process (MacKenzie, et al. 2007). In the case of a linear function, a below freezing temperature is

achieved as the water saturation moves towards 0. However, once a certain temperature is reached, water saturation will remain constant even though temperature continues to decrease.

Secondary frost heave is a more complex process which is resultant of capillary forces (tension) drawing water into the freezing front from a non-local location. Numerically, secondary frost heave is generally based on a pre-determined empirical coefficient which estimates the volume expansion due to moisture migration. This coefficient will be variable depending on the soil type. This method of predicting frost heave is known as a Segregation Potential model, an example of which is given by Fu et al. (2014):

$$\Delta H = \Delta h_f + 0.09 n \Delta Z = 1.09 SP_0 gradT(t) \Delta t + 0.09 n \Delta Z \quad (20)$$

Where:

$\Delta H = the\ amount\ of\ frost\ heave,$

$\Delta h_f = amount\ of\ segregation\ frost,$

$SP_0 = segregation\ potential,$

$gradT(t) = temperature\ gradient\ at\ time\ t,$

$n = porosity\ of\ soil,$

$\Delta Z = displacement\ of\ freezing\ front$

The values ‘0.09’ and ‘1.09’ are empirical coefficients representing expansion due to in situ freezing and moisture migration (cryosuction), respectively. Certain models may only account for primary (in situ) freezing and omit the effects of secondary frost heave. This is common for models which incorporate groundwater flow along with heat transport. Such models will consider vertical deformation to be the result of only in situ phase change. For example, *Heat-flow smoker*, a groundwater flow-heat transport model published by Molson and Frind in 2017, considers vertical element deformation as follows:

$$dz^e = \theta S_w * \Delta W^u \left(\frac{\rho_w - \rho_i}{\rho_i}\right) * Z_L^e \quad (21)$$

Where:

$\theta = porosity,$

$S_w = water\ saturation,$

$\Delta W^u = unfrozen\ moisture\ content\ over\ timestep\ t,$

$\rho_w = water\ density,$

$\rho_i = ice\ density,$

$Z_L^e = original\ element\ height$

(Liu et al., 2012)

It is noted that segregation potential models do not predict the discrete location of ice lenses. Rather, they estimate the total amount of frost heave based on the expected volumetric change from in situ and secondary freezing. The section to follow will discuss the theory of discrete ice lens formation.

A.3.3 Discrete Ice Lens Formation

Ice lenses form entirely from secondary frost heave processes (moisture migration and cryosuction) and result in the separation of soil grains to allow the formation of a completely solid lens of ice within the subsurface. Discrete ice lens theory has been described analytically by Nixon in 1991. This theory is based on the following principle:

$$(22) \qquad P_{ice} = P_0 + P_{sep}$$

Where P_{ice} is the pressure in the ice, P_o is the overburden pressure, and P_{sep} is the pressure required to initiate the separation of the soil skeleton. In order for an ice lens to form, the ice pressure must exceed the combined overburden and separation pressure (Gilpin, 1980). The separation pressure can also be described as the internal pressure, and has been measured empirically in several studies. The actual movement of water into the freezing fringe is then governed by Darcy's Law. The use of Darcy's law (groundwater flow) invokes the necessity of a relative permeability function which is used to prevent permeability from reaching zero when

residual saturation is achieved. This function is a necessity when groundwater flow is considered with heat transport because a relative permeability of 0 will result in no flow. Generally, relative permeability functions are linear or power functions. An example of a linear function is given below (MacKenzie, et al. 2007):

$$(23) \qquad K_r = \left(10^{-6} - \frac{1}{Bt}\right) * \ T + 1 \ if \ T > Bt \ or \ K_r = \ 10^{-6} \ if \ T < Bt$$

Where K_r is the relative permeability and Bt is the temperature at which residual saturation is reached. When the temperature in an element is less than the temperature at which residual saturation is reached, permeability is reduced to such a small value that flow is essentially not occurring but solution convergence is still possible.

A study by Ming et al (2016). examines ice lens formation in a soil column, and then compares the results of this experiment to a numerical model (COMSOL) that is used to predict the discrete location of ice lenses. Very few numerical models have attempted to predict the exact location and size of an ice lens. This study uses a column of silty-clay with an initial saturation of 16% and freezes it from the top down using a cooling plate. In different scenarios, an ice lens formed near the bottom of the freezing front as a result of moisture migration from water reserves below. It was found when the overburden pressure (manipulated by a pressure plate) was increased, the flux of water into the freezing fringe was decreased, and that when the temperature of the cooling plate was decreased, the maximum flux of water into the freezing fringe was obtained more quickly. Total frost heave in the soil column was greatest when the overburden pressure was non-existent (0 Kpa). The results from this column experiment were compared to the results of a numerical code that was developed using COMSOL. Following Gilpin's theoretical description of ice lens formation, the numerical model used in this work predicted the location and extent of discrete ice lenses with time, such that the number of ice lenses within the freezing fringe increases with time. Ice lenses do not generally form in the upper reaches of the frozen zone as they can only form when the freezing process is occurring sufficiently slowly (which generally occurs after the freezing front surpasses some depth) to allow the ice pressure to exceed the combined overburden and separation pressure. A source of water below the freezing front must also be accessible. When the temperature gradient is changing quickly, in situ freezing will occur before the required separation pressure is reached.

The results of this study have several important implications for the cases addressed by this thesis. Overburden pressure and temperature gradient have a significant impact on the amount of water that can be drawn in by the freezing front. It then follows that initial saturation in the vadose zone will be an important consideration. Greater initial saturation will result in larger overburden pressure, which may limit ice lens formation, therefore limiting overall frost heave. It is noted that though ice lens formation may be limited in this way, overall stress exerted on the porous media may be greater in cases where the saturation is also greater, as this increases the pressure above the freezing front.

Ice lenses tend to develop in a horizontal sequence as the freezing front progresses downwards vertically. Only the lowermost (warmest) ice lens in a sequence will be growing, and the lenses above it are considered to be stable (Arenson, et al. 2016). The specific conditions which lead to one ice lens reaching maximum growth and a new ice lens beginning to form beneath it is still contested. Gilpin's model, adapted for use in the COMSOL numerical model described above, is one approach of several which have been developed over the last several decades. This particular one is highlighted in this work as the agreement between the experimental investigations and the numerical modelling was strong. Though ice lens formation is not considered in the conceptual problems of this thesis, an understanding of their formation aids in the understanding of stress distribution in the porous media.

A.3.4 Defining Stress-Strain associated with Frost Heave

In addition to simulating heat transport and frost heave/thaw settlement, many problems require that a stress-strain field resulting from frost heave and thaw settlement also be computed. This is necessary when determining the effect of freezing soil on infrastructure such as foundations, roads, and pipes. Such models, referred to here as mechanical deformation-heat transport (MD-HT) models, do not generally consider groundwater flow. A model which considers heat transport, frost heave/settlement, groundwater flow, and stress within the soil skeleton introduces significant challenges for achieving numerical convergence. Groundwater flow – and discrete ice lens formation – are therefore normally omitted; secondary frost heave is approximated by a Segregation Potential model instead.

As aforementioned, MD-HT models will also quantify the amount of stress applied at each node and time step within a domain which is allowed to deform. The set of equations which define the mechanical deformation process depend on how the soil body is defined. Generally, the soil body is defined by a porosity-elasticity relationship where higher porosity materials are considered to be 'less elastic'. Alternatively, certain materials (ex. clay) may be considered entirely inelastic. This is to say that following a consolidation event, they cannot revert to their original position. The compressibility of a material is dictated by its porosity such that mediums which are more compressible behave plastically, and mediums which are less compressible behave elastically (Fetter, 2014). Because MD-HT models do not solve the groundwater flow equation, saturation is not a derivative of time but rather is fixed, in most cases to 1 (fully saturated).

There are numerous theories and systems of equations which describe stress and strain in a porous medium. An example given by Yaping Wu, et al. (2010) using *ANSYS* describes the total strain within a frozen soil domain as follows:

$$\{\varepsilon\} = \{\varepsilon_e\} + \{\varepsilon_p\} + \{\varepsilon_h\} \quad (24)$$

Where:

$\{\varepsilon_e\} = elastic\ strain,$

$\{\varepsilon_p\} = plastic\ strain,$

$\{\varepsilon_h\} = volumetric\ strain$

Elastic and plastic strain are governed by a complex set of equations which can be found in Yaping Wu, et al. (2010). Volumetric strain considers frost heave due to phase change in situ and due to moisture migration (indirectly):

$$\{\varepsilon_h\} = [\varepsilon^v, \varepsilon^v, \varepsilon^v, 0, 0, 0]^{T}/_{3} \quad (25)$$

where $\boldsymbol{\varepsilon^v}$ is the volumetric expansion strain in the x, y, and z directions.

Equation 24 both quantifies frost heave, and explicitly determines its contribution to the total strain within the porous media. This is in contrast to equation 21, which does only the former. The works of Yaping Wu. et al. attempt to determine the nodal stress surrounding a pipeline which exists in a dynamic permafrost environment subjected to the differential stress caused by frost heaving and thawing. Here, a pipeline exists right above the permafrost table, and a region below the pipe is allowed to thaw and heave with the active layer due to greater frost susceptibility. This creates a transition zone between the heaving zone and the non-heaving zone which exerts differential stress on the pipe. The results of this work indicate that a larger transition zone between the two soil conditions minimizes the deformation of the pipeline. The largest amount of deformation which occurred in the pipe was ~10cm when the transition zone was small. The penetration of the freezing front (in the area in which freezing was allowed) reached 0.75 meters below the pipe. In addition to determining the overall heave/settlement in the soil and the displacement of the pipe, the model used in this work also calculated the stress along the length of the pipe to determine whether the yield stress of the pipe was exceeded.

A study by Wang et al. (2013) considers groundwater flow in a MD-HT model. Wang et al. (2013) describe a model for embankment settlement using *FLAC-3D* where mechanical deformation is considered in the following way:

- Set of equations A – Frozen soil: Subsidence is dominated by soil creep. Soil creep occurs in frozen soils that exhibit visco-plastic and visco-elastic behavior. This process is described by the Drucker Prager criterion, where visco-plastic behavior is approximated by Maxwell and Kelvin bodies, and visco-elastic behavior is approximated by a Bingham body.
- Set of equations B – Unfrozen soil: Subsidence is dominated by consolidation due to grain rearrangement and drainage.

The model decides which set of equations to use based on the nodal temperature. In addition to characterizing the mechanical behavior of the soil, this model also solves the heat transport and groundwater flow equations such that groundwater flow is allowed to occur in a frozen or partially frozen domain. When this is the case, a relative permeability function must also be established. This function relates the permeability of the media to its ice content. In most cases, and in the work of Wang, et al., temperatures exceeding the phase change threshold result in a

relative permeability of 0. If flow is not allowed, the groundwater flow equation will no longer be calculated. Implementation of a decision tree such as this eliminates the need for the model to calculate a solution to the flow equation unless it is needed. It is noted that the groundwater flow equation is *not* used to describe discrete ice lens formation, but rather just to more realistically simulate the conditions of saturation which occur in a natural environment.

A.3.5 Research Gaps

Based on the literature reviewed for this work, several gaps related to numerical freezing soil simulations are observed. Firstly, the unsaturated zone is rarely considered. This is largely due to the non-linearity that including it introduces into the overall numerical problem. However, to more realistically simulate freezing processes in Southern Ontario where a significant vadose zone exists, it should be included in numerical simulations. Secondly, the process of discrete ice lens formation is not generally incorporated into models which also describe the stress-strain field within the porous media. Including ice lens formation requires that that moisture migration be defined, generally through Darcy's Law, and therefore introduces a need for the model to describe both groundwater flow, and the conditions which will lead to the formation of an ice lens. Indeed, this is a complex problem to describe mathematically, but it is the interactions between these processes that are expected to play a large role in the distribution of stress within a freezing porous media. Finally, it is noted that studies examining frost heave and ice lens formation rarely consider the distribution of stress in both the upward and downward directions. Certainly, frost heave occurs primarily in the upward direction (relative to the location of the freezing front) due to the lack of force (overburden material) acting against it. It is far more difficult for heaving processes to result in downward strain as the force acting against these processes is greater from below. However, it is still expected that some strain occurs below the freezing front, and that this may be a cause of the pipe/main breakage that is observed in Southern Ontario. Several studies observe that frost heave (the actual amount of surface upheave) occurs more quickly at the beginning of freezing, due to a steeper temperature gradient, but then declines after a period of intense growth (Abdalla et al. 2015). It is expected that during this time, propagation of the freezing front continues and that frost heave occurs in the downward direction. The majority of investigations on frost heave compute a total amount of

frost heave over a given time period, but do not quantify either the amount or the distribution of stress resulting from that frost heave. Therefore, it remains a distinct possibility that pipe and water main damage may be related to late stage frost heave.

A.4 Conceptual Models

A.4.1 Case 1

In case 1, silt (a frost-susceptible soil), interacts with sand (a soil of low frost-susceptibility) at a vertical interface as shown in Figure 37. A pipe or water main exists within the vadose zone above the water table but below the maximum depth of the freezing front. As the freezing front propagates downwards from the ground surface, the silt expands more than the sand due to its greater porosity and water-retaining properties. This process creates a differential stress field within the porous media which is hypothesized to exert significant pressure onto pipes and mains at the location of the changing soil interface. Depending on the conditions in the porous media, the greatest damage to the pipe will occur at the strongest deflection points; these are commonly on either side of the point where maximum stress is observed (Xiang Huang, 2018). Ice lens formation will not be examined for this case; only primary (expansion in situ) and indirect secondary (estimation of expansion due to moisture migration) will be considered.

Several factors may influence the degree to which stress is exerted on the pipe. These include:

I. *Depth of the water table:* A shallower water table is expected to result in easier availability of water for cryosuction but also to increase the force acting upon the freezing front from below, thereby decreasing the stress exerted in the downward direction and limiting the strain (deformation) experienced by the soil skeleton. When there is more free pore space between the water table and the bottom of the freezing front, compaction potential is expected to be greater.

II. *Temperature gradient:* Slower freezing of the active zone is expected to result in a greater amount of secondary frost heave which in turn will exhibit greater stress on the pipe. Greater secondary frost heave does not imply ice lens formation, but rather that the secondary frost heave component of a segregation potential model will increase.

III. *Initial saturation in the vadose zone:* The impact of the degree of saturation in the vadose zone has several complex implications. Firstly, higher saturation is expected to create greater in situ frost heave due to the volume expansion of freezing water. Secondly, it will increase the overburden pressure above the freezing front resulting in less cryosuction from unfrozen water outside of the freezing fringe. Thirdly, the distribution of stress in the porous media is expected to be greater in the downward direction when the overburden pressure is greater. The trade-off between the decrease in secondary frost heave and increase in overburden pressure will be explored in this modelling effort.

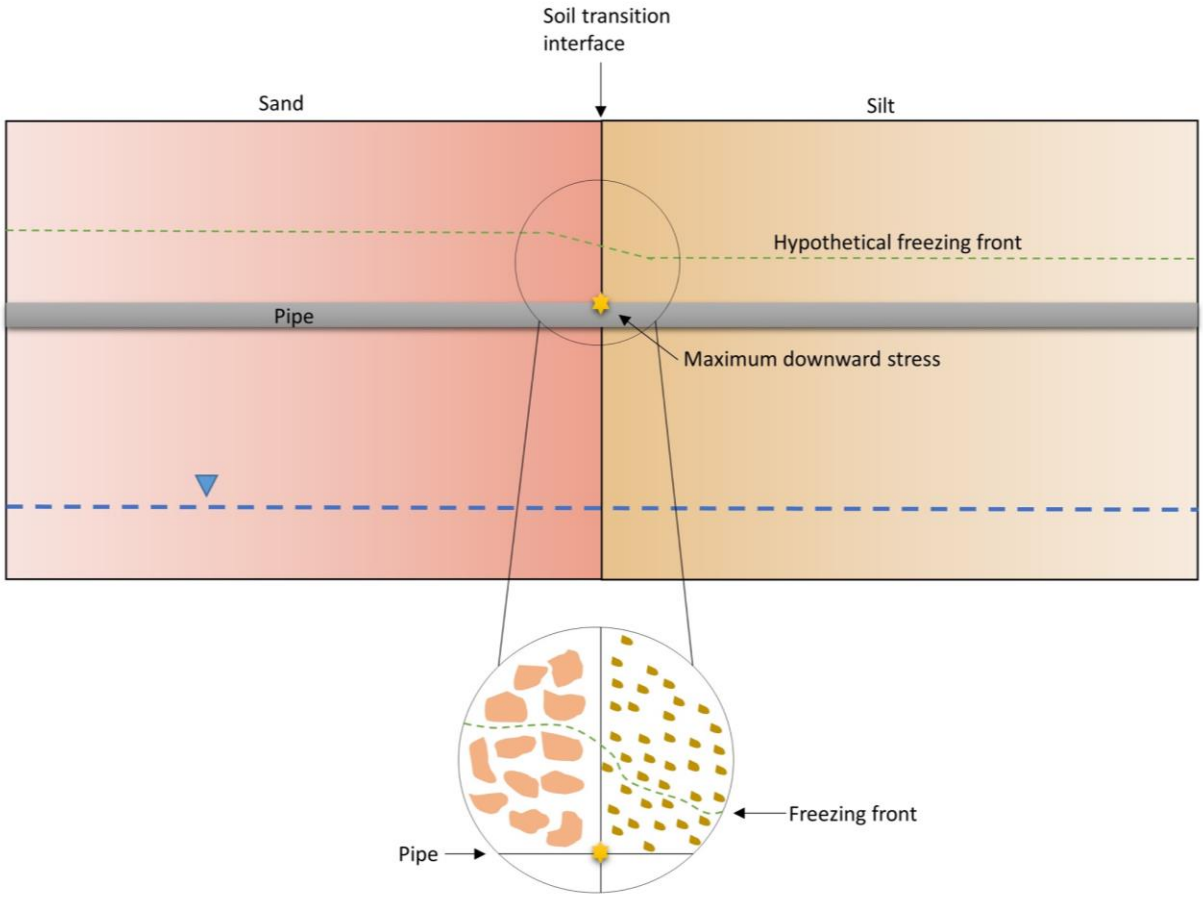

Figure 1a. Conceptual diagram for case 1.

IV. *Depth of freezing front:* A deeper freezing front is expected to exert greater downward force onto the pipe. Presumably, a deeper freezing front results in greater overburden pressure, and therefore greater compaction potential below the freezing front. It should also be noted that overburden pressure may consist of buildings, roadways, etc. which are above the freezing zone and increase the force acting against frost heave in the upward direction. Greater pressure overlying the freezing zone is certainly expected to shift the distribution of stress in the downward direction, but it is also noted that many man-made features which increase the overburden pressure also serve to insulate the ground beneath them, thereby reducing the potential for freezing. The overburden pressure should be explicitly taken into account as both the soil matrix and any infrastructure overlying it.

V. *Backfilling material:* The backfilling material around the pipe is not considered in this work. Many older pipes and mains do not have any backfilling material surrounding them, and even newer pipes which do have still been damaged during the winter. When backfilling material is used, it is normally a gravelly/sandy mixture with a low heaving ratio and high permeability (Abdalla, et al 2015). These types of materials also have much lower potential for compression when compared to a silt or a clay. They are used for this reason – they increase the force acting against the freezing front thereby reducing potential for stress to be directed downward. Why pipes and mains surrounded by this material are still at risk is further explored in case 2.

A.4.2 Case 2

Case 2 presents the same initial conditions as case 1, with the addition of an undetected break in the water main at some point during the freezing process, which results in a continuous leak (shown in Figure 38). In order to examine the influence of the different soil types, the leak is situated at the interface between the soil sections. The leaking water will migrate away from the break and redistribute within the surrounding unsaturated soils as influenced by the different physical soil characteristics. This influx of a local water source in the vadose zone is expected to

exert a differential stress on the water main directly above the location of the leak. This is due to the new supply of water which can be drawn up to the freezing fringe via cryosuction, and/or freeze in situ above the main. It is expected that downward force will be exerted in the same way as it is in Case 1, but that it will be greater due to the additional supply of water which may not only cause differential frost heave, but also ice lens formation in the fine-grained soil. In addition to the factors listed for case 1, the exertion of stress on the main due to a leak in that same main may be affected by:

I. *Timing of leak:* The leak is more likely to occur as the freezing front gets closer to the pipe. However, if the leak occurs following a period which is very cold and rapidly warms up again (as has been observed frequently in recent Southern Ontario winters), the leak may not cause significant frost heave if it is stopped before a period of cooling begins again. Therefore, leaks are expected to cause the most amount of damage when atmospheric temperatures are 'cold' for a sufficient amount of time to allow frost heave to continue occurring after the main break, or when a small continuous leak remains undetected for a long period of time. In the latter case, a major break causing water main failure is expected to occur given enough time. A deeper freezing front may also be resultant from a long period of cold weather. This is noted as having a two-fold effect on the potential for ice lens formation - Ice lenses have a greater chance of forming when freezing occurs slowly (as it normally does when the freezing front approaches its maximum depth) but the greater the overburden pressure, the lower the ice lens initiation temperature (Tezera, et al. 2012).

II. *Suction in the freezing fringe:* Suction within the freezing fringe is linearly related to temperature such that for every 1 degree (Celsius) decrease in temperature, suction increases by 1250 kPa (Konrad, 1944). Therefore, cooler temperatures in the freezing fringe have greater potential to draw in unfrozen water. That being said, the conditions for ice lens initiation must still be met if an ice lens is to form: A certain temperature and separation pressure must be overcome depending on the external stress acting on the location of the ice lens formation. Tereza, et al. (2012) relate the overburden stress to both the temperature and separation pressure conditions required for ice lens formation.

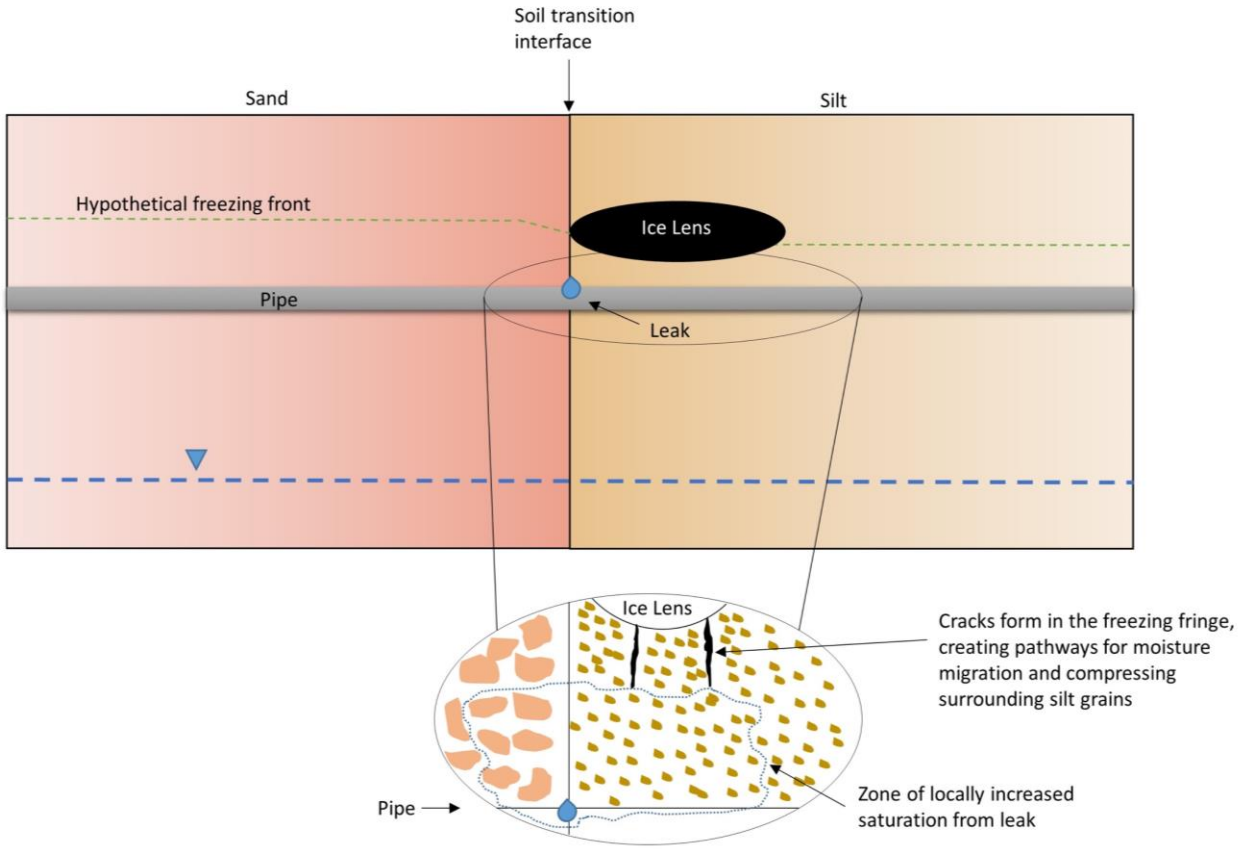

Figure 1b. Conceptual diagram for Case 2.

A.5 Adaptation for Numerical Modelling using ABAQUS

A.5.1 Previous works using ABAQUS

As previously discussed, solving a numerical problem involving heat transport, stress-strain, deformation, and moisture migration is computationally challenging in terms of both model design and solution convergence. Few existing commercial models will perform all of these processes without significant modification and/or the addition of new subroutines. The addition of unsaturated flow conditions adds another element of non-linearity which can be challenging to model even without stress-strain and deformation simulations.

Upon research of several different currently available numerical models, *ABAQUS* was determined to be a model which should be able to successfully solve the cases described above. *ABAQUS* provides many default solutions for the required processes, but also allows for the flexibility of implementing user subroutines where preferred. A few examples of applications of *ABAQUS,* which are relevant to the cases in this study, are given below.

In 2009, Xienfeng Xu et al. use ABAQUS to address the thaw settlement problem, which occurs in permafrost that thaws when a warm oil pipeline generates a 'thaw bulb'. Rather than being fully coupled, the problem is simulated in two parts: First, the heat transfer is simulated using 2D 4-node linear heat transfer quadrilateral elements, then the thaw settlement is simulated using 3D 8-node brick with tri-linear displacement and pore pressure elements. The authors note that heat transport is negligent in the longitudinal direction, therefore the heat transfer process is two dimensional. They also neglect advective heat transport resulting from moisture migration as it accounts for a small fraction of the thawing. The Drucker-Prager/Cap Plasticity model is used to predict the thaw settlement and associated strain within the pipeline. This deformation model is one of several which can be pre-selected within ABAQUS.

For this problem, the top surface of the model is the only location in which free drainage is allowed. Therefore, frozen water which becomes liberated in the thaw bulb can only drain to the surface. Though this may be a significant simplification in terms of groundwater flow, it minimizes the complexity of the numerical model when understanding of the flow system is not essential. Defining the method of frost heave is also not necessary for this model as the authors

are interested in the result of thaw settlement. Following this paper, ABAQUS described the non-coupled method in an example case (found in the user manual) and compared it to a fully-coupled analysis for the heat transfer and deformation (consolidation). The results were not significantly different.

Another problem, modelled using ABAQUS by Abdalla et al. (2015) aimed to quantify the frost heave that could occur as a result of a buried, chilled pipeline. In this scenario, an extended porosity rate function is used to describe the frost heave: Assuming that the overall volume of a soil body changes in response to heaving and thawing, the porosity rate (time derivative of porosity) reflects either the expansion of pore space due to frost heaving, or the contraction of pore space due to consolidation. Three correction factors are introduced into the porosity rate function for this work:

1. Consideration of the temperature gradient: Frost heave growth magnitude is proportional to the absolute value of the temperature gradient (such that frost heave can be spatially discontinuous regardless of other soil properties).
2. Consideration of overburden stress: A stress factor of 1.0 is used when frost heave growth is unconfined, and decreases toward zero as growth becomes more confined.
3. Consideration of initial porosity: Since frost heave occurs more quickly during earlier stages, a porosity correction factor relates the ability of a soil to hold ice (higher porosity soils) to the porosity correction factor such that a lower correction factor is used when the porosity of the soil is higher.

This approach, as used by Abdalla et al. (2015), is an efficient and accurate way to predict the total amount of frost heave and/or thaw settlement within the soil. It was implemented through the ABAQUS subroutine UXPAN (), which allows the user to define the equations governing the deformation of the soil resulting from freezing or thawing. The porosity rate function cannot provide the discrete location of ice lenses or determine the distribution of stress resulting from freezing and thawing processes. Therefore, the dependence of frost heave on overburden pressure, which Abdalla et al. employ, will be utilized in the modelling for cases 1-3 in addition to a porous elastic model which will predict the stress-strain field.

A.5.2 Recommendations for Modelling Cases 1 & 2 with ABAQUS

In order to effectively model the cases 1-2 described above, the following processes need to be defined numerically:

***Heat transport within the porous medium*:** Given the number of other complex processes that must be defined in this physical scenario, the heat transport process should be simplified as much as possible. Because the velocity of water entering the freezing front is very low, convective heat transport can be excluded. Several studies have shown that conductive heat transport is negligible in the case of frost heaving (Y.W. Jame, 1997; Nixon, 1991; Li et al. 2018). Only conductive heat transport, resultant from the release of latent heat from the subsurface in the case of freezing, should be considered. ABAQUS can couple heat transport with thermal stress/strain and pore fluid movement.

Thermal expansion (frost heave): Primary frost heave (in situ thermal expansion) is described in ABAQUS by a relation between the temperature gradient between t_0 and t_1 and a thermal expansion coefficient. Because the expansion of water is dependent on its temperature (though is approximately 10% by volume given the range of temperatures over which freezing is likely to occur in soils), a new thermal expansion coefficient should be calculated at each time step depending on the current nodal temperature at that time step. The response of the liquid (water) and solid (soil grain) to thermal expansion is different. For the solid:

$$\frac{\rho_g}{\rho_g^0} \approx 1 + \frac{1}{K_g}\left(s_w + \frac{\bar{p}}{1-n-n_t}\right) - \varepsilon_g^{th} \qquad (26)$$

Where:

$\rho_g = density\ of\ solid$

$K_g = bulk\ modulus\ of\ solid$

$s_w = saturation\ of\ the\ wetting\ phase$

$\varepsilon_g^{th} = volumetric\ thermal\ strain$

The above equation approximates the change in density of the soil matrix upon freezing. The density of the soil is required to describe the total overburden pressure acting on the unfrozen

area below the freezing front. It is assumed that the pressure applied to the non-wetting (gas/air) phase is acceptably small and consistent enough that it is not considered in the definition of effective stress. The response of the liquid to effective stress (freezing) is given as follows:

$$\frac{\rho_w}{\rho_w^0} \approx 1 + \frac{\mu_w}{K_w} - \varepsilon_w^{th} \quad (27)$$

Where:

$\rho_w = density\ of\ liquid$

$K_w = bulk\ modulus\ of\ liquid$

$\mu_w = wetting\ liquid\ pressure$

$\varepsilon_w^{th} = volmetric\ expansion\ of\ liquid\ (induced\ by\ temperature\ change)$

This equation describes the change of density in the liquid portion of the domain in response to thermal expansion (ie – the decreased density of ice in response to expansion).

Deformation below the freezing front: Given that a very small element size and time step will be required for this model, it is recommended that the model use a decision tree based approach in order to decide whether an element should be experiencing thermal expansion, or deformation as a result of thermal expansion. Deformation below the freezing front should not occur until a certain overburden pressure is achieved because the distribution of stress in the downward direction is not expected to occur until the freezing front reaches a certain depth (which will depend on physical soil characteristics). At this depth, the energy required to heave more soil upward is greater than the pressure acting on the current point of freezing. At what overburden pressure this occurs will be variable depending on vadose zone saturation, grain size, porosity, and initial effective stress. Using this approach, the decision tree would operate as follows:

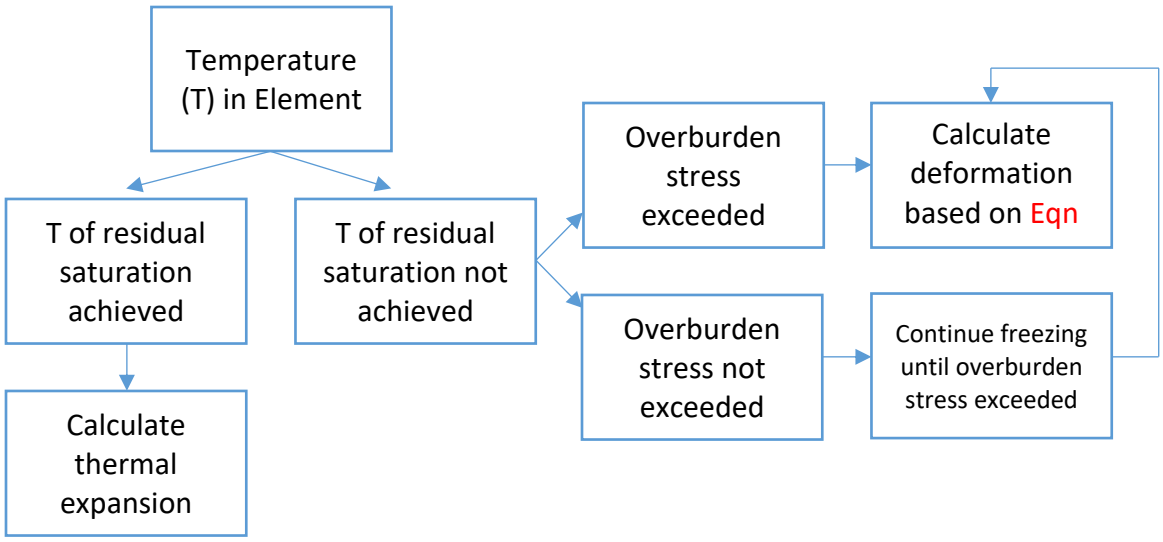

Figure 3a. Decision tree used to determine whether mechanical deformation should be included in the modelling step.

The temperature at which residual saturation is reached is considered to be the point when freezing can no longer occur. It is recommended, for simplicity, that the freezing function be linearly defined such that a decrease in saturation will result in a depression of the temperature required to begin freezing.

The mechanical constitutive equations used to describe the consolidation and deformation below the freezing front can be one of many soil deformation models given by ABAQUS. Considering that it is not important to know the rebound properties of the soil after thawing, the porous elastic model is recommended to define the behavior of the non-frozen soil which is allowed to deform:

$$\frac{k}{1+e_0}\ln\frac{p_0+p_t^{el}}{p+p_t^{el}} = J^{el}-1 \qquad (28)$$

Where:

$$k = the\ logarithm\ of\ the\ bulk\ modulus$$

$$e_0 = intial\ void\ ratio\ (porosity)$$

$$p = equivalent\ pressure\ stress$$

$$p_0 = initial\ value\ of\ equivalent\ pressure\ stress$$

$$p_t^{el} = elastic\ tensile\ strength$$

$$J^{el} =' elastic' portion\ of\ the\ volume\ ratio\ between\ intial\ and\ current\ time$$

Here, the equivalent pressure stress must be given as the overburden stress acting on the element which is allowed to deform. The elastic portion of volumetric change within the porous media is proportional to the logarithm of the pressure stress (overburden stress) applied above it. Use of the porous elastic model should be able to determine the amount of deformation occurring in terms of porosity, consolidation, and nodal stress. Of these, the nodal stress will be the most important metric as it indicates at which locations within the model the greatest stress is occurring. This can be related to the location of the hypothetical pipe.

Secondary Frost Heave: It is expected that predicting the discrete location of ice lenses within the freezing front will be ambitious at this point. This may be something to explore in the future if the proposed numerical model can be successfully implemented by considering secondary frost heave indirectly first. It is recommended that this be accomplished using a Segregation Potential (SP) model. In order to use this model, moisture migration must also be defined (see the section below). The SP model uses empirical coefficients to predict the amount of primary and secondary heave occurring within the freezing fringe, and also determines a value for Segregation Potential – this is the pressure gradient between the freezing fringe and the closest point at which water can be drawn into the fringe. Normally, the pressure within the freezing fringe is negative, thereby inducing the effects of cryosuction. The SP model does not take into account the separation pressure nor temperature required to initiate an ice lens, but does predict the resultant primary/secondary heave and the saturation field.

Moisture Migration*:* Moisture migration into the freezing fringe should be defined by either the Forchheimer or Darcy's Law. Either can be utilized by ABAQUS in combination with partially saturated or fully saturated flow. Given that Darcy's Law is more commonly used for applications involving secondary frost heave, it is recommended that it be used here as well. The ABAQUS user manual gives a detailed explanation regarding solution convergence for a coupled pore fluid-heat-stress analysis. Convergence can be automatically maintained by selecting an automatic incrementation scheme.

Boundary and initial conditions for the model are recommended as follows:

- Heat conduction (release of latent heat) allowed only at surface. Lateral heat conduction is generally negligible. The bottom of the model should represent a constant temperature boundary. The temperature at the top of the model will depend on the scenario that is being considered. Generally, the temperature at the top of the domain is given by a sinusoidal amplitude function when considered over an entire season, and as a step function when considered for a time period within a particular season.
- The bottom of the model can be represented in two ways: Firstly, it can be represented as the top of the water table such that the model would only consider the vadose zone. Secondly, it can be represented as a no-flow boundary such that the water table, at whatever depth it exists, can exhibit steady-state or transient behavior. The former of these is a simplification, though it is not clear what effect this may have on the total amount of frost heave. Therefore, both boundary options should be tested. It is expected that the water table exists at a sufficient depth that it would not supply a significant amount of water to the freezing fringe, however, the magnitude of this simplification will depend on the local pressure gradient between the water table and the bottom of the freezing fringe.
- Deformation should be allowed only in the vertical direction such that the lateral model boundaries are restricted from exhibiting any displacement. This is expected to be a reasonable assumption given that frost heave modelling normally considers thermal expansion to be an isotropic process. Furthermore, the overburden pressure created by the freezing process is not expected to generate significant soil creep or other lateral displacement.
- All boundaries should be no-flow boundaries in the case where the bottom boundary represents the bottom of the vadose zone. If the water table is included in the model, then flow will be allowed on both sides of the saturated zone and the flux through the saturated zone can force the water table to remain in the same position (steady-state condition) or allow the water table to fluctuate (transient condition).

As this specific type of model has not been constructed previously, the method used to achieve the final model will need to be adaptive. The goal of this section is not to simulate the models, but to provide guidance as to how the models should be considered. Table 8 below presents the parts and steps that should be used in each case. ABAQUS allows a model to be separated into an infinite number of parts which exhibit a certain material behavior. This material behavior defines what the elements in the part are allowed to do and what their initial conditions are. The initial conditions within a part can change as long as the degrees of freedom are specified. The process within a part can be simulated individually and then later assembled with other parts through the use of contact constraints which define the behavior of the parts at the location where they interact. A tie constraint should be used until the very last step in the model to ensure that each part is operating correctly before it is required to be assembled to other parts. The tie constraint links two parts or surfaces, with dissimilar meshes, such that there is no relative motion between them. Until each part operates correctly on its own, this constraint is advised; it will also speed model convergence during the initial stages of trial/error and testing.

Table 1a. ‘Parts’ and ‘steps’ to be used in ABAQUS for each of the two cases.

Case	Parts	Steps
1	Part 1: Silt, unsaturated, thermal expansion allowed Part 2: Sand, unsaturated, thermal expansion allowed Part 3: Silt, unsaturated, only mechanical deformation allowed Part 4: Sand, unsaturated, only mechanical deformation allowed Part 5: Silt, saturated, no thermal expansion or mechanical deformation allowed Part 6: Sand, saturated, no thermal expansion or mechanical deformation allowed Part 7: Pipe, rigid-element, no flow, heat, or deformation allowed	Step 1: Geostatic stress state Step 2: Temperature-pore pressure Step 3: Temperature-pore pressure displacement
2	Part 1: Silt, unsaturated, thermal expansion allowed Part 2: Sand, unsaturated, thermal expansion allowed Part 3: Silt, unsaturated, only mechanical deformation allowed Part 4: Sand, unsaturated, only mechanical deformation allowed Part 5: Silt, saturated, no thermal expansion or mechanical deformation allowed Part 6: Sand, saturated, no thermal expansion or mechanical deformation allowed Part 7: Pipe, rigid-element, no flow, heat, or deformation allowed Part 8: Pipe breakage region, rigid-element, flux boundary, no heat or deformation allowed	Step 1: Geostatic stress state Step 2: Temperature-pore pressure Step 3: Introduce part 8 Step 4: Temperature-pore pressure displacement
3	Part 1: Gravel, unsaturated, T < 0℃ (initial frozen state), only thermal expansion allowed Part 2: Gravel, unsaturated, T > 0℃ (below freezing front), mechanical deformation allowed Part 3: Gravel, saturated, T > 0℃ (below water table), no expansion or deformation allowed Part 4: Pipe, rigid-element, no flow, heat, or deformation allowed	Step 1: Geostatic stress state Step 2: Infiltration event begins Step 3: Temperature-pore pressure Step 4: Temperature-pore pressure displacement

[Ł] A user subroutine will be required to implement the decision tree given in Figure 40, which will decide whether an element is exhibiting the material behaviors of thermal expansion or mechanical deformation.

[ł] Displacement (deformation) step only initiated when overburden pressure is exceeded. Thermal expansion processes are included in the 'Temperature-pore pressure' step.

Using the process described above, subroutines would be required to implement the decision tree given in Figure 3a, and to define the Segregation Potential (SP) model that will be used to estimate the expansion resultant from secondary frost heaving. Using the UEXPAN() routine, an SP model can be implemented into the overall thermal expansion calculation. Design of a subroutine for the decision tree will not be as straightforward as it is not available as an option in ABAQUS's predefined subroutines. However, this appears to be the most efficient way to induce the process of deformation below the freezing front. There are no existing empirical equations, which define the combined behavior of thermal expansion and stress-strain below the freezing front, therefore, approximating the frozen zone as overburden pressure in a standard soil deformation equation seems to be a reasonable solution. Provided that the modelling scheme described here is effective, laboratory testing (ie – column experiments) should be used to verify the results of the modelling.

Additionally, the geostatic stress state must be established for every analysis involving soil deformation as it accounts for the initial stresses, which are present in the domain before any subsequent deformation steps are initiated. The initial stresses have to be specified for two vertical coordinates (generally one at the top surface and one at the bottom surface). ABAQUS linearly interpolates the initial stress at all other nodes in the domain. This is the process that occurs during Step 1 (geostatic stress state) for all the cases listed in Table 1a. Initial stress at a point in a vertical plane can be obtained simply by multiplying the bulk soil density, the gravitational constant, and the depth below the surface in the vertical plane. Since soil bulk density varies with water content, geostatic stress states can be established for different conditions of saturation within the domain, then interpolate linearly within them. This would require more parts, but would yield a more accurate geostatic stress state.

Suggested input and discretization parameters for the modelling in ABAQUS were tabulated from previous works and are given in Appendix B.

A.6 Conclusions

The problem of pipe and water main damage in Southern Ontario during the winter is hypothesized to be caused by differential stress created by the uneven freezing of soil above the pipe/main. This problem is unique from other incidences of differential freezing and stress because the pipes and mains in this region are not encompassed by the freezing front. So, rather than examine the effect of frost heave in the upward direction, as is common, this study proposes the numerical investigation of frost heave in the downward direction. This may be a means to explain the damage of pipes and mains during the winter. In this thesis, two specific cases of differential freezing and stress are conceptualized and described mathematically. Recommendations for a strategy to model the conceptual cases numerically in ABAQUS are also given. Following the modelling of the proposed cases, the results should be verified using laboratory and/or in-situ methods to compare to the results of the modelling.

Appendix B: Parameters for Modelling Environment in ABAQUS

PARAMETER	VALUE
Fluid properties	
Latent heat of fusion	334000 J/kg
Fluid specific heat	4182 J/kg C
Fluid conductivity	0.6 J/s m C
Ice specific heat	2108 J/kg C
Ice conductivity	2.14 J/s m C
Fluid compressibility	Incompressible
Density of ice	920 kg/m^3
Density of water	1000 kg/m^3
Thermal expansion coefficient of water	Non-linear and variable with temperature, see below
Soil properties	
Porosity of sand*; dry density of sand	0.3; 1800 kg/m3
Porosity of clay*; dry density of clay	0.4; 1600 kg/m3
Soil grain specific heat	1380 J/kg C
Thermal conductivity	2.0 J/s m C
Saturated permeability of sand; clay**	1.0 Darcy; 10^{-3} Darcy
Unsaturated permeability function (permeability (K) as a function of saturation (s))	$K(s) = s^3$
Sorption (adsorption/exsorption) function	Tabular function of saturation between 0 and 1
Mechanical properties	
Poisson's ratio	0.3
Thawed Elastic (Young's) modulus for sand; clay	1.03421×10^7 Pa; 6.89476×10^5 Pa
Frozen Elastic (Young's) modulus	1.03421×10^{11} Pa
Thermal expansion coefficient for sand; clay	5.60×10^{-6} C; 9.67×10^{-6} C

Domain properties	
Length of domain in x, y, z	50m, 3m, 1m
Initial domain temperature	5°C everywhere
Porous media element type (in ABAQUS)	Reduced integration fully-coupled temperature pore pressure displacement (C3D8RPT)

** Porosity is considered as a void ratio equal to 'porosity/porosity-1'*

*** 1 Darcy = 9.87 × 10-^{9} cm^{2}*

Table 1b. Summary of input parameters. Parameters 1-7 are given by MacKenzie et al. (2007). Other properties are given by Fetter (2014), and Abaqus Example Problem 10.16.

Appendix C.1 Tabulated Results of Icing Distributions for CMV using Landsat Data

Year	Anomaly Strength	Number of Discrete Icings	Area Covered by Icings (m^2)	Average Icing Size (m^2)	Percent of Total Icings by Area (%)	Volume of Icings (m^3)
2016	-4	60	276075	4601	0.8	818447
	-3	736	7212081	9799	20.5	28678556
	-2	1586	8242315	5196	23.5	33171482
	-1	2376	11714909	4930	33.3	48662751
	1	1475	4652899	3154	13.2	17786479
	2	569	2625047	4613	7.5	9530828
	3	106	367403	3466	1.0	1117575
	4	12	48305	4025	0.1	122412
Total	-	6920	**35139034**	-	100.0	**161132125**
2009	-4	28	29494	1053	0.1	71496
	-3	201	624929	3109	1.8	1994007
	-2	516	1726297	3345	5.0	6035693
	-1	2547	11936721	4686	34.3	49667915
	1	1939	18119014	9344	52.1	78277673
	2	437	1689861	3886	4.9	5896968
	3	284	450596	1586	1.3	1396045
	4	25	223883	8995	0.6	651320
Total		5977	**34800795**	-	100.0	**159442253**
2004	-4	5	3774	754	0.0	7603
	-3	24	73283	3053	0.2	192808
	-2	357	1888427	5289	5.8	6656109
	-1	4363	18086416	4145	55.1	78124181
	1	2432	9081474	3734	27.7	36869025
	2	538	1700146	3160	5.2	5936100
	3	109	673861	6182	2.1	2164776
	4	44	1303039	29614	4.0	4441962
Total	-	7872	**32810420**	-	100.0	**149528537**

Table 1c. Results of the Icing distribution within thermal anomalies analysis for Landsat 4-5 TM and Landsat 8-OLI data for years 2004, 2009, and 2016.

Appendix C.2 Tabulated Results of Chi-Squared Test of Icings in the CMV

Year Combination	Anomaly Strength	# of Icings in 2016	# of Icings in 2009	Proportion of Icings in 2009	Expected Number of Icings in 2016	X^2 (Test statistic)
2016/2009	-4	60	28	0.004684624	32	23.5
	-3	736	201	0.033628911	233	1088.5
	-2	1586	516	0.086330935	597	1635.9
	-1	2376	2547	0.426133512	2949	111.3
	1	1475	1939	0.324410239	2245	264.1
	2	569	437	0.073113602	506	7.9
	3	106	284	0.047515476	329	151.0
	4	12	25	0.0041827	29	9.9
Total	-	6920	5977	1	6920	**3291.9**

Table 2c. Chi Squared Test comparing the number of icings in 2016 to the number of icings 2009 (Critical value = 14.07)

Year Combination	Anomaly Strength	# of Icings in 2009	# of Icings in 2004	Proportion of Icings in 2004	Expected Number of Icings in 2009	X^2 (Test statistic)
2009/2004	-4	28	5	0.000635163	4	154.3
	-3	201	24	0.00304878	18	1833.3
	-2	516	357	0.04535061	271	221.3
	-1	2547	4363	0.554242886	3313	177.0
	1	1939	2432	0.308943089	1847	4.6
	2	437	538	0.068343496	408	2.0
	3	284	109	0.013846545	83	489.3
	4	25	44	0.005589431	33	2.1
Total	-	5977	7872	1	5977	**2884.0**

Table 3c. Chi Squared Test comparing the number of icings in 2009 to the number of icings 2004 (Critical value = 14.07)

Year Combination	Anomaly Strength	Area of Icings 2016 (m^2)	Area of Icings 2009 (m^2)	Proportion of Area 2009	Expected Icing Area in 2016 (m^2)	X^2 (Test statistic)
2016/2009	-4	276075	29494	0.000847509	29781	2036922.6
	-3	7212081	624929	0.01795732	631003	68637706.3
	-2	8242315	1726297	0.049605102	1743075	24233097.5
	-1	11714909	11936721	0.343001388	12052737	9469.1
	1	4652899	18119014	0.520649428	18295118	10172666.7
	2	2625047	1689861	0.048558115	1706285	494714.0
	3	367403	450596	0.012947865	454975	16855.7
	4	48305	223883	0.006433273	226059	139770.9
Total	-	35139034	34800795	1	35139034	**105741202.9**

Table 4c. Chi Squared Test comparing the area of icings in 2016 to the area of icings 2009 (Critical value = 14.07)

Year Combination	Anomaly Strength	Area of Icings 2009 (m^2)	Area of Icings 2004 (m^2)	Proportion of Area 2004	Expected Icing Area in 2009 (m^2)	X^2 (Test statistic)
2009/2004	-4	29494	3774	0.000115024	4003	162329.1
	-3	624929	73283	0.002233528	77729	3852230.5
	-2	1726297	1888427	0.057555709	2002984	38220.9
	-1	11936721	18086416	0.551240002	19183590	2737606.2
	1	18119014	9081474	0.276786277	9632382	7477165.1
	2	1689861	1700146	0.051817258	1803282	7133.8
	3	450596	673861	0.020538018	714739	97618.4
	4	223883	1303039	0.039714182	1382085	970585.8
Total	-	34800795	32810420	1	34800795	**15342889.8**

Table 5c. Chi Squared Test comparing the area of icings in 2009 to the area of icings 2004 (Critical value = 14.07)

Appendix C.3 Tabulated Results of Kolmogorov-Smirnov Normality Test for Temp. Distribution Subsets

										Sum
Value °C (x)	-23.7	-23.6	-23.5	-23.4	-23.3	-23.2	-23.1	-23	-22.9	-
Frequency (f)	2	6	8	9	23	23	11	16	2	100
fx	-47.4	-141.6	-188	-210.6	-535.9	-533.6	-254.1	-368	-45.8	-2325

x	f	Cumulative	Sn(x)	Z-score	f(x)	Difference between Sn(x) and f(x)
-23.7	2	2	0.02	-2.49248	0.006343	0.01365728
-23.6	6	8	0.08	-1.9386	0.026275	0.05372472
-23.5	8	16	0.16	-1.38471	0.08307	0.07692963
-23.4	9	25	0.25	-0.83083	0.203036	0.04696426
-23.3	23	48	0.48	-0.27694	0.390912	0.08908778
-23.2	23	71	0.71	0.276942	0.609088	**0.10091222**
-23.1	11	82	0.82	0.830827	0.796964	0.02303574
-23	16	98	0.98	1.384711	0.91693	0.06307037
-22.9	2	100	1	1.938596	0.973725	0.02627528

Dn Max	0.1009122
Dn, α	0.136
α	0.05

Metric	Excel Function
Sn(x)	Cumulative Frequency / # of Observations
Z-Score	STANDARDIZE (x, mean, std. dev.)
F(x)	NORMDIST (x, mean, std. dev., TRUE)

Table 6c. Data and results of KS Normality Test for the 2016 Temperature Distribution Subset.

									Sum
Value °C (x)	-30	-29	-28	-27	-26	-25	-24	-23	-
Frequency (f)	3	8	12	25	28	16	5	3	100
fx	-90	-232	-336	-675	-728	-400	-120	-69	-2650

x	**f**	**Cumulative**	**Sn(x)**	**Z-score**	**f(x)**	**Difference between Sn(x) and f(x)**
-30	3	3	0.03	-2.30283	0.010644	0.01935582
-29	8	11	0.11	-1.64488	0.049997	0.06000264
-28	12	23	0.23	-0.98693	0.161839	0.06816092
-27	25	48	0.48	-0.32898	0.371087	0.10891303
-26	28	76	0.76	0.32898	0.628913	**0.13108697**
-25	16	92	0.92	0.98693	0.838161	0.08183908
-24	5	97	0.97	1.64488	0.950003	0.01999736
-23	3	100	1	2.30283	0.989356	0.01064418

Dn Max	0.13108697
Dn, α	0.136
α	0.05

Metric	**Excel Function**
Sn(x)	Cumulative Frequency / # of Observations
Z-Score	STANDARDIZE (x, mean, std. dev.)
F(x)	NORMDIST (x, mean, std. dev., TRUE)

Table 7c. Data and results of KS Normality Test for the 2009 Temperature Distribution Subset.

									Sum
Value °C (x)	-3	-2	-1	0	1	2	3	4	-
Frequency (f)	9	9	17	29	21	10	3	2	100
fx	-27	-18	-17	0	21	20	9	8	-4

x	**f**	**Cumulative**	**Sn(x)**	**Z-score**	**f(x)**	**Difference between Sn(x) and f(x)**
-3	9	9	0.09	-1.85785	0.031594845	0.058405155
-2	9	18	0.18	-1.23020	0.109310941	0.070689059
-1	17	35	0.35	-0.60255	0.273404917	0.076595083
0	29	64	0.64	0.02511	0.510014849	**0.129985151**
1	21	85	0.85	0.65276	0.743044384	0.106955616
2	10	95	0.95	1.28041	0.89980007	0.05019993
3	3	98	0.98	1.28041	0.89980007	0.08019993
4	2	100	1	2.53572	0.994389183	0.005610817

Dn Max	0.129985151
Dn, α	0.136
α	0.05

Metric	**Excel Function**
Sn(x)	Cumulative Frequency / # of Observations
Z-Score	STANDARDIZE (x, mean, std. dev.)
F(x)	NORMDIST (x, mean, std. dev., TRUE)

Table 8c. Data and results of KS Normality Test for the 2004 Temperature Distribution Subset.

Appendix C.4 Attribute Tables for Icings in Bogg Creek Watershed (2004)

Icing ID	Area (sq. m)	Icing ID	Area (sq. m)	Icing ID	Area (sq. m)
0	165.8274391	42	634.7903912	84	234.3800541
1	157.5199655	43	6.612449072	85	1686.367727
2	25.67080548	44	616.2222863	86	576.3427734
3	91.60546068	45	0.236599852	87	233.0037224
4	64.48930285	46	144.6160564	88	616.2222862
5	616.2222863	47	279.7690755	89	3164.71871
6	142.4257663	48	165.8160172	90	10.06839926
7	448.098644	49	1208.811474	91	41944.56111
8	4.998676126	50	148.2385056	92	6126.712229
9	77.55123768	51	329.8872311	93	616.2222862
10	190.681969	52	86.7752795	94	616.2222862
11	3207.872908	53	583.2356551	95	2476.052705
12	954.7337995	54	137.079013	96	2131.864452
13	277.3647237	55	313.1324565	97	617.8966267
14	42.29460079	56	17.33117688	98	5561.146904
15	189.1228055	57	4032.550694	99	12.40887062
16	58.32434833	58	5263.721645	100	104.2400852
17	1451.238585	59	299.9938316	101	2106.436384
18	21.9456049	60	1.477380148	102	21.29196273
19	34.16197263	61	54.09643005	103	1.276188054
20	164.4476549	62	136.756913	104	706.0227641
21	1362.182792	63	4.274574906	105	285.2463556
22	153.5209306	64	8.225671208	106	118.1283591
23	241.8738182	65	134.7139648	107	445.7619679
24	350.2223928	66	9.339250945	108	98.68444009
25	19.88440458	67	139.1128303	109	86.57215652
26	209.5634693	68	36.69813378	110	39.06686473
27	599.9276759	69	85.03283743	111	32.18310123
28	1920.724946	70	2.278048701		
29	16.21392293	71	235.345438		
30	171.7317161	72	189.7885452		
31	9.380218265	73	762.2032246		
32	14344.59824	74	18.40990603		
33	0.00499888	75	797.6022489		
34	9.483674143	76	877.0446428		
35	359.4922551	77	7474.04647		
36	193.8879225	78	343.7943088		
37	541.3141298	79	2225.993216		
38	2910.135327	80	20.83932578		
39	14.89216088	81	0.181903244		
40	11.52506727	82	376.3601323		
41	158.5695088	83	121.6404251		

(2009)

Icing ID	Area (sq. m)	Icing ID	Area (sq. m)	Icing ID	Area (sq. m)
0	165.8274391	42	266.7826641	84	1213.230955
1	88.10396476	43	86.77527955	85	343.794309
2	157.5199655	44	32.72526814	86	616.2222862
3	59.87223788	45	137.079013	87	616.2222862
4	25.67080544	46	313.1324565	88	1.725671503
5	149.6121225	47	596.6367447	89	24.50565074
6	91.60546069	48	900	90	570.5979697
7	64.48930285	49	1356.207493	91	1362.7105
8	83.03954609	50	616.2222862	92	616.2222862
9	19.4242581	51	554.9328019	93	233.0037224
10	96.57882274	52	1.477380147	94	6555.360989
11	4.998676126	53	136.756913	95	647.6891444
12	1.291584744	54	4.274574907	96	50859.94806
13	190.6819691	55	0.127833865	97	1250.505698
14	901.900277	56	0.001563686	98	556.9638977
15	1417.606195	57	42.87023392	99	304.3037125
16	189.1228055	58	616.2222863	100	156.9814715
17	2.641578852	59	11.62250844	101	274.2313286
18	58.32434832	60	36.69813376	102	1893.62577
19	164.4476548	61	1476.342773	103	5561.146904
20	280.7270771	62	85.03283742	104	2106.436384
21	337.7236318	63	452.0456849	105	1.276188053
22	64.53448014	64	2.278048707	106	93.18934728
23	153.5209306	65	25.4313716	107	285.2463557
24	241.8738182	66	235.3454381	108	70.05621009
25	350.2223927	67	189.7885452	109	75.28280847
26	19.88440459	68	762.2032246	110	147.7543597
27	209.5634693	69	616.2222862	111	3.130154075
28	599.927676	70	616.2222862		
29	1920.724946	71	616.2222862		
30	568.3898199	72	616.2222863		
31	9.380218273	73	1152.685547		
32	10262.82681	74	616.2222862		
33	1542.290168	75	616.2222862		
34	2333.792554	76	616.2222863		
35	14.89216087	77	149.0781395		
36	11.52506728	78	18.40990602		
37	158.5695088	79	184.434468		
38	0.959931547	80	0.016728737		
39	39.24861795	81	223.6785447		
40	634.7903912	82	217.6693325		
41	0.236599852	83	7474.04647		

(2016)

Icing ID	Area (sq. m)	Icing ID	Area (sq. m)
0	0.30248126	42	102.2107147
1	5005.371094	43	616.2222863
2	57.08450664	44	616.2222862
3	7799.993708	45	5.972574825
4	95.63774771	46	616.2222862
5	0.305773193	47	0.353109479
6	28.98895572	48	24.01347468
7	616.2222862	49	4489.892578
8	0.316218186	50	589.2089137
9	45.24005245	51	35.43790761
10	0.840863738	52	2447.477297
11	616.2222862	53	0.162078045
12	0.071387279	54	2.348696837
13	361.5860524	55	1152.685547
14	550.827701	56	2052.685547
15	193.6124166	57	616.2222862
16	0.304250517	58	6.296125234
17	13.80328686	59	123.516879
18	102.2169588	60	316.8754398
19	3565.018846	61	616.2222862
20	67.55064818	62	1800
21	7797.927224	63	616.2222862
22	362.3010967	64	10.19394962
23	21.82746713	65	0.344196302
24	66.50402503		
25	1.318110626		
26	616.2222862		
27	8.85863768		
28	900		
29	34.67186638		
30	616.2222862		
31	24.40584053		
32	26.94681719		
33	2.426245895		
34	0.306848831		
35	616.2222862		
36	244.6754841		
37	77.73158647		
38	616.2222862		
39	0.25583454		
40	616.2222862		
41	6.031909801		

(2017)

Icing ID	Area (sq. m)	Icing ID	Area (sq. m)
0	42	42	4
1	4	43	42
2	4	44	27
3	1	45	720
4	22	46	17
5	8	47	162
6	6	48	9
7	1	49	9
8	45	50	32
9	20	51	77
10	9	52	151
11	9	53	0
12	20	54	91
13	9	55	7
14	28	56	9
15	1	57	12
16	21	58	9
17	3	59	18
18	33	60	9
19	8	61	9
20	0	62	9
21	49	63	3
22	22	64	9
23	3	65	18
24	2	66	4
25	6	67	9
26	6	68	6
27	1	69	141
28	27	70	3
29	2	71	3
30	49	72	2
31	6	73	6
32	8	74	18
33	1	75	27
34	9	76	9
35	178	77	673
36	235	78	18
37	108	79	9
38	6	80	716
39	18	81	6
40	42	82	675
41	4	83	48

Icing ID	Area (sq. m)	Icing ID	Area (sq. m)	Icing ID	Area (sq. m)
84	16	126	0	168	54
85	192	127	18	169	72
86	9	128	9	170	203
87	18	129	45	171	34
88	27	130	9		
89	9	131	9		
90	52	132	27		
91	18	133	18		
92	9	134	9		
93	18	135	0		
94	9	136	9		
95	62	137	2		
96	9	138	18		
97	27	139	0		
98	42	140	9		
99	27	141	18		
100	410	142	18		
101	27	143	81		
102	18	144	45		
103	2	145	36		
104	9	146	27		
105	9	147	18		
106	21	148	54		
107	0	149	9		
108	9	150	36		
109	18	151	9		
110	153	152	36		
111	54	153	9		
112	27	154	36		
113	9	155	9		
114	9	156	36		
115	1	157	18		
116	36	158	45		
117	15	159	9		
118	9	160	9		
119	18	161	9		
120	18	162	9		
121	266	163	18		
122	8	164	9		
123	27	165	9		
124	9	166	9		
125	9	167	9		

Table 9c. – Attribute table data showing all icings and their associated areas.

Appendix C.5 Tabulated Results of Vegetation Distribution NDVI Change

Year Combination	Change in NDVI	Pixel Count	Area (m^2)
2017/2016	(-0.001 to -0.05)	3026	75650
	(-0.05 to -0.1)	316	7900
	(-0.1 to -0.15)	46	1150
	(-0.15 to -0.2)	17	425
	(-0.2 to -0.25)	4	100
	(-0.25 to -0.3)	0	0
	(< -0.3)	0	0
2016/2014	(-0.001 to -0.05)	3097	77425
	(-0.05 to -0.1)	306	7650
	(-0.1 to -0.15)	17	425
	(-0.15 to -0.2)	7	175
	(-0.2 to -0.25)	0	0
	(-0.25 to -0.3)	1	25
	(< -0.3)	0	0
2014/2013	(-0.001 to -0.05)	2586	64650
	(-0.05 to -0.1)	1063	26575
	(-0.1 to -0.15)	100	2500
	(-0.15 to -0.2)	8	200
	(-0.2 to -0.25)	0	0
	(-0.25 to -0.3)	1	25
	(< -0.3)	0	0
2013/2012	(-0.001 to -0.05)	3020	75500
	(-0.05 to -0.1)	519	12975
	(-0.1 to -0.15)	25	625
	(-0.15 to -0.2)	2	50
	(-0.2 to -0.25)	0	0
	(-0.25 to -0.3)	0	0
	(< -0.3)	0	0

Table 10c. Distribution of NDVI change for each year combination, given by pixel count and by area (pixel count * 25 sq. m).

Appendix C.6 Data and Results from Chi-Squared Analysis for Consecutive NDVI Change

Year Combination	NDVI Change	Area Δ in 2017 - 2016 (m^2)	2017 - 2016 as a proportion	Area Δ in 2016 - 2014 (m^2)	Expected Area Δ in 2017 - 2016 as a proportion	X^2 (Test statistic)
2017/2016 and 2016/2014	(-0.001 to -0.05)	75650	0.8877	77425	0.9034	0.0003
	(-0.05 to -0.1)	7900	0.0927	7650	0.0893	0.0001
	(-0.1 to -0.15)	1150	0.0135	425	0.0050	0.0147
	(-0.15 to -0.2)	425	0.0050	175	0.0020	0.0042
	(-0.2 to -0.25)	100	0.0012	0	0.0000	0.0000
	(-0.25 to -0.3)	0	0.0000	25	0.0003	0.0003
	(< -0.3)	0	0.0000	0	0.0000	0.0000
Total	-	85225	1	85700	1	**0.0196**

Table 11c. Results of Chi-squared test comparing NDVI Change as a proportion between the year combinations 2017/2016 and 2016/2014.

Year Combination	NDVI Change	Area Δ in 2016 - 2014 (m^2)	2016 – 2014 as a proportion	Area Δ in 2014 - 2013 (m^2)	Expected Area Δ in 2016 - 2014 as a proportion	X^2 (Test statistic)
2016/2014 and 2014/2013	(-0.001 to -0.05)	77425	0.9034	64650	0.6881	0.0674
	(-0.05 to -0.1)	7650	0.0893	26575	0.2829	0.1325
	(-0.1 to -0.15)	425	0.0050	2500	0.0266	0.0176
	(-0.15 to -0.2)	175	0.0020	200	0.0021	0.0000
	(-0.2 to -0.25)	0	0.0000	0	0.0000	0.0000
	(-0.25 to -0.3)	25	0.0003	25	0.0003	0.0000
	(< -0.3)	0	0.0000	0	0.0000	0.0000
Total	-	85700	1.0000	93950	1.0000	**0.2175**

Table 12c. Results of Chi-squared test comparing NDVI Change as a proportion between the year combinations 2016/2014 and 2014/2013.

Year Combination	NDVI Change	Area Δ in 2014 – 2013 (m^2)	2014 – 2013 as a proportion	Area Δ in 2013 - 2012 (m^2)	Expected Area Δ in 2013 - 2012 as a proportion	X^2 (Test statistic)
2014/2013 and 2013/2012	(-0.001 to -0.05)	77425	0.6881	75500	0.8469	0.0298
	(-0.05 to -0.1)	7650	0.2829	12975	0.1455	0.1296
	(-0.1 to -0.15)	425	0.0266	625	0.0070	0.0548
	(-0.15 to -0.2)	175	0.0021	50	0.0006	0.0044
	(-0.2 to -0.25)	0	0.0000	0	0.0000	0.0000
	(-0.25 to -0.3)	25	0.0003	0	0.0000	0.0000
	(< -0.3)	0	0.0000	0	0.0000	0.0000
Total	-	85700	1.0000	89150	1.0000	**0.2185**

Table 13c. Results of Chi-squared test comparing NDVI Change as a proportion between the year combinations 2014/2013 and 2013/2012.

Appendix C.7 Data Used to Construct Histograms for Image Algorithms and Temperature Distributions

Index	Text	Vertical Bar
0	0.10415720473974943 - 0.10653202000958117	19
1	0.10653202000958117 - 0.10890683527941292	18
2	0.10890683527941292 - 0.11128165054924466	15
3	0.11128165054924466 - 0.1136564658190764	18
4	0.1136564658190764 - 0.11603128108890814	21
5	0.11603128108890814 - 0.11840609635873989	23
6	0.11840609635873989 - 0.12078091162857163	23
7	0.12078091162857163 - 0.12315572689840337	22
8	0.12315572689840337 - 0.12553054216823512	25
9	0.12553054216823512 - 0.12790535743806686	13
10	0.12790535743806686 - 0.1302801727078986	30
11	0.1302801727078986 - 0.13265498797773034	27
12	0.13265498797773034 - 0.13502980324756209	14
13	0.13502980324756209 - 0.13740461851739383	19
14	0.13740461851739383 - 0.13977943378722557	29
15	0.13977943378722557 - 0.14215424905705731	19
16	0.14215424905705731 - 0.14452906432688906	21
17	0.14452906432688906 - 0.1469038795967208	31
18	0.1469038795967208 - 0.14927869486655254	28
19	0.14927869486655254 - 0.15165351013638428	24
20	0.15165351013638428 - 0.15402832540621603	30
21	0.15402832540621603 - 0.15640314067604777	20
22	0.15640314067604777 - 0.15877795594587951	26
23	0.15877795594587951 - 0.16115277121571125	19
24	0.16115277121571125 - 0.163527586485543	23
25	0.163527586485543 - 0.16590240175537474	33
26	0.16590240175537474 - 0.16827721702520648	14
27	0.16827721702520648 - 0.17065203229503823	30
28	0.17065203229503823 - 0.17302684756486997	29
29	0.17302684756486997 - 0.17540166283470171	36
30	0.17540166283470171 - 0.17777647810453345	35
31	0.17777647810453345 - 0.1801512933743652	33
32	0.1801512933743652 - 0.18252610864419694	22
33	0.18252610864419694 - 0.18490092391402868	35
34	0.18490092391402868 - 0.18727573918386042	25
35	0.18727573918386042 - 0.18965055445369217	37
36	0.18965055445369217 - 0.19202536972352391	26
37	0.19202536972352391 - 0.19440018499335565	39
38	0.19440018499335565 - 0.19677500026318739	35
39	0.19677500026318739 - 0.19914981553301914	32
40	0.19914981553301914 - 0.20152463080285088	28
41	0.20152463080285088 - 0.20389944607268262	26
42	0.20389944607268262 - 0.20627426134251436	30
43	0.20627426134251436 - 0.20864907661234611	34
44	0.20864907661234611 - 0.21102389188217785	34
45	0.21102389188217785 - 0.21339870715200959	40
46	0.21339870715200959 - 0.21577352242184134	40
47	0.21577352242184134 - 0.21814833769167308	43
48	0.21814833769167308 - 0.22052315296150482	34
49	0.22052315296150482 - 0.22289796823133656	36
50	0.22289796823133656 - 0.22527278350116831	54
51	0.22527278350116831 - 0.22764759877100005	42
52	0.22764759877100005 - 0.23002241404083179	41

```
53    0.23002241404083179 - 0.23239722931066353 60
54    0.23239722931066353 - 0.23477204458049528 41
55    0.23477204458049528 - 0.23714685985032702 49
56    0.23714685985032702 - 0.23952167512015876 57
57    0.23952167512015876 - 0.2418964903899905  47
58    0.2418964903899905 - 0.24427130565982225  43
59    0.24427130565982225 - 0.24664612092965399 65
60    0.24664612092965399 - 0.24902093619948573 62
61    0.24902093619948573 - 0.25139575146931747 43
62    0.25139575146931747 - 0.25377056673914922 61
63    0.25377056673914922 - 0.25614538200898096 53
64    0.25614538200898096 - 0.2585201972788127  59
65    0.2585201972788127 - 0.26089501254864444  47
66    0.26089501254864444 - 0.26326982781847619 81
67    0.26326982781847619 - 0.26564464308830793 67
68    0.26564464308830793 - 0.26801945835813967 71
69    0.26801945835813967 - 0.27039427362797142 72
70    0.27039427362797142 - 0.27276908889780316 80
71    0.27276908889780316 - 0.2751439041676349  74
72    0.2751439041676349 - 0.27751871943746664  95
73    0.27751871943746664 - 0.27989353470729839 88
74    0.27989353470729839 - 0.28226834997713013 96
75    0.28226834997713013 - 0.28464316524696187 119
76    0.28464316524696187 - 0.28701798051679361 100
77    0.28701798051679361 - 0.28939279578662536 100
78    0.28939279578662536 - 0.2917676110564571  109
79    0.2917676110564571 - 0.29414242632628884  115
80    0.29414242632628884 - 0.29651724159612058 130
81    0.29651724159612058 - 0.29889205686595233 149
82    0.29889205686595233 - 0.30126687213578407 148
83    0.30126687213578407 - 0.30364168740561581 148
84    0.30364168740561581 - 0.30601650267544755 162
85    0.30601650267544755 - 0.3083913179452793  184
86    0.3083913179452793 - 0.31076613321511104  193
87    0.31076613321511104 - 0.31314094848494278 190
88    0.31314094848494278 - 0.31551576375477453 193
89    0.31551576375477453 - 0.31789057902460627 231
90    0.31789057902460627 - 0.32026539429443801 239
91    0.32026539429443801 - 0.32264020956426975 254
92    0.32264020956426975 - 0.3250150248341015  284
93    0.3250150248341015 - 0.32738984010393324  286
94    0.32738984010393324 - 0.32976465537376498 297
95    0.32976465537376498 - 0.33213947064359672 323
96    0.33213947064359672 - 0.33451428591342847 345
97    0.33451428591342847 - 0.33688910118326021 344
98    0.33688910118326021 - 0.33926391645309195 401
99    0.33926391645309195 - 0.34163873172292369 410
100   0.34163873172292369 - 0.34401354699275544 445
101   0.34401354699275544 - 0.34638836226258718 477
102   0.34638836226258718 - 0.34876317753241892 482
103   0.34876317753241892 - 0.35113799280225066 548
104   0.35113799280225066 - 0.35351280807208241 572
105   0.35351280807208241 - 0.35588762334191415 596
106   0.35588762334191415 - 0.35826243861174589 606
107   0.35826243861174589 - 0.36063725388157764 663
108   0.36063725388157764 - 0.36301206915140938 667
109   0.36301206915140938 - 0.36538688442124112 757
```

110 0.36538688442124112 - 0.36776169969107286 806
111 0.36776169969107286 - 0.37013651496090461 830
112 0.37013651496090461 - 0.37251133023073635 835
113 0.37251133023073635 - 0.37488614550056809 924
114 0.37488614550056809 - 0.37726096077039983 993
115 0.37726096077039983 - 0.37963577604023158 1041
116 0.37963577604023158 - 0.38201059131006332 1119
117 0.38201059131006332 - 0.38438540657989506 1199
118 0.38438540657989506 - 0.3867602218497268 1237
119 0.3867602218497268 - 0.38913503711955855 1305
120 0.38913503711955855 - 0.39150985238939029 1365
121 0.39150985238939029 - 0.39388466765922203 1387
122 0.39388466765922203 - 0.39625948292905377 1474
123 0.39625948292905377 - 0.39863429819888552 1553
124 0.39863429819888552 - 0.40100911346871726 1646
125 0.40100911346871726 - 0.4033839928738549 1655
126 0.4033839928738549 - 0.40575874400838075 1754
127 0.40575874400838075 - 0.40813355927821249 1757
128 0.40813355927821249 - 0.41050837454804423 1903
129 0.41050837454804423 - 0.41288318981787597 1954
130 0.41288318981787597 - 0.41525800508770772 2081
131 0.41525800508770772 - 0.41763282035753946 2022
132 0.41763282035753946 - 0.4200076356273712 2135
133 0.4200076356273712 - 0.42238245089720294 2113
134 0.42238245089720294 - 0.42475726616703469 2166
135 0.42475726616703469 - 0.42713208143686643 2204
136 0.42713208143686643 - 0.42950689670669817 2383
137 0.42950689670669817 - 0.43188171197652991 2512
138 0.43188171197652991 - 0.43425652724636166 2573
139 0.43425652724636166 - 0.4366313425161934 2558
140 0.4366313425161934 - 0.43900615778602514 2526
141 0.43900615778602514 - 0.44138097305585688 2710
142 0.44138097305585688 - 0.44375578832568863 2762
143 0.44375578832568863 - 0.44613060359552037 2787
144 0.44613060359552037 - 0.44850541886535211 2806
145 0.44850541886535211 - 0.45088023413518385 2858
146 0.45088023413518385 - 0.4532550494050156 2901
147 0.4532550494050156 - 0.45562986467484734 3005
148 0.45562986467484734 - 0.45800467994467908 3043
149 0.45800467994467908 - 0.46037949521451083 3020
150 0.46037949521451083 - 0.46275431048434257 3108
151 0.46275431048434257 - 0.46512912575417431 3051
152 0.46512912575417431 - 0.46750394102400605 2995
153 0.46750394102400605 - 0.4698787562938378 3164
154 0.4698787562938378 - 0.47225357156366954 3131
155 0.47225357156366954 - 0.47462838683350128 3075
156 0.47462838683350128 - 0.47700320210333302 3116
157 0.47700320210333302 - 0.47937801737316477 3186
158 0.47937801737316477 - 0.48175283264299651 3013
159 0.48175283264299651 - 0.48412764791282825 3131
160 0.48412764791282825 - 0.48650246318265999 3054
161 0.48650246318265999 - 0.48887727845249174 3035
162 0.48887727845249174 - 0.49125209372232348 3141
163 0.49125209372232348 - 0.49362690899215522 3048
164 0.49362690899215522 - 0.49600172426198696 2901
165 0.49600172426198696 - 0.49837653953181871 3014
166 0.49837653953181871 - 0.50075135480165045 2914

167 0.50075135480165045 - 0.50312617007148219 2877
168 0.50312617007148219 - 0.50550098534131394 2830
169 0.50550098534131394 - 0.50787580061114568 2840
170 0.50787580061114568 - 0.51025061588097742 2697
171 0.51025061588097742 - 0.51262543115080916 2691
172 0.51262543115080916 - 0.51500024642064091 2680
173 0.51500024642064091 - 0.51737506169047265 2624
174 0.51737506169047265 - 0.51974987696030439 2631
175 0.51974987696030439 - 0.52212469223013613 2479
176 0.52212469223013613 - 0.52449950749996788 2393
177 0.52449950749996788 - 0.52687432276979962 2398
178 0.52687432276979962 - 0.52924913803963136 2286
179 0.52924913803963136 - 0.5316239533094631 2282
180 0.5316239533094631 - 0.53399876857929485 2138
181 0.53399876857929485 - 0.53637358384912659 2104
182 0.53637358384912659 - 0.53874839911895833 2086
183 0.53874839911895833 - 0.54112321438879007 1920
184 0.54112321438879007 - 0.54349802965862182 1900
185 0.54349802965862182 - 0.54587284492845356 1925
186 0.54587284492845356 - 0.5482476601982853 1769
187 0.5482476601982853 - 0.55062247546811705 1813
188 0.55062247546811705 - 0.55299729073794879 1758
189 0.55299729073794879 - 0.55537210600778053 1568
190 0.55537210600778053 - 0.55774692127761227 1625
191 0.55774692127761227 - 0.56012173654744402 1556
192 0.56012173654744402 - 0.56249655181727576 1415
193 0.56249655181727576 - 0.5648713670871075 1471
194 0.5648713670871075 - 0.56724618235693924 1423
195 0.56724618235693924 - 0.56962099762677099 1376
196 0.56962099762677099 - 0.57199581289660273 1261
197 0.57199581289660273 - 0.57437062816643447 1183
198 0.57437062816643447 - 0.57674544343626621 1217
199 0.57674544343626621 - 0.57912025870609796 1234
200 0.57912025870609796 - 0.5814950739759297 1130
201 0.5814950739759297 - 0.58386988924576144 1089
202 0.58386988924576144 - 0.58624470451559318 1062
203 0.58624470451559318 - 0.58861951978542493 1005
204 0.58861951978542493 - 0.59099433505525667 977
205 0.59099433505525667 - 0.59336915032508841 924
206 0.59336915032508841 - 0.59574396559492016 894
207 0.59574396559492016 - 0.5981187808647519 857
208 0.5981187808647519 - 0.60049359613458364 842
209 0.60049359613458364 - 0.60286841140441538 830
210 0.60286841140441538 - 0.60524322667424713 798
211 0.60524322667424713 - 0.60761804194407887 771
212 0.60761804194407887 - 0.60999285721391061 743
213 0.60999285721391061 - 0.61236767248374235 722
214 0.61236767248374235 - 0.6147424877535741 676
215 0.6147424877535741 - 0.61711730302340584 678
216 0.61711730302340584 - 0.61949211829323758 666
217 0.61949211829323758 - 0.62186693356306932 614
218 0.62186693356306932 - 0.62424174883290107 643
219 0.62424174883290107 - 0.62661656410273281 557
220 0.62661656410273281 - 0.62899137937256455 561
221 0.62899137937256455 - 0.63136619464239629 551
222 0.63136619464239629 - 0.63374100991222804 560
223 0.63374100991222804 - 0.63611582518205978 555

```
224   0.63611582518205978 - 0.63849064045189152 542
225   0.63849064045189152 - 0.64086545572172327 494
226   0.64086545572172327 - 0.64324027099155501 507
227   0.64324027099155501 - 0.64561508626138675 454
228   0.64561508626138675 - 0.64798990153121849 477
229   0.64798990153121849 - 0.65036471680105024 460
230   0.65036471680105024 - 0.65273953207088198 424
231   0.65273953207088198 - 0.65511434734071372 454
232   0.65511434734071372 - 0.65748916261054546 456
233   0.65748916261054546 - 0.65986397788037721 417
234   0.65986397788037721 - 0.66223879315020895 366
235   0.66223879315020895 - 0.66461360842004069 377
236   0.66461360842004069 - 0.66698842368987243 337
237   0.66698842368987243 - 0.66936323895970418 306
238   0.66936323895970418 - 0.67173805422953592 310
239   0.67173805422953592 - 0.67411286949936766 298
240   0.67411286949936766 - 0.6764876847691994  308
241   0.6764876847691994 - 0.67886250003903115  304
242   0.67886250003903115 - 0.68123731530886289 281
243   0.68123731530886289 - 0.68361213057869463 278
244   0.68361213057869463 - 0.68598694584852637 227
245   0.68598694584852637 - 0.68836176111835812 236
246   0.68836176111835812 - 0.69073657638818986 221
247   0.69073657638818986 - 0.6931113916580216  217
248   0.6931113916580216 - 0.69548620692785335  186
249   0.69548620692785335 - 0.69786102219768509 167
250   0.69786102219768509 - 0.70023583746751683 184
251   0.70023583746751683 - 0.70261065273734857 172
252   0.70261065273734857 - 0.70498546800718032 133
253   0.70498546800718032 - 0.70736028327701206 131
254   0.70736028327701206 - 0.7097350985468438  138
255   0.7097350985468438 - 0.71210991381667554  143
```

Table 14c. Normalized Difference Vegetation Index Distribution used to construct categorical histogram for 2012.

```
Index     Text                                          Vertical Bar
0     -0.43098719930276275 - -0.42566173271006846     160
1     -0.42566173271006846 - -0.42033626611737418     191
2     -0.42033626611737418 - -0.4150107995246799      252
3     -0.4150107995246799 - -0.40968533293198561      339
4     -0.40968533293198561 - -0.40435986633929133     390
5     -0.40435986633929133 - -0.39903439974659705     471
6     -0.39903439974659705 - -0.39370893315390276     558
7     -0.39370893315390276 - -0.38838346656120848     727
8     -0.38838346656120848 - -0.3830579999685142      869
9     -0.3830579999685142 - -0.37773253337581991      947
10    -0.37773253337581991 - -0.37240706678312563     1122
11    -0.37240706678312563 - -0.36708160019043135     1236
12    -0.36708160019043135 - -0.36175613359773706     1416
13    -0.36175613359773706 - -0.35643066700504278     1520
14    -0.35643066700504278 - -0.35110520041234849     1635
15    -0.35110520041234849 - -0.34577973381965421     1701
16    -0.34577973381965421 - -0.34045426722695993     1761
17    -0.34045426722695993 - -0.33512880063426564     1900
18    -0.33512880063426564 - -0.32980333404157136     1933
```

19	-0.32980333404157136 - -0.32447786744887708	2063
20	-0.32447786744887708 - -0.31915240085618279	2169
21	-0.31915240085618279 - -0.31382693426348851	2258
22	-0.31382693426348851 - -0.30850146767079423	2351
23	-0.30850146767079423 - -0.30317600107809994	2381
24	-0.30317600107809994 - -0.29785053448540566	2431
25	-0.29785053448540566 - -0.29252506789271138	2507
26	-0.29252506789271138 - -0.28719960130001709	2736
27	-0.28719960130001709 - -0.28187413470732281	2842
28	-0.28187413470732281 - -0.27654866811462853	2994
29	-0.27654866811462853 - -0.27122320152193424	3105
30	-0.27122320152193424 - -0.26589773492923996	3338
31	-0.26589773492923996 - -0.26057226833654568	3567
32	-0.26057226833654568 - -0.25524680174385139	3628
33	-0.25524680174385139 - -0.24992133515115711	3671
34	-0.24992133515115711 - -0.24459586855846283	3796
35	-0.24459586855846283 - -0.23927040196576854	3932
36	-0.23927040196576854 - -0.23394493537307426	4003
37	-0.23394493537307426 - -0.22861946878037998	4045
38	-0.22861946878037998 - -0.22329400218768569	3919
39	-0.22329400218768569 - -0.21796853559499141	4050
40	-0.21796853559499141 - -0.21264306900229712	3953
41	-0.21264306900229712 - -0.20731760240960284	3866
42	-0.20731760240960284 - -0.20199213581690856	3716
43	-0.20199213581690856 - -0.19666666922421427	3568
44	-0.19666666922421427 - -0.19134120263151999	3539
45	-0.19134120263151999 - -0.18601573603882571	3429
46	-0.18601573603882571 - -0.18069026944613142	3234
47	-0.18069026944613142 - -0.17536480285343714	3045
48	-0.17536480285343714 - -0.17003933626074286	2872
49	-0.17003933626074286 - -0.16471386966804857	2694
50	-0.16471386966804857 - -0.15938840307535429	2637
51	-0.15938840307535429 - -0.15406293648266001	2501
52	-0.15406293648266001 - -0.14873746988996572	2376
53	-0.14873746988996572 - -0.14341200329727144	2197
54	-0.14341200329727144 - -0.13808653670457716	2021
55	-0.13808653670457716 - -0.13276107011188287	1899
56	-0.13276107011188287 - -0.12743560351918859	1778
57	-0.12743560351918859 - -0.12211013692649431	1699
58	-0.12211013692649431 - -0.11678467033380002	1623
59	-0.11678467033380002 - -0.11145920374110574	1464
60	-0.11145920374110574 - -0.10613373714841146	1399
61	-0.10613373714841146 - -0.10080827055571717	1368
62	-0.10080827055571717 - -0.095482803963022889	1313
63	-0.095482803963022889 - -0.090157337370328605	1259
64	-0.090157337370328605 - -0.084831870777634322	1077
65	-0.084831870777634322 - -0.079506404184940038	1021
66	-0.079506404184940038 - -0.074180937592245755	1003
67	-0.074180937592245755 - -0.068855470999551471	908
68	-0.068855470999551471 - -0.063530004406857188	897
69	-0.063530004406857188 - -0.058204537814162904	864
70	-0.058204537814162904 - -0.052879071221468621	843
71	-0.052879071221468621 - -0.047553604628774337	761
72	-0.047553604628774337 - -0.042228138036080054	693
73	-0.042228138036080054 - -0.036902671443385771	686
74	-0.036902671443385771 - -0.031577204850691487	643
75	-0.031577204850691487 - -0.026251738257997204	665

76	-0.026251738257997204 - -0.02092627166530292	565
77	-0.02092627166530292 - -0.015600805072608637	554
78	-0.015600805072608637 - -0.010275338479914353	519
79	-0.010275338479914353 - -0.0049498718872200698	485
80	-0.0049498718872200698 - 0.00037555947054742137	471
81	0.00037555947054742137 - 0.0057010612981684972	465
82	0.0057010612981684972 - 0.011026527890862781	421
83	0.011026527890862781 - 0.016351994483557064	437
84	0.016351994483557064 - 0.021677461076251348	387
85	0.021677461076251348 - 0.027002927668945631	327
86	0.027002927668945631 - 0.032328394261639914	306
87	0.032328394261639914 - 0.037653860854334198	316
88	0.037653860854334198 - 0.042979327447028481	310
89	0.042979327447028481 - 0.048304794039722765	297
90	0.048304794039722765 - 0.053630260632417048	277
91	0.053630260632417048 - 0.058955727225111332	243
92	0.058955727225111332 - 0.064281193817805615	225
93	0.064281193817805615 - 0.069606660410499899	233
94	0.069606660410499899 - 0.074932127003194182	214
95	0.074932127003194182 - 0.080257593595888466	204
96	0.080257593595888466 - 0.085583060188582749	174
97	0.085583060188582749 - 0.090908526781277033	163
98	0.090908526781277033 - 0.096233993373971316	166
99	0.096233993373971316 - 0.1015594599666656	163
100	0.1015594599666656 - 0.10688492655935988	141
101	0.10688492655935988 - 0.11221039315205417	148
102	0.11221039315205417 - 0.11753585974474845	139
103	0.11753585974474845 - 0.12286132633744273	135
104	0.12286132633744273 - 0.12818679293013702	119
105	0.12818679293013702 - 0.1335122595228313	120
106	0.1335122595228313 - 0.13883772611552558	101
107	0.13883772611552558 - 0.14416319270821987	106
108	0.14416319270821987 - 0.14948865930091415	110
109	0.14948865930091415 - 0.15481412589360843	91
110	0.15481412589360843 - 0.16013959248630272	114
111	0.16013959248630272 - 0.165465059078997	109
112	0.165465059078997 - 0.17079052567169128	87
113	0.17079052567169128 - 0.17611599226438557	90
114	0.17611599226438557 - 0.18144145885707985	100
115	0.18144145885707985 - 0.18676692544977413	80
116	0.18676692544977413 - 0.19209239204246842	72
117	0.19209239204246842 - 0.1974178586351627	69
118	0.1974178586351627 - 0.20274332522785699	69
119	0.20274332522785699 - 0.20806879182055127	67
120	0.20806879182055127 - 0.21339425841324555	63
121	0.21339425841324555 - 0.21871972500593984	67
122	0.21871972500593984 - 0.22404519159863412	73
123	0.22404519159863412 - 0.2293706581913284	70
124	0.2293706581913284 - 0.23469612478402269	63
125	0.23469612478402269 - 0.24002159137671697	64
126	0.24002159137671697 - 0.24534705796941125	65
127	0.24534705796941125 - 0.25067252456210554	55
128	0.25067252456210554 - 0.25599799115479982	55
129	0.25599799115479982 - 0.2613234577474941	55
130	0.2613234577474941 - 0.26664892434018839	67
131	0.26664892434018839 - 0.27197439093288267	66
132	0.27197439093288267 - 0.27729985752557695	57

133 0.27729985752557695 - 0.28262532411827124 50
134 0.28262532411827124 - 0.28795079071096552 55
135 0.28795079071096552 - 0.2932762573036598 48
136 0.2932762573036598 - 0.29860172389635409 59
137 0.29860172389635409 - 0.30392719048904837 53
138 0.30392719048904837 - 0.30925265708174265 51
139 0.30925265708174265 - 0.31457812367443694 41
140 0.31457812367443694 - 0.31990359026713122 44
141 0.31990359026713122 - 0.3252290568598255 55
142 0.3252290568598255 - 0.33055452345251979 57
143 0.33055452345251979 - 0.33587999004521407 42
144 0.33587999004521407 - 0.34120545663790836 60
145 0.34120545663790836 - 0.34653092323060264 54
146 0.34653092323060264 - 0.35185638982329692 43
147 0.35185638982329692 - 0.35718185641599121 43
148 0.35718185641599121 - 0.36250732300868549 51
149 0.36250732300868549 - 0.36783278960137977 38
150 0.36783278960137977 - 0.37315825619407406 58
151 0.37315825619407406 - 0.37848372278676834 43
152 0.37848372278676834 - 0.38380918937946262 43
153 0.38380918937946262 - 0.38913465597215691 43
154 0.38913465597215691 - 0.39446012256485119 39
155 0.39446012256485119 - 0.39978558915754547 33
156 0.39978558915754547 - 0.40511105575023976 50
157 0.40511105575023976 - 0.41043652234293404 35
158 0.41043652234293404 - 0.41576198893562832 43
159 0.41576198893562832 - 0.42108745552832261 65
160 0.42108745552832261 - 0.42641292212101689 36
161 0.42641292212101689 - 0.43173838871371117 46
162 0.43173838871371117 - 0.43706385530640546 48
163 0.43706385530640546 - 0.44238932189909974 43
164 0.44238932189909974 - 0.44771478849179402 48
165 0.44771478849179402 - 0.45304025508448831 35
166 0.45304025508448831 - 0.45836572167718259 42
167 0.45836572167718259 - 0.46369118826987687 34
168 0.46369118826987687 - 0.46901665486257116 41
169 0.46901665486257116 - 0.47434212145526544 42
170 0.47434212145526544 - 0.47966758804795973 33
171 0.47966758804795973 - 0.48499305464065401 43
172 0.48499305464065401 - 0.49031852123334829 40
173 0.49031852123334829 - 0.49564398782604258 44
174 0.49564398782604258 - 0.50096945441873686 43
175 0.50096945441873686 - 0.50629492101143114 45
176 0.50629492101143114 - 0.51162038760412543 49
177 0.51162038760412543 - 0.51694585419681971 45
178 0.51694585419681971 - 0.52227132078951399 47
179 0.52227132078951399 - 0.52759678738220828 37
180 0.52759678738220828 - 0.53292225397490256 45
181 0.53292225397490256 - 0.53824772056759684 41
182 0.53824772056759684 - 0.54357318716029113 48
183 0.54357318716029113 - 0.54889865375298541 47
184 0.54889865375298541 - 0.55422412034567969 55
185 0.55422412034567969 - 0.55954958693837398 38
186 0.55954958693837398 - 0.56487505353106826 26
187 0.56487505353106826 - 0.57020052012376254 41
188 0.57020052012376254 - 0.57552598671645683 35
189 0.57552598671645683 - 0.58085145330915111 40

190 0.58085145330915111 - 0.58617691990184539 38
191 0.58617691990184539 - 0.59150238649453968 50
192 0.59150238649453968 - 0.59682785308723396 49
193 0.59682785308723396 - 0.60215331967992825 53
194 0.60215331967992825 - 0.60747878627262253 47
195 0.60747878627262253 - 0.61280425286531681 32
196 0.61280425286531681 - 0.6181297194580111 30
197 0.6181297194580111 - 0.62345518605070538 55
198 0.62345518605070538 - 0.62878065264339966 48
199 0.62878065264339966 - 0.63410611923609395 47
200 0.63410611923609395 - 0.63943158582878823 40
201 0.63943158582878823 - 0.64475705242148251 49
202 0.64475705242148251 - 0.6500825190141768 41
203 0.6500825190141768 - 0.65540798560687108 53
204 0.65540798560687108 - 0.66073345219956536 40
205 0.66073345219956536 - 0.66605891879225965 41
206 0.66605891879225965 - 0.67138438538495393 45
207 0.67138438538495393 - 0.67670985197764821 40
208 0.67670985197764821 - 0.6820353185703425 44
209 0.6820353185703425 - 0.68736078516303678 23
210 0.68736078516303678 - 0.69268625175573106 47
211 0.69268625175573106 - 0.69801171834842535 51
212 0.69801171834842535 - 0.70333718494111963 47
213 0.70333718494111963 - 0.70866265153381391 42
214 0.70866265153381391 - 0.7139881181265082 54
215 0.7139881181265082 - 0.71931358471920248 45
216 0.71931358471920248 - 0.72463905131189676 45
217 0.72463905131189676 - 0.72996451790459105 51
218 0.72996451790459105 - 0.73528998449728533 53
219 0.73528998449728533 - 0.74061545108997962 73
220 0.74061545108997962 - 0.7459409176826739 46
221 0.7459409176826739 - 0.75126638427536818 77
222 0.75126638427536818 - 0.75659185086806247 82
223 0.75659185086806247 - 0.76191731746075675 77
224 0.76191731746075675 - 0.76724278405345103 87
225 0.76724278405345103 - 0.77256825064614532 85
226 0.77256825064614532 - 0.7778937172388396 93
227 0.7778937172388396 - 0.78321918383153388 84
228 0.78321918383153388 - 0.78854465042422817 109
229 0.78854465042422817 - 0.79387011701692245 115
230 0.79387011701692245 - 0.79919558360961673 122
231 0.79919558360961673 - 0.80452105020231102 146
232 0.80452105020231102 - 0.8098465167950053 173
233 0.8098465167950053 - 0.81517198338769958 196
234 0.81517198338769958 - 0.82049744998039387 198
235 0.82049744998039387 - 0.82582291657308815 210
236 0.82582291657308815 - 0.83114838316578243 226
237 0.83114838316578243 - 0.83647384975847672 234
238 0.83647384975847672 - 0.841799316351171 223
239 0.841799316351171 - 0.84712478294386528 220
240 0.84712478294386528 - 0.85245024953655957 212
241 0.85245024953655957 - 0.85777571612925385 201
242 0.85777571612925385 - 0.86310118272194813 205
243 0.86310118272194813 - 0.86842664931464242 252
244 0.86842664931464242 - 0.8737521159073367 345
245 0.8737521159073367 - 0.87907758250003099 411
246 0.87907758250003099 - 0.88440304909272527 523

247	0.88440304909272527 - 0.88972851568541955	635
248	0.88972851568541955 - 0.89505398227811384	638
249	0.89505398227811384 - 0.90037944887080812	618
250	0.90037944887080812 - 0.9057049154635024	718
251	0.9057049154635024 - 0.91103038205619669	1044
252	0.91103038205619669 - 0.91635584864889097	1348
253	0.91635584864889097 - 0.92168131524158525	1550
254	0.92168131524158525 - 0.92700678183427954	1578
255	0.92700678183427954 - 0.93233224842697382	1029

Table 15c. Normalized Difference Snow Index Distribution used to construct categorical histogram for 2016.

Index	Text	Vertical Bar
0	46.515140533447273 - 53.378687388845727	27
1	53.378687388845727 - 60.24223424424418	431
2	60.24223424424418 - 67.105781099642627	1078
3	67.105781099642627 - 73.969327955041081	490
4	73.969327955041081 - 80.832874810439534	276
5	80.832874810439534 - 87.696421665837988	190
6	87.696421665837988 - 94.559968521236442	161
7	94.559968521236442 - 101.4235153766349	252
8	101.4235153766349 - 108.28706223203335	428
9	108.28706223203335 - 115.1506090874318	2598
10	115.1506090874318 - 122.01415594283026	3621
11	122.01415594283026 - 128.87770279822871	2060
12	128.87770279822871 - 135.74124965362716	537
13	135.74124965362716 - 142.60479650902562	307
14	142.60479650902562 - 149.46834336442407	213
15	149.46834336442407 - 156.33189021982253	146
16	156.33189021982253 - 163.19543707522098	145
17	163.19543707522098 - 170.05898393061943	110
18	170.05898393061943 - 176.92253078601789	101
19	176.92253078601789 - 183.78607764141634	104
20	183.78607764141634 - 190.64962449681479	93
21	190.64962449681479 - 197.51317135221325	79
22	197.51317135221325 - 204.3767182076117	76
23	204.3767182076117 - 211.24026506301016	87
24	211.24026506301016 - 218.10381191840861	68
25	218.10381191840861 - 224.96735877380706	65
26	224.96735877380706 - 231.83090562920552	79
27	231.83090562920552 - 238.69445248460397	78
28	238.69445248460397 - 245.55799934000243	63
29	245.55799934000243 - 252.42154619540088	50
30	252.42154619540088 - 259.28509305079933	67
31	259.28509305079933 - 266.14863990619779	67
32	266.14863990619779 - 273.01218676159624	51
33	273.01218676159624 - 279.87573361699469	54
34	279.87573361699469 - 286.73928047239315	60
35	286.73928047239315 - 293.6028273277916	65
36	293.6028273277916 - 300.46637418319006	61
37	300.46637418319006 - 307.32992103858851	43
38	307.32992103858851 - 314.19346789398696	52
39	314.19346789398696 - 321.05701474938542	44
40	321.05701474938542 - 327.92056160478387	51
41	327.92056160478387 - 334.78410846018232	54

42	334.78410846018232 - 341.64765531558078	42
43	341.64765531558078 - 348.51120217097923	40
44	348.51120217097923 - 355.37474902637769	55
45	355.37474902637769 - 362.23829588177614	47
46	362.23829588177614 - 369.10184273717459	35
47	369.10184273717459 - 375.96538959257305	55
48	375.96538959257305 - 382.8289364479715	38
49	382.8289364479715 - 389.69248330336995	38
50	389.69248330336995 - 396.55603015876841	44
51	396.55603015876841 - 403.41957701416686	37
52	403.41957701416686 - 410.28312386956532	29
53	410.28312386956532 - 417.14667072496377	40
54	417.14667072496377 - 424.01021758036222	44
55	424.01021758036222 - 430.87376443576068	37
56	430.87376443576068 - 437.73731129115913	38
57	437.73731129115913 - 444.60085814655758	31
58	444.60085814655758 - 451.46440500195604	23
59	451.46440500195604 - 458.32795185735449	20
60	458.32795185735449 - 465.19149871275295	25
61	465.19149871275295 - 472.0550455681514	27
62	472.0550455681514 - 478.91859242354985	26
63	478.91859242354985 - 485.78213927894831	24
64	485.78213927894831 - 492.64568613434676	25
65	492.64568613434676 - 499.50923298974521	33
66	499.50923298974521 - 506.37277984514367	25
67	506.37277984514367 - 513.23632670054212	29
68	513.23632670054212 - 520.09987355594058	20
69	520.09987355594058 - 526.96342041133903	22
70	526.96342041133903 - 533.82696726673748	23
71	533.82696726673748 - 540.69051412213594	20
72	540.69051412213594 - 547.55406097753439	20
73	547.55406097753439 - 554.41760783293284	18
74	554.41760783293284 - 561.2811546883313	26
75	561.2811546883313 - 568.14470154372975	24
76	568.14470154372975 - 575.00824839912821	16
77	575.00824839912821 - 581.87179525452666	21
78	581.87179525452666 - 588.73534210992511	9
79	588.73534210992511 - 595.59888896532357	25
80	595.59888896532357 - 602.46243582072202	17
81	602.46243582072202 - 609.32598267612047	21
82	609.32598267612047 - 616.18952953151893	23
83	616.18952953151893 - 623.05307638691738	27
84	623.05307638691738 - 629.91662324231584	17
85	629.91662324231584 - 636.78017009771429	23
86	636.78017009771429 - 643.64371695311274	25
87	643.64371695311274 - 650.5072638085112	27
88	650.5072638085112 - 657.37081066390965	21
89	657.37081066390965 - 664.23435751930811	12
90	664.23435751930811 - 671.09790437470656	22
91	671.09790437470656 - 677.96145123010501	24
92	677.96145123010501 - 684.82499808550347	20
93	684.82499808550347 - 691.68854494090192	22
94	691.68854494090192 - 698.55209179630037	23
95	698.55209179630037 - 705.41563865169883	28
96	705.41563865169883 - 712.27918550709728	20
97	712.27918550709728 - 719.14273236249574	25
98	719.14273236249574 - 726.00627921789419	14

99	726.00627921789419 - 732.86982607329264	17
100	732.86982607329264 - 739.7333729286911	18
101	739.7333729286911 - 746.59691978408955	25
102	746.59691978408955 - 753.460466639488	19
103	753.460466639488 - 760.32401349488646	20
104	760.32401349488646 - 767.18756035028491	20
105	767.18756035028491 - 774.05110720568337	21
106	774.05110720568337 - 780.91465406108182	18
107	780.91465406108182 - 787.77820091648027	21
108	787.77820091648027 - 794.64174777187873	20
109	794.64174777187873 - 801.50529462727718	24
110	801.50529462727718 - 808.36884148267563	38
111	808.36884148267563 - 815.23238833807409	19
112	815.23238833807409 - 822.09593519347254	24
113	822.09593519347254 - 828.959482048871	23
114	828.959482048871 - 835.82302890426945	16
115	835.82302890426945 - 842.6865757596679	23
116	842.6865757596679 - 849.55012261506636	19
117	849.55012261506636 - 856.41366947046481	15
118	856.41366947046481 - 863.27721632586326	26
119	863.27721632586326 - 870.14076318126172	30
120	870.14076318126172 - 877.00431003666017	19
121	877.00431003666017 - 883.86785689205863	13
122	883.86785689205863 - 890.73140374745708	29
123	890.73140374745708 - 897.59495060285553	21
124	897.59495060285553 - 904.45849745825399	19
125	904.45849745825399 - 911.32204431365244	16
126	911.32204431365244 - 918.18559116905089	28
127	918.18559116905089 - 925.04913802444935	17
128	925.04913802444935 - 931.9126848798478	14
129	931.9126848798478 - 938.77623173524626	17
130	938.77623173524626 - 945.63977859064471	14
131	945.63977859064471 - 952.50332544604316	18
132	952.50332544604316 - 959.36687230144162	9
133	959.36687230144162 - 966.23041915684007	21
134	966.23041915684007 - 973.09396601223852	20
135	973.09396601223852 - 979.95751286763698	17
136	979.95751286763698 - 986.82105972303543	19
137	986.82105972303543 - 993.68460657843389	18
138	993.68460657843389 - 1000.5481534338323	20
139	1000.5481534338323 - 1007.4117002892308	14
140	1007.4117002892308 - 1014.2752471446292	16
141	1014.2752471446292 - 1021.1387940000277	17
142	1021.1387940000277 - 1028.0023408554262	16
143	1028.0023408554262 - 1034.8658877108246	19
144	1034.8658877108246 - 1041.7294345662231	18
145	1041.7294345662231 - 1048.5929814216215	18
146	1048.5929814216215 - 1055.45652827702	18
147	1055.45652827702 - 1062.3200751324184	20
148	1062.3200751324184 - 1069.1836219878169	17
149	1069.1836219878169 - 1076.0471688432153	18
150	1076.0471688432153 - 1082.9107156986138	13
151	1082.9107156986138 - 1089.7742625540122	15
152	1089.7742625540122 - 1096.6378094094107	11
153	1096.6378094094107 - 1103.5013562648091	21
154	1103.5013562648091 - 1110.3649031202076	17
155	1110.3649031202076 - 1117.2284499756061	12

156	1117.2284499756061 - 1124.0919968310045	11
157	1124.0919968310045 - 1130.955543686403	11
158	1130.955543686403 - 1137.8190905418014	16
159	1137.8190905418014 - 1144.6826373971999	16
160	1144.6826373971999 - 1151.5461842525983	9
161	1151.5461842525983 - 1158.4097311079968	14
162	1158.4097311079968 - 1165.2732779633952	12
163	1165.2732779633952 - 1172.1368248187937	5
164	1172.1368248187937 - 1179.0003716741921	13
165	1179.0003716741921 - 1185.8639185295906	13
166	1185.8639185295906 - 1192.727465384989	12
167	1192.727465384989 - 1199.5910122403875	10
168	1199.5910122403875 - 1206.454559095786	11
169	1206.454559095786 - 1213.3181059511844	10
170	1213.3181059511844 - 1220.1816528065829	12
171	1220.1816528065829 - 1227.0451996619813	13
172	1227.0451996619813 - 1233.9087465173798	15
173	1233.9087465173798 - 1240.7722933727782	7
174	1240.7722933727782 - 1247.6358402281767	10
175	1247.6358402281767 - 1254.4993870835751	8
176	1254.4993870835751 - 1261.3629339389736	8
177	1261.3629339389736 - 1268.226480794372	13
178	1268.226480794372 - 1275.0900276497705	10
179	1275.0900276497705 - 1281.9535745051689	9
180	1281.9535745051689 - 1288.8171213605674	11
181	1288.8171213605674 - 1295.6806682159659	10
182	1295.6806682159659 - 1302.5442150713643	3
183	1302.5442150713643 - 1309.4077619267628	11
184	1309.4077619267628 - 1316.2713087821612	11
185	1316.2713087821612 - 1323.1348556375597	7
186	1323.1348556375597 - 1329.9984024929581	8
187	1329.9984024929581 - 1336.8619493483566	14
188	1336.8619493483566 - 1343.725496203755	4
189	1343.725496203755 - 1350.5890430591535	6
190	1350.5890430591535 - 1357.4525899145519	12
191	1357.4525899145519 - 1364.3161367699504	8
192	1364.3161367699504 - 1371.1796836253488	7
193	1371.1796836253488 - 1378.0432304807473	11
194	1378.0432304807473 - 1384.9067773361458	5
195	1384.9067773361458 - 1391.7703241915442	8
196	1391.7703241915442 - 1398.6338710469427	8
197	1398.6338710469427 - 1405.4974179023411	8
198	1405.4974179023411 - 1412.3609647577396	8
199	1412.3609647577396 - 1419.224511613138	9
200	1419.224511613138 - 1426.0880584685365	9
201	1426.0880584685365 - 1432.9516053239349	13
202	1432.9516053239349 - 1439.8151521793334	13
203	1439.8151521793334 - 1446.6786990347318	3
204	1446.6786990347318 - 1453.5422458901303	8
205	1453.5422458901303 - 1460.4057927455287	17
206	1460.4057927455287 - 1467.2693396009272	6
207	1467.2693396009272 - 1474.1328864563257	8
208	1474.1328864563257 - 1480.9964333117241	1
209	1480.9964333117241 - 1487.8599801671226	7
210	1487.8599801671226 - 1494.723527022521	9
211	1494.723527022521 - 1501.5870738779195	7
212	1501.5870738779195 - 1508.4506207333179	10

213	1508.4506207333179 - 1515.3141675887164	5
214	1515.3141675887164 - 1522.1777144441148	4
215	1522.1777144441148 - 1529.0412612995133	5
216	1529.0412612995133 - 1535.9048081549117	5
217	1535.9048081549117 - 1542.7683550103102	7
218	1542.7683550103102 - 1549.6319018657086	5
219	1549.6319018657086 - 1556.4954487211071	3
220	1556.4954487211071 - 1563.3589955765055	6
221	1563.3589955765055 - 1570.222542431904	4
222	1570.222542431904 - 1577.0860892873025	5
223	1577.0860892873025 - 1583.9496361427009	6
224	1583.9496361427009 - 1590.8131829980994	3
225	1590.8131829980994 - 1597.6767298534978	5
226	1597.6767298534978 - 1604.5402767088963	1
227	1604.5402767088963 - 1611.4038235642947	7
228	1611.4038235642947 - 1618.2673704196932	7
229	1618.2673704196932 - 1625.1309172750916	5
230	1625.1309172750916 - 1631.9944641304901	6
231	1631.9944641304901 - 1638.8580109858885	8
232	1638.8580109858885 - 1645.721557841287	6
233	1645.721557841287 - 1652.5851046966854	4
234	1652.5851046966854 - 1659.4486515520839	6
235	1659.4486515520839 - 1666.3121984074824	1
236	1666.3121984074824 - 1673.1757452628808	3
237	1673.1757452628808 - 1680.0392921182793	8
238	1680.0392921182793 - 1686.9028389736777	0
239	1686.9028389736777 - 1693.7663858290762	5
240	1693.7663858290762 - 1700.6299326844746	2
241	1700.6299326844746 - 1707.4934795398731	5
242	1707.4934795398731 - 1714.3570263952715	4
243	1714.3570263952715 - 1721.22057325067	6
244	1721.22057325067 - 1728.0841201060684	5
245	1728.0841201060684 - 1734.9476669614669	3
246	1734.9476669614669 - 1741.8112138168653	5
247	1741.8112138168653 - 1748.6747606722638	5
248	1748.6747606722638 - 1755.5383075276623	5
249	1755.5383075276623 - 1762.4018543830607	2
250	1762.4018543830607 - 1769.2654012384592	3
251	1769.2654012384592 - 1776.1289480938576	2
252	1776.1289480938576 - 1782.9924949492561	2
253	1782.9924949492561 - 1789.8560418046545	2
254	1789.8560418046545 - 1796.719588660053	5
255	1796.719588660053 - 1803.5831355154514	2

Table 16c. Maximum Difference Snow and Ice Index used to construct categorical histogram for 2016.

Index	Text	Vertical Bar
0	-25.271576881408688 - -25.260333860293027	11
1	-25.260333860293027 - -25.249090839177367	15
2	-25.249090839177367 - -25.237847818061706	18
3	-25.237847818061706 - -25.226604796946045	13
4	-25.226604796946045 - -25.215361775830385	21
5	-25.215361775830385 - -25.204118754714724	34
6	-25.204118754714724 - -25.192875733599063	32
7	-25.192875733599063 - -25.181632712483403	25

```
8     -25.181632712483403 - -25.170389691367742 17
9     -25.170389691367742 - -25.159146670252081 35
10    -25.159146670252081 - -25.147903649136421 25
11    -25.147903649136421 - -25.13666062802076  26
12    -25.13666062802076 - -25.125417606905099  22
13    -25.125417606905099 - -25.114174585789439 32
14    -25.114174585789439 - -25.102931564673778 32
15    -25.102931564673778 - -25.091688543558117 31
16    -25.091688543558117 - -25.080445522442457 35
17    -25.080445522442457 - -25.069202501326796 45
18    -25.069202501326796 - -25.057959480211135 46
19    -25.057959480211135 - -25.046716459095475 46
20    -25.046716459095475 - -25.035473437979814 28
21    -25.035473437979814 - -25.024230416864153 42
22    -25.024230416864153 - -25.012987395748493 50
23    -25.012987395748493 - -25.001744374632832 65
24    -25.001744374632832 - -24.990501353517171 30
25    -24.990501353517171 - -24.979258332401511 61
26    -24.979258332401511 - -24.96801531128585  49
27    -24.96801531128585 - -24.956772290170189  83
28    -24.956772290170189 - -24.945529269054528 38
29    -24.945529269054528 - -24.934286247938868 95
30    -24.934286247938868 - -24.923043226823207 88
31    -24.923043226823207 - -24.911800205707546 100
32    -24.911800205707546 - -24.900557184591886 54
33    -24.900557184591886 - -24.889314163476225 101
34    -24.889314163476225 - -24.878071142360564 94
35    -24.878071142360564 - -24.866828121244904 87
36    -24.866828121244904 - -24.855585100129243 108
37    -24.855585100129243 - -24.844342079013582 61
38    -24.844342079013582 - -24.833099057897922 123
39    -24.833099057897922 - -24.821856036782261 124
40    -24.821856036782261 - -24.8106130156666   111
41    -24.8106130156666 - -24.79936999455094    100
42    -24.79936999455094 - -24.788126973435279  124
43    -24.788126973435279 - -24.776883952319618 135
44    -24.776883952319618 - -24.765640931203958 108
45    -24.765640931203958 - -24.754397910088297 83
46    -24.754397910088297 - -24.743154888972636 155
47    -24.743154888972636 - -24.731911867856976 157
48    -24.731911867856976 - -24.720668846741315 157
49    -24.720668846741315 - -24.709425825625654 107
50    -24.709425825625654 - -24.698182804509994 154
51    -24.698182804509994 - -24.686939783394333 144
52    -24.686939783394333 - -24.675696762278672 171
53    -24.675696762278672 - -24.664453741163012 111
54    -24.664453741163012 - -24.653210720047351 130
55    -24.653210720047351 - -24.64196769893169  160
56    -24.64196769893169 - -24.63072467781603   168
57    -24.63072467781603 - -24.619481656700369  194
58    -24.619481656700369 - -24.608238635584708 113
59    -24.608238635584708 - -24.596995614469048 183
60    -24.596995614469048 - -24.585752593353387 169
61    -24.585752593353387 - -24.574509572237726 192
62    -24.574509572237726 - -24.563266551122066 138
63    -24.563266551122066 - -24.552023530006405 205
64    -24.552023530006405 - -24.540780508890744 193
```

65 -24.540780508890744 - -24.529537487775084 197
66 -24.529537487775084 - -24.518294466659423 126
67 -24.518294466659423 - -24.507051445543762 215
68 -24.507051445543762 - -24.495808424428102 230
69 -24.495808424428102 - -24.484565403312441 194
70 -24.484565403312441 - -24.47332238219678 234
71 -24.47332238219678 - -24.46207936108112 162
72 -24.46207936108112 - -24.450836339965459 217
73 -24.450836339965459 - -24.439593318849798 244
74 -24.439593318849798 - -24.428350297734138 227
75 -24.428350297734138 - -24.417107276618477 203
76 -24.417107276618477 - -24.405864255502816 275
77 -24.405864255502816 - -24.394621234387156 284
78 -24.394621234387156 - -24.383378213271495 291
79 -24.383378213271495 - -24.372135192155834 306
80 -24.372135192155834 - -24.360892171040174 244
81 -24.360892171040174 - -24.349649149924513 320
82 -24.349649149924513 - -24.338406128808852 352
83 -24.338406128808852 - -24.327163107693192 349
84 -24.327163107693192 - -24.315920086577531 258
85 -24.315920086577531 - -24.30467706546187 357
86 -24.30467706546187 - -24.29343404434621 377
87 -24.29343404434621 - -24.282191023230549 448
88 -24.282191023230549 - -24.270948002114888 422
89 -24.270948002114888 - -24.259704980999228 316
90 -24.259704980999228 - -24.248461959883567 463
91 -24.248461959883567 - -24.237218938767906 487
92 -24.237218938767906 - -24.225975917652246 514
93 -24.225975917652246 - -24.214732896536585 363
94 -24.214732896536585 - -24.203489875420924 509
95 -24.203489875420924 - -24.192246854305264 570
96 -24.192246854305264 - -24.181003833189603 568
97 -24.181003833189603 - -24.169760812073942 626
98 -24.169760812073942 - -24.158517790958282 439
99 -24.158517790958282 - -24.147274769842621 632
100 -24.147274769842621 - -24.13603174872696 622
101 -24.13603174872696 - -24.1247887276113 684
102 -24.1247887276113 - -24.113545706495639 485
103 -24.113545706495639 - -24.102302685379978 649
104 -24.102302685379978 - -24.091059664264318 625
105 -24.091059664264318 - -24.079816643148657 615
106 -24.079816643148657 - -24.068573622032996 705
107 -24.068573622032996 - -24.057330600917336 417
108 -24.057330600917336 - -24.046087579801675 656
109 -24.046087579801675 - -24.034844558686014 692
110 -24.034844558686014 - -24.023601537570354 715
111 -24.023601537570354 - -24.012358516454693 795
112 -24.012358516454693 - -24.001115495339032 509
113 -24.001115495339032 - -23.989872474223372 741
114 -23.989872474223372 - -23.978629453107711 782
115 -23.978629453107711 - -23.96738643199205 777
116 -23.96738643199205 - -23.95614341087639 780
117 -23.95614341087639 - -23.944900389760729 526
118 -23.944900389760729 - -23.933657368645068 785
119 -23.933657368645068 - -23.922414347529408 790
120 -23.922414347529408 - -23.911171326413747 843
121 -23.911171326413747 - -23.899928305298086 565

122 -23.899928305298086 - -23.888685284182426 784
123 -23.888685284182426 - -23.877442263066765 774
124 -23.877442263066765 - -23.866199241951104 730
125 -23.866199241951104 - -23.854956220835444 785
126 -23.854956220835444 - -23.843713199719783 507
127 -23.843713199719783 - -23.832470178604122 758
128 -23.832470178604122 - -23.821227157488462 775
129 -23.821227157488462 - -23.809984136372801 799
130 -23.809984136372801 - -23.79874111525714 802
131 -23.79874111525714 - -23.78749809414148 537
132 -23.78749809414148 - -23.776255073025819 749
133 -23.776255073025819 - -23.765012051910158 756
134 -23.765012051910158 - -23.753769030794498 823
135 -23.753769030794498 - -23.742526009678837 748
136 -23.742526009678837 - -23.731282988563176 457
137 -23.731282988563176 - -23.720039967447516 733
138 -23.720039967447516 - -23.708796946331855 756
139 -23.708796946331855 - -23.697553925216194 736
140 -23.697553925216194 - -23.686310904100534 782
141 -23.686310904100534 - -23.675067882984873 563
142 -23.675067882984873 - -23.663824861869212 804
143 -23.663824861869212 - -23.652581840753552 766
144 -23.652581840753552 - -23.641338819637891 760
145 -23.641338819637891 - -23.63009579852223 757
146 -23.63009579852223 - -23.61885277740657 547
147 -23.61885277740657 - -23.607609756290909 765
148 -23.607609756290909 - -23.596366735175248 769
149 -23.596366735175248 - -23.585123714059588 769
150 -23.585123714059588 - -23.573880692943927 776
151 -23.573880692943927 - -23.562637671828266 802
152 -23.562637671828266 - -23.551394650712606 549
153 -23.551394650712606 - -23.540151629596945 737
154 -23.540151629596945 - -23.528908608481284 783
155 -23.528908608481284 - -23.517665587365624 753
156 -23.517665587365624 - -23.506422566249963 826
157 -23.506422566249963 - -23.495179545134302 521
158 -23.495179545134302 - -23.483936524018642 764
159 -23.483936524018642 - -23.472693502902981 806
160 -23.472693502902981 - -23.46145048178732 768
161 -23.46145048178732 - -23.45020746067166 806
162 -23.45020746067166 - -23.438964439555999 504
163 -23.438964439555999 - -23.427721418440338 770
164 -23.427721418440338 - -23.416478397324678 807
165 -23.416478397324678 - -23.405235376209017 776
166 -23.405235376209017 - -23.393992355093356 726
167 -23.393992355093356 - -23.382749333977696 528
168 -23.382749333977696 - -23.371506312862035 773
169 -23.371506312862035 - -23.360263291746374 772
170 -23.360263291746374 - -23.349020270630714 719
171 -23.349020270630714 - -23.337777249515053 757
172 -23.337777249515053 - -23.326534228399392 759
173 -23.326534228399392 - -23.315291207283732 499
174 -23.315291207283732 - -23.304048186168071 723
175 -23.304048186168071 - -23.29280516505241 728
176 -23.29280516505241 - -23.28156214393675 691
177 -23.28156214393675 - -23.270319122821089 692
178 -23.270319122821089 - -23.259076101705428 463

179 -23.259076101705428 - -23.247833080589768 722
180 -23.247833080589768 - -23.236590059474107 693
181 -23.236590059474107 - -23.225347038358446 675
182 -23.225347038358446 - -23.214104017242786 605
183 -23.214104017242786 - -23.202860996127125 652
184 -23.202860996127125 - -23.191617975011464 441
185 -23.191617975011464 - -23.180374953895804 622
186 -23.180374953895804 - -23.169131932780143 627
187 -23.169131932780143 - -23.157888911664482 630
188 -23.157888911664482 - -23.146645890548822 657
189 -23.146645890548822 - -23.135402869433161 415
190 -23.135402869433161 - -23.1241598483175 565
191 -23.1241598483175 - -23.11291682720184 651
192 -23.11291682720184 - -23.101673806086179 610
193 -23.101673806086179 - -23.090430784970518 535
194 -23.090430784970518 - -23.079187763854858 545
195 -23.079187763854858 - -23.067944742739197 301
196 -23.067944742739197 - -23.056701721623536 477
197 -23.056701721623536 - -23.045458700507876 514
198 -23.045458700507876 - -23.034215679392215 433
199 -23.034215679392215 - -23.022972658276554 469
200 -23.022972658276554 - -23.011729637160894 463
201 -23.011729637160894 - -23.000486616045233 299
202 -23.000486616045233 - -22.989243594929572 428
203 -22.989243594929572 - -22.978000573813912 387
204 -22.978000573813912 - -22.966757552698251 376
205 -22.966757552698251 - -22.95551453158259 391
206 -22.95551453158259 - -22.94427151046693 322
207 -22.94427151046693 - -22.933028489351269 231
208 -22.933028489351269 - -22.921785468235608 338
209 -22.921785468235608 - -22.910542447119948 319
210 -22.910542447119948 - -22.899299426004287 335
211 -22.899299426004287 - -22.888056404888626 293
212 -22.888056404888626 - -22.876813383772966 291
213 -22.876813383772966 - -22.865570362657305 191
214 -22.865570362657305 - -22.854327341541644 257
215 -22.854327341541644 - -22.843084320425984 250
216 -22.843084320425984 - -22.831841299310323 254
217 -22.831841299310323 - -22.820598278194662 233
218 -22.820598278194662 - -22.809355257079002 253
219 -22.809355257079002 - -22.798112235963341 139
220 -22.798112235963341 - -22.78686921484768 197
221 -22.78686921484768 - -22.77562619373202 191
222 -22.77562619373202 - -22.764383172616359 178
223 -22.764383172616359 - -22.753140151500698 182
224 -22.753140151500698 - -22.741897130385038 160
225 -22.741897130385038 - -22.730654109269377 99
226 -22.730654109269377 - -22.719411088153716 129
227 -22.719411088153716 - -22.708168067038056 164
228 -22.708168067038056 - -22.696925045922395 143
229 -22.696925045922395 - -22.685682024806734 130
230 -22.685682024806734 - -22.674439003691074 133
231 -22.674439003691074 - -22.663195982575413 95
232 -22.663195982575413 - -22.651952961459752 122
233 -22.651952961459752 - -22.640709940344092 103
234 -22.640709940344092 - -22.629466919228431 106
235 -22.629466919228431 - -22.61822389811277 85

236	-22.61822389811277 - -22.60698087699711	81
237	-22.60698087699711 - -22.595737855881449	55
238	-22.595737855881449 - -22.584494834765788	74
239	-22.584494834765788 - -22.573251813650128	82
240	-22.573251813650128 - -22.562008792534467	78
241	-22.562008792534467 - -22.550765771418806	77
242	-22.550765771418806 - -22.539522750303146	65
243	-22.539522750303146 - -22.528279729187485	56
244	-22.528279729187485 - -22.517036708071824	40
245	-22.517036708071824 - -22.505793686956164	62
246	-22.505793686956164 - -22.494550665840503	53
247	-22.494550665840503 - -22.483307644724842	41
248	-22.483307644724842 - -22.472064623609182	53
249	-22.472064623609182 - -22.460821602493521	50
250	-22.460821602493521 - -22.44957858137786	29
251	-22.44957858137786 - -22.4383355602622	28
252	-22.4383355602622 - -22.427092539146539	44
253	-22.427092539146539 - -22.415849518030878	38
254	-22.415849518030878 - -22.404606496915218	33
255	-22.404606496915218 - -22.393363475799557	35

Table 17c. Temperature subset distribution used to construct categorical histogram and perform KS Normality Test for 2016.

Appendix C.8 Thermistor Data taken from Appendix D of '2016 Surface Water Quality Assessment' prepared by Husky Energy

Sensor depth (m b.g.s)	0.85	1.6	2.35	3.1	3.85	4.6
Min MW-04T (°C)	-2.43	-1.65	-1.45	-1.26	-1.14	-1.1
Max MW-04T (°C)	-1.08	-1.08	-1.2	-1.08	-0.83	-0.69
Sensor depth (m b.g.s)	0.85	1.6	2.35	3.1	3.85	4.6
Min MW-09T (°C)	-14.39	-9.8	-6.6	-4.76	-3.09	-2.1
Max MW-09T (°C)	9.42	1.76	-0.44	-0.86	-0.96	-0.97
Sensor depth (m b.g.s)	3.7	5.7	7.7	9.7	11.7	13.7
Min MW-12T (°C)	-2.63	-1.08	-0.71	-0.56	-0.48	-0.42
Max MW-12T (°C)	-0.38	-0.16	-0.18	-0.17	-0.17	-0.13

Table 18c. Thermistor data collected by Husky Energy between March 2013 and August 2016.